

1 **Response to Reviewer1**

2

3 **“In my opinion the manuscript Direct radiative effects of intense Mediterranean desert dust**
4 **outbreaks is acceptable for publication in ACP in its current state.”**

5

6 Thanks!

7

8 Before our paper being published in ACPD, the reviewer made the following comment and the Editor
9 suggested that it should be answered in the current review process. Please find our response (regular font)
10 below the reviewer’s comment (bold font).

11

12 **“My major concern is how the model takes into account the relative humidity to scale the optical**
13 **(e.g. real and imaginary refractive indices) and the microphysical properties (e.g. size) of the**
14 **aerosols. As authors well-know and say within the manuscript the water vapor influences SW and**
15 **LW spectral ranges. It is not clear for me how the RRTMG considers this significant aspect (RH).**
16 **An analysis the relative humidity (RH) in this area for these 20 desert dust cases would be very**
17 **clarifying because it is huge important to go through how the RH changes from day to night times**
18 **and how the desert dust optical and microphysical properties vary from day to night times.**
19 **Relevant parameters in your calculations are the mass extinction efficiency, the single scattering**
20 **albedo and the asymmetry parameter. The effect of the RH over them is well explained by Myhre**
21 **et al. (1998).”**

22

23 In the NMMB-MONARCH model, dust aerosols are externally mixed and hydrophobic. Therefore, no
24 hygroscopic growth is considered and subsequently the RH effects are not taken into account in the
25 RRTMG. This assumption, it is not expected to introduce large errors since it is well documented in
26 literature that mineral particles are mainly hydrophobic and consisted of insoluble substances,
27 particularly over desert regions. Of course, it is also known (e.g. Sullivan et al., 2009; Knippertz and
28 Stuut, 2014) that dust hygroscopicity increases through mixing soluble of hygroscopic material with
29 insoluble mineral particles, thus leading to the formation of internal mixtures of dust and sulfate, which
30 can make mineral particles more soluble. Nevertheless, it should be noted that for such atmospheric
31 processing to take place, time is needed and that this increase of dust hygroscopicity mainly occurs
32 through aging. However, our study focuses on intense dust episodes above the Mediterranean, which
33 basically transport fresh, and thus hydrophobic, dust particles. This clarification has been added in the
34 revised manuscript (Lines 283-284). The paper of Myhre et al. (1998), regarding the effect of RH on
35 optical properties, refers to sulfate and soot aerosols, and not dust.

36

37

38

39

40

41

42

43

44

45

46 **Response to Reviewer2**

47
48 We would like to thank the Reviewer for the useful comments that helped us to improve our manuscript.
49 Below are given point by point answers to the comments (also provided in bold font).

50
51 **“The paper addresses an important aspect of the Mediterranean radiation budget and climate.**
52 **Intense Saharan dusts event may produce large perturbations to radiation, and affect surface**
53 **temperature, heat exchange at the surface, circulation, etc. The study uses satellite data to identify**
54 **intense events. Effects on radiation and different processes are investigated for the selected cases**
55 **using a regional model which includes dust and radiation.**

56
57 **The paper is an interesting and useful contribution to the understanding of dust role and**
58 **interactions in the Mediterranean.**

59
60 **A couple of aspects may be improved.”**

61
62 **“The radiative effects are strongly related with the aerosol optical depth (AOD). A comparison of**
63 **AOD values produced by the model versus those obtained from MODIS is presented in the paper.**
64 **However, the comparison is qualitative and for a selection of cases. Given the large role of AOD in**
65 **determining the radiative effects, a more detailed, possibly quantitative, comparison should be**
66 **carried out. On the same point, some reference is made throughout the text to the inability of the**
67 **model in reproducing the amount of dust. This should be better assessed.”**

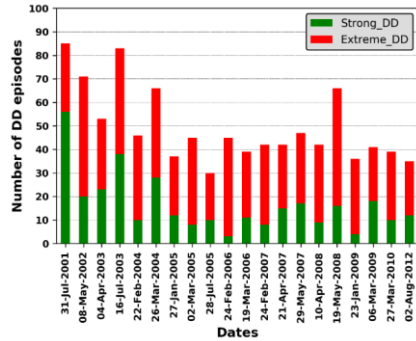
68
69 As suggested by the Reviewer, we have made a more detailed comparison between the observed
70 (MODIS) and simulated (NMMB) AODs. In order to eliminate the spatial inconsistencies between the
71 two products, we have regridded the model outputs from their raw spatial resolution ($0.25^\circ \times 0.25^\circ$) to
72 $1^\circ \times 1^\circ$ in order to match them the resolution of satellite retrievals. The new geographical distributions
73 of the modelled AODs (dynamically calculated dust plus GOCART climatology for the other aerosol
74 types), at coarse spatial resolution, have replaced the old ones presented in Figures 3 and S1 of the
75 previous version of manuscript. In both MODIS and NMMB patterns a common colorbar is used making
76 easier a visual intercomparison for the reader. Moreover, the model AODs have been compared against
77 those of MODIS, considering only the grid cells where a DD episode (either strong or extreme) has been
78 identified by the satellite algorithm. Note that NMMB-MODIS comparison all over the MSD is not
79 possible because of the gaps (white areas) in MODIS AOD distributions, given that the operation of
80 MODIS retrieval algorithm is impossible therein. The obtained results for each episode, in terms of
81 overall computed correlation coefficient and bias (defined as NMMB-MODIS) are given in Fig. R1,
82 while the stacked bars illustrate the number of strong, extreme and total DD episodes for each case
83 (available also in Table 1).

84 Among the studied cases, it is revealed a strong variation of R values (Figure R1-ii) which reflects the
85 diversity of the model’s capability in terms of capturing the spatial patterns of the desert dust outbreaks.
86 These drawbacks rise mainly from displacements of the simulated dust patterns with respect to the
87 observed ones (see Figs 3 and S1). The best performance is found on 22 Feb 2004 ($R=0.82$) while in 7
88 out of 20 cases R values are higher than 0.5. As it concerns the bias, in absolute terms, in all the events
89 negative values are recorded ranging from -2.3 (24 Feb 2006) to -0.17 (19 May 2008). This finding shows
90 that the model underestimates consistently the intensity of the desert dust outbreaks which have been
91 analyzed in the present study.

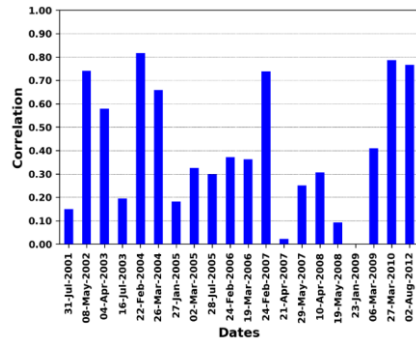
92 According to the evaluation analysis, the model’s ability in terms of reproducing satisfactorily the
93 dust fields varies strongly case-by-case while the simulated intensity of the desert dust outbreaks is lower

94 with respect to the satellite retrievals. It should be noted that the level of agreement between observed
 95 and simulated AODs (Lines 451-465) is not only associated with the model deficiencies, but also with
 96 other factors like the temporal inconsistency between the two products. More specifically, the satellite
 97 retrievals correspond to daily averages whereas the model products are representative for a specific
 98 forecast time (instantaneous fields). Considering the high variability of aerosols' loads, particularly under
 99 episodic conditions, this temporal discrepancy imposes a limitation when a quantitative comparison
 100 between MODIS and NMMB is attempted. This fact can explain the observed differences found either
 101 on the intensity or on the spatial patterns of the desert dust events. Also, it must be considered that
 102 artifacts of the satellite retrievals (e.g. clouds contamination, representativeness/homogeneity within the
 103 1° x 1° grid cell) may lead to higher AODs as it has been shown in relevant evaluation studies (Gkikas
 104 et al., 2016). In the revised manuscript, the discussion in Section 5.1 has been updated presenting the
 105 quantitative comparison of NMMB-MONARCH versus MODIS-Terra as well as the reasons which lead
 106 to deviations between these two products.

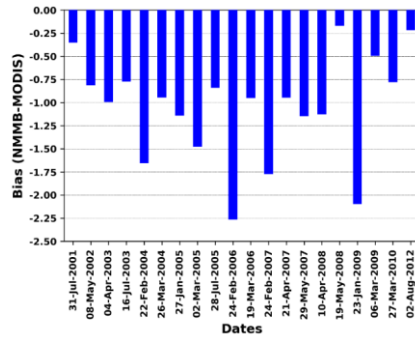
107 Finally, we would like to bring to the attention of the Reviewer that a detailed evaluation of the same
 108 version of the NMMB model for 2006 has been presented in Pérez et al. (2011), who compared the model
 109 products against MISR and AERONET retrievals. Based on their findings, for a domain including the
 110 Mediterranean, it is revealed that the model in general is able to reproduce satisfactorily the
 111 spatiotemporal features of the desert dust fields. Moreover, an evaluation of the NMMB AOD forecasts,
 112 along with similar forecasts from other models, against ground based AERONET and satellite MODIS
 113 retrievals, is available at the weblink of SDS-WAS System ([https://sds-was.aemet.es/forecast-
 114 products/forecast-evaluation](https://sds-was.aemet.es/forecast-products/forecast-evaluation)) to which reference is now made in the revised manuscript (lines 303-306).
 115



(i)



(ii)



(iii)

116 **Figure R1:** (i) Number of strong (green bars), extreme (red bars) and total (entire bars) DD episodes identified by the satellite
 117 algorithm, (ii) Correlation coefficients (R) between satellite and model AODs, (iii) Regional average biases between the
 118 NMMB simulated and the MODIS retrieved AODs. Results are given for each studied case (given in x-axis) and are computed
 119 taking into account only pixels over which a DD episode (either strong or extreme) has been identified by the satellite
 120 algorithm.

121 **“Some results, mainly in the shortwave spectral range, may be linked to differences in the surface**
 122 **albedo, in particular between ocean and land/desert. The discussion of this point may be somewhat**
 123 **improved. In some cases, averages over the Mediterranean Satellite Domain (MSD) have been**
 124 **used. The domain includes land and ocean surfaces. I would suggest separating the estimates of**
 125 **radiative effects obtained on land from those obtained over the ocean. Summing/compensation**
 126 **effects, also dependent on the fraction of surface type occurring in each event, may be present when**
 127 **the average includes land and ocean surface types.”**

128
 129 The regional SW DREs for the MSD have been calculated separately over land and sea and the obtained
 130 results are illustrated in Figure R2. The temporal variation of SW DRE_{ATM}, DRE_{SURF} and DRE_{NETSURF}
 131 values is similar with the one presented for the whole Mediterranean domain (Figure 5 in the revised
 132 document) over both land and ocean areas. However, a careful eye look reveals differences between land
 133 and ocean DREs. Thus, over dark (sea) surfaces DRE_{SURF} and DRE_{NETSURF} values are almost equal (Fig.
 134 R2-ii) while over brighter (land) surfaces DRE_{NETSURF} values clearly differ by DRE_{SURF} ones, i.e. they
 135 are smaller, due to the higher surface albedo, leading to increasing upward component and reducing the
 136 absorbed radiation. Another difference between land and ocean DREs is the larger magnitude of surface
 137 DREs over ocean than land areas, especially in early forecast times, due to higher AODs over ocean. The
 138 most noticeable difference between the Mediterranean land and sea DREs is evident at TOA, both in
 139 terms of temporal variation and magnitude, clearly reflecting the role of the surface albedo. In particular,
 140 over land, the DRE_{TOA} values are maximum (up to 9 Wm⁻²) during early morning and afternoon hours,
 141 decreasing in magnitude between 9-12 UTC (values ranging from -3.6 to -2.2 Wm⁻²) while such a
 142 decrease is not observed over sea areas. Also, the magnitude of ocean DRE_{TOA} values is smaller than
 143 over land, i.e. a stronger cooling of the Earth-atmosphere system is produced by aerosols over oceans
 144 than land due to the low sea water albedo below aerosols. The overall computed SW DREs presented in
 145 Figure 5 (without discriminating between land and sea grid points of the NMMB-MONARCH model)
 146 are mainly driven by the corresponding DREs over continental Mediterranean areas. The aforementioned
 147 result is also valid for the whole simulation domain (NSD) as well as for the Sahara domain (SDD). In
 148 the revised document a short sentence has been added (Lines 582-584).

149
 150

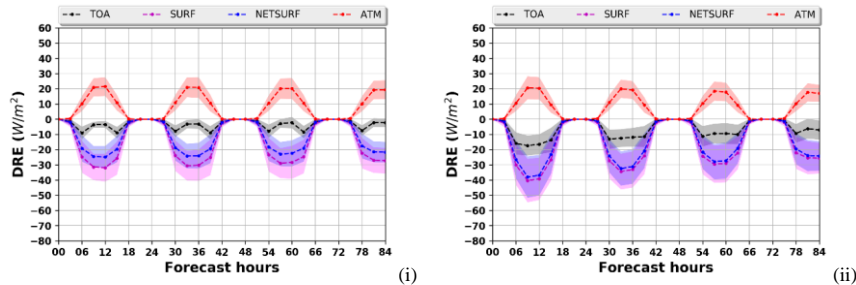


Figure R2: Regional all-sky SW DREs calculated over the MSD above: (i) land and (ii) sea areas.

151
152

153
154 Minor points are outlined below.

155
156 **“lines 17-19: please, indicate the AOD range attained during the selected events.”**

157
158 We have added in the text (lines 22-23) the range of the maximum dust AODs (2.5 – 5.5) simulated by
159 the NMMB-MONARCH model.

160
161 **“l.21-26: please, specify for what AOD and over what area these vary large radiative effects are
162 found.”**

163
164 Done. Please see Lines 23-31.

165
166 **“l. 66-68: the sentence is not clear; please, rephrase it”**

167
168 The following sentence in the submitted document has been replaced with a new one (written below) in
169 the revised text (Lines 73-76).

170
171 **OLD (submitted manuscript)**

172 “Through this chain of complex processes, it is described the indirect impact of mineral particles on the
173 radiation and compared to the other two dust radiative effects (direct and semi-direct) is characterized by
174 even larger uncertainties.”

175
176 **NEW (revised manuscript)**

177 “This chain of complex processes, involving aerosol-cloud-interactions (ACI) and the subsequent
178 modifications of the radiation fields, constitute the indirect impact of mineral particles on radiation,
179 which is characterized by the largest uncertainties, even larger than those of the dust direct and semi-
180 direct effects.”

181
182 **“l. 153: I would suggest specifying here that the dust outbreaks are identified using daily multi-
183 sensor satellite data”**

184
185 Done. Please see Lines 160-163 in the revised manuscript.

186
187 **“l. 188-: please, clarify the difference between pixel and grid cell: are those the same?”**

188

189 Both terms have the same meaning. In order to be clear we have added this clarification in Lines 200-
190 202.

191
192 **“table 1: are all the selected cases classified as "extreme" events? Are there "strong" events among
193 them? Is there information on the time duration of the events?”**

194
195 For each dust outbreak there are pixel-level episodes that are either strong or extreme, according to their
196 AOD values. As suggested by the Referee, we have added in Table 1 two columns giving the number of
197 strong and extreme DD episodes for each dust outbreak. Moreover, in the revised manuscript we have
198 included this information by providing the ranges for the strong and extreme DD episodes that took place
199 within the MSD (see Lines 224-228). No information is given about the duration of studied events
200 because according to our analysis, the maximum duration (consecutive days satisfying the defined
201 criteria, see sect. 2) is two (2) days, but in such cases we have decided to keep just the day for which the
202 number of total pixel-level DD episodes is higher (see Lines 216-217).

203
204

Case	Date	Strong DD episodes	Extreme DD episodes	Total DD episodes	Intensity	Affected parts of the Mediterranean domain
1	31 July 2001	56	29	85	0.74	Western
2	8 May 2002	20	51	71	1.60	Central
3	4 April 2003	23	30	53	1.42	Eastern
4	16 July 2003	38	45	83	0.98	Western and Central
5	22 February 2004	10	36	46	2.18	Central and Eastern
6	26 March 2004	28	38	66	1.45	Central and Eastern
7	27 January 2005	12	25	37	1.36	Central and Eastern
8	2 March 2005	8	37	45	2.96	Central and Eastern
9	28 July 2005	10	20	30	1.08	Western and Central
10	24 February 2006	3	42	45	2.92	Eastern
11	19 March 2006	11	28	39	1.37	Eastern
12	24 February 2007	8	34	42	2.29	Central and Eastern
13	21 April 2007	15	27	42	1.65	Central
14	29 May 2007	17	30	47	1.40	Eastern
15	10 April 2008	9	33	42	1.58	Central
16	19 May 2008	16	50	66	1.45	Central
17	23 January 2009	4	32	36	2.65	Eastern
18	6 March 2009	18	23	41	1.41	Eastern
19	27 March 2010	10	29	39	1.43	Central
20	2 August 2012	12	23	35	1.20	Western

205
206 **“l. 308: "quadratic" should be "quadrature"”**

207
208 We have corrected it.

209
210 **“l. 313: the correct web address seems to be: <http://rtweb.aer.com/>”**

211
212 We have corrected this. Thanks for the note.

213
214 **“l. 317: maybe "fraction" instead of "percentage"”**

215
216 We have changed the text according to the reviewer’s suggestion.

217

218 **“I. 324: it may be useful to add here information on the used refractive indices. They play a central**
219 **role in the determination of the radiative effects, and the reader should be aware of which set of**
220 **refractive index values are used in the calculations.”**

221
222 In Lines 331-336 of the revised manuscript, we have provided information on the refractive indices used
223 in the model, as requested by the reviewer. More specifically, it is now specified that the refractive indices
224 used in our simulations were taken by GADS (Koepke et al., 1997) and modified following Sinyuk et al.
225 (2003), as described in Pérez et al. (2011).

226
227 **“section 5.1: as discussed above, the comparison between satellite and modelled AOD seems**
228 **qualitative. Given the stated limitations of the satellite dataset over land, a quantitative comparison**
229 **might be carried out over the ocean. Also, the use of different colour scales in figure 3 does not**
230 **allow a more detailed comparison.”**

231
232 Please see our response to your first main comment.

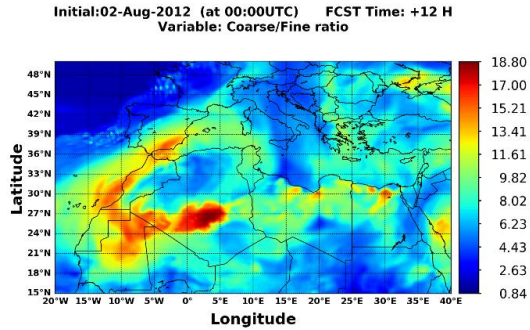
233
234 **“I. 552: may the differences between the results over the MSD and SDD domains be partly due to**
235 **the albedo differences? I would expect an effect, mainly for the NETSURF component.”**

236
237 In the shortwave spectrum, the surface albedo plays a critical role on the observed differences between
238 the calculated DREs in the MSD and SDD. This is evident at noon when positive (planetary warming)
239 and negative (planetary cooling) DRE_{TOA} values are found over the Sahara and the Mediterranean,
240 respectively (Figure 5). In the former region, due to the higher surface albedo the atmospheric warming
241 enhances (mineral particles do not absorb only the incoming SW radiation but also the reflected radiation
242 from the ground) dominating over the surface (NETSURF) cooling which decreases since the upward
243 component (reflected radiation from the ground) increases. On the contrary, over dark areas (maritime
244 environments or vegetated land) the dust layers are brighter than the underlying surface resulting in
245 negative perturbations (cooling effect) at TOA. Summarizing, the contrast between low- and high-
246 reflective surfaces doesn't affect only the absorbed radiation at the ground (NETSURF) but also the
247 atmospheric radiation budget and subsequently the perturbation of the Earth-Atmosphere system's
248 radiation budget (Eq. 4).

249
250 **“I. 596: does the model produce substantially different dust size distributions over the Sahara and**
251 **along the coast and in the Mediterranean? It might be interesting to show this effect.”**

252
253 In Figure R3 is depicted the geographical distribution of the coarse-to-fine ratio of dust aerosols, at 12
254 UTC on 2nd August 2012, which has been calculated by dividing the aggregated dust concentrations for
255 bins 5-8 (coarse particles) and bins 1-4 (fine particles). As expected, the maximum ratios (~ 19) are found
256 over/close the dust sources (central Algeria) whereas considerably high values (> 10) are observed in the
257 western parts of Sahara and over the Atlantic Ocean, both affected by the major dust plume (see Figure
258 4 in the manuscript).

259



260
261 **Figure R3:** Geographical distribution of coarse-to-fine ratio of dust aerosols at 12 UTC on 2nd August 2012.

262 **“section 5.3. the dust outbreak impact on SH and LE is investigated only over land. It may be**
263 **worth including in this section the discussion on the SH and LE changes in the marine environment**
264 **(l. 751-752). This is also needed to support the validity of the estimated temperature biases over**
265 **the ocean discussed in section 5.4.”**

266 As stated in lines 664-665, in the utilized version of NMMB-MONARCH model the atmospheric driver
267 is not coupled with an ocean model. Therefore, not a significant impact on SH and LE is expected over
268 maritime areas, since the feedbacks from ocean are neglected. In addition, due to the larger heat capacity
269 of sea (Lines 736 - 743), the perturbations of the SH and LE fields should be negligible at short temporal
270 scales. The aforementioned reasons explain why we have investigated the induced impacts on heat fluxes
271 (Section 5.3) only over land areas.

272
273
274 **“l. 734:- it may be worth recalling the AOD value which corresponds with these cross sections.”**

275
276 We have inserted in the text the maximum dust AODs at 550nm simulated by the NMMB-MONARCH
277 model along the cross-sections (see lines 732-733, lines 750-753).

278
279 **“l. 858: although pyrgeometers are sensitive to the wavelength range 4-50 micron or similar, they**
280 **are calibrated to provide LW irradiances integrated up to 100 micron.”**

281
282 We have taken this information from the specifications of the pyrgeometers (Eppley-PIR and Kipp &
283 Zonen CGR4) that are installed at BSRN stations. The spectral ranges of the measured downwelling LW
284 radiation at the ground span the wavelength range from 4 to 50 microns for Eppley-PIR and from 4.5 to
285 42 microns for Kipp & Zonen CGR4. Nevertheless, we haven't found any relevant reference regarding
286 the calibration procedure that extends the upper bound to 100 microns.

287
288 **“l. 796-803: how is the dust emission calculated? It should be mainly related to the wind intensity,**
289 **and it seems to me that such a large day/night difference may be explained only if the emission is**
290 **calculated as dust entrainment at some altitude above the ground”**

291
292 We have avoided in our paper to provide much information about the dust emission scheme since a
293 detailed description is given by Pérez et al. (2011). Briefly, the saltation of mineral particles is
294 approximately proportional to the third power of the wind speed. The vertical dust flux (F_k), constrained
295 by a tuning factor, is proportional to the horizontal flux. Based on F_k and turbulent regime, the

296 concentration of the emitted dust particles is diagnosed at the top of a viscous sublayer extending between
297 the assumed smooth desert surface and the lowest model layer. During day, due to thermal convection,
298 the turbulence is enhanced resulting thus to an unstable atmosphere, higher wind speeds and subsequently
299 to larger amounts of emitted dust. On the contrary, during night, the atmosphere is more stratified (less
300 turbulence) leading to weaker wind speeds and less dust emission. The strong variability of dust emission
301 throughout the day, presented in Figure 6-ii of our manuscript, has been also reported in previous studies
302 (e.g. Schepanski et al., 2009).
303

304 **“section 5.6: the verification of the data against surface radiation measurements is a very ambitious**
305 **task. As the authors state, it would require a very good model description of the dust event**
306 **evolution and spatial distribution, and a good reproduction of the observed AOD. I would suggest**
307 **shortening this section, removing the discussion of specific cases and figure 10, and presenting the**
308 **results as statistical means for all considered sites (a condensed version of table S1). Some of the**
309 **selected events have been previously investigated using satellite/ground based measurements, and**
310 **radiation transfer modelling (see e.g., Santese et al., 2010; Benas et al., 2011; di Sarra et al., 2011).**
311 **The authors may consider if it may be reasonable to compare the radiative effect estimates, instead**
312 **of the irradiances, obtained during some of these events.”**
313

314 We would like to remind that the goal of this study is not to evaluate the model’s radiative fluxes against
315 measurements, but to highlight the model improvement in terms of more adequately reproducing
316 radiative fluxes when it takes into account dust in its simulations. Thus, we prefer to keep Figure 10 and
317 the relevant discussion, since in both example cases (in Sede Boker) is nicely depicted (highlighted) the
318 role of factors affecting the level of agreement between NMMB and BSRN, by taking advantage of the
319 existing concurrent AERONET retrievals while the impact of clouds (relied on numerical simulations)
320 is also considered. It is the first time that such an evaluation analysis of the NMMB-MONARCH is
321 presented.

322 Regarding the last part of the reviewer’s comment, following his suggestion, we have compared our SW
323 DREs with the corresponding ones calculated in Benas et al. (2011) and the results are presented in Table
324 R1. The surface DREs (SURF, NETSURF) are comparable but lower (by up to 12 Wm^{-2} and 8 Wm^{-2} ,
325 respectively) in our analysis while the atmospheric warming in Benas et al. (2011) is 2.6 times higher
326 than ours. At TOA, our SW DRE reach down to -35 Wm^{-2} , being higher, in absolute terms, by 59% with
327 respect to Benas et al. (2011). A significant difference between the two studies, determining the DRE
328 calculations, is that in our case the AOD (0.09) and SSA (0.87) are very low in contrast to Benas et al.
329 (2011) where the corresponding values are equal to 0.44 and 0.95, respectively. Therefore, higher loads
330 are considered in Benas et al. (2011) whereas the suspended particles are more absorptive in our analysis.
331 Both facts interpret the differences found between the two studies. An additional source of differences is
332 that DREs in our calculations are representative 60 hours after the initialization of the model (00 UTC
333 24-Feb-2006) while they have been spatially averaged around the FORTH-CRETE AERONET station
334 (Latitude: 35° - 36° N, Longitude: 25° - 26° E). The increasing errors for increasing forecast time, as well
335 as spatially averaged NMMB DREs against almost local (MODIS’ nadir view $10 \times 10 \text{ km}$ spatial
336 resolution) estimates of DREs in Benas et al. produce differences when comparing our model to Benas
337 et al. (2011) DREs.
338

339 In di Sarra et al. (2011), the SW DREs are presented for 25th and 26th March 2010 while in our study case
340 the forecast run starts at 00 UTC on 27th March 2010.
341

342 In Santese et al. (2010), the daily averages of DREs are presented for 17th July 2003. In the revised
343 supplement document, we are providing the corresponding instantaneous (noon and night) DREs for the
344 same date in Figure S6 (third and fourth row).

345 **Table R1:** SW DREs at 11:25 UTC on 26-Feb-2006 (Benas et al. (2011)) and at 12 UTC on 26-Feb-2006 (present analysis)
346 over the FORTH-CRETE AERONET station (Crete, southern Greece).

	Benas et al. (2011) [11:25 UTC]	Present study [12:00 UTC]
TOA	-22 Wm ⁻²	-35 Wm ⁻²
SURF	-66 Wm ⁻²	-54 Wm ⁻²
NETSURF	-56 Wm ⁻²	-48 Wm ⁻²
ATM	34 Wm ⁻²	13 Wm ⁻²

348
349
350 **“I. 859: I assume that emission from atmospheric gases and from the surface is not included in the**
351 **way the SW radiation (up to 12.2. microns) is calculated. This might be clarified.”**

352 In the existing version of the NMMB-MONARCH model, only greenhouse gases and not the emitted
353 short lived atmospheric gases are taken into account. We have added the relevant information in the text
354 (Lines 267-268).

355 356 **References**

357
358 **Benas, N., N. Hatzianastassiou, C. Matsoukas, A. Fotiadi, N. Mihalopoulos, and I. Vardavas (2011),**
359 **Aerosol shortwave direct radiative effect and forcing based on MODIS Level 2 data in the Eastern**
360 **Mediterranean (Crete), Atmos. Chem. Phys., 11, 12647-12662.**

361
362 **di Sarra, A., C. Di Biagio, D. Meloni, F. Monteleone, G. Pace, S. Pugnaghi, and D. Sferlazzo (2011),**
363 **Shortwave and longwave radiative effects of the intense Saharan dust event of 25-26 March, 2010,**
364 **at Lampedusa (Mediterranean Sea), J. Geophys. Res., 116, D23209, doi: 10.1029/2011JD016238.**

365
366 **Santese, M., M. R. Perrone, A. S. Zaakey, F. De Tomasi, and F. Giorgi (2010), Modeling of Saharan**
367 **dust outbreaks over the Mediterranean by RegCM3: Case studies, Atmos. Chem. Phys., 10, 133-**
368 **156.**

369
370
371
372
373
374
375
376
377
378
379
380

381
382

Response to Reviewer3

383 We would like to thank the Reviewer who helped us to improve our paper through his/her report. Below
384 are listed our detailed responses (regular font) to each comment raised by the Reviewer (bold font).

385 **The paper presents an interesting study for calculating DRE with the use of the NNMB-**
386 **MONARCH model (NNMB). It is a well written paper which with the following revisions it could**
387 **be published in the ACP journal. My main comments are:**

388 **- In order to accept the results of such a study, a more comprehensive validation of the presented**
389 **outputs using real measurements and an analysis of the uncertainties introduces in several phases**
390 **of the method have to be presented.**

391 In the revised manuscript we have made a more detailed comparison between MODIS-NMNB for the
392 cases (dust outbreaks) which are analyzed here. Regarding the validation of radiation and temperature
393 fields, the discussion has been updated whenever is needed. Please see our responses to your comments
394 below.

395 **- A major aspect of the paper is not clarified. The abstracts talks about DRE and as the authors**
396 **point out this is mostly aerosol optical depth (AOD) dependent. MODIS retrieves total (dust +**
397 **other types) AOD while NNMB only dust AOD (that is what is shown throughout the text and in**
398 **e.g. figure 3). So the authors have to clarify if they talk about Dust DRE or DRE. If someone**
399 **assumes that these 20 events are purely dust events, an AOD comparison of MODIS AOD and**
400 **NNMB AODs have to be included (not quantitatively as in fig. 3), in order try to assess the model**
401 **results.**

402 We have changed the title of our paper from “*Direct radiative effects of intense Mediterranean desert*
403 *dust outbreaks*” to “*Direct radiative effects during intense Mediterranean desert dust outbreaks*” so that
404 the goal of our study is more clear. This modification has been made since based on the configuration of
405 the model the amount of dust aerosols is simulated dynamically (online) while for the other aerosol types
406 the GOCART climatology is used (Lines 340-342). Moreover, the DREs are computed for days in which
407 intense dust outbreaks prevail over the greater Mediterranean basin. Under such conditions, and over
408 places where Saharan dust is transported, dust predominates and is the main contributor of AOD, even
409 in MODIS AOD retrievals. Of course, in such cases all aerosol types exert a perturbation of the radiation
410 budget, but the impact of mineral particles is predominant. A quantitative comparison between MODIS
411 and NNMB has been made (suggested also by the Reviewer 2) and the obtained results are presented in
412 Figure S2 (supplementary material) and discussed in Section 5.1.

413 **- A major issue of the paper is the link between the NNMB results and the Gkikas et al.,**
414 **methodology (GM) for identifying dust episodes. Some questions that have to be clarified on the**
415 **manuscript are the following:**

416 **(i) Are the domains seen in figure 3 and 1 have been used in the GM for all the episodes that are**
417 **presented in the table 1? Is there a mix of surface and sea Modis pixels used?**

418 The identification of DD episodes through the implementation of the satellite algorithm is made only for
419 the Mediterranean Satellite Domain (MSD, red rectangle in Figure 1) as stated in the manuscript (see
420 lines 192-194). The structure, methodology, and operational phases of the satellite algorithm have been

421 presented in detail by Gkikas et al. (2013, <https://www.atmos-chem-phys.net/13/12135/2013/>). Briefly,
422 the algorithm operates separately over land and sea surfaces by taking into account the MODIS AODs
423 obtained by the dark target land and ocean retrieval algorithms. Therefore, the number of DD episodes
424 presented in Table 1 corresponds to the number of grid cells ($1^\circ \times 1^\circ$ spatial resolution) where a desert
425 dust (DD) episode has been recorded/identified within the geographical limits of the MSD. Please see
426 lines 207-210 and the caption of Table 1 in the revised manuscript.

427 **(ii) When GM identifies an episode (e.g. example of figure 3) are the DRE calculations of NNMB**
428 **account only the relative (episodic) modis pixels? I think the answer here is no but it has to be**
429 **clarified. So, If the answer is no (thus the whole domain (e.g. MSD) is used for NNMB) then the**
430 **importance of the GM episode identification is only partially valid. (e.g. a lot of white in fig. 3 are**
431 **used based only on NNMB and not on GM). As identifying an episode in a limited area in the MSD**
432 **domain does not mean that this is valid for the whole domain.**

433 We think that it is clear that the NNMB DREs calculations are made all over the Mediterranean basin
434 and not only over the episodic MODIS pixels. This does not limit the validity and importance of GM
435 dust episode identification. It is self evident that when talking about a dust episode over the
436 Mediterranean, not the entire basin but just a significant part of it is expected to be dominated by dust,
437 which is adequately ensured by GM. Therefore, having “a lot of white in Fig. 3” is not strange,
438 unreasonable or problematic, but on the contrary it is expected and sound. Nevertheless, this does not
439 prevent us from talking about Mediterranean dust episodes and radiative effects (DREs). The only issue
440 that might be relevant to this comment, is averaging regionally over the Mediterranean, where dust and
441 no dust dominated areas are considered together, but even in such cases DRE computations are
442 meaningful. In the revised manuscript, the calculations of the regional DREs have been made taking into
443 account all the grid points and therefore the spatial representativeness is consistent at each forecast step
444 and among the studied cases.

445 **(iii) If the whole domain is used are results of table 1 dependent in addition to dust AOD to the**
446 **spatial extension of the event? Can a number of different episodes with different spatial extends**
447 **and AODs, averaged (table 2)**

448 In the revised manuscript (Table 1, lines 213-218) it is explained that the frequency and regional intensity,
449 i.e. AOD of 20 dust outbreaks, is calculated from the total pixel-level DD episodes, therefore the results
450 of Table 1, more specifically the intensity, are not dependent on the spatial extend of the episodes. As
451 already answered in the previous comment, regional DREs can be computed for every dust episode.
452 Therefore, as it concerns the second part (sentence) of this comment (e.g. Table 2 results) we believe that
453 averaging DREs over the 20 different dust episodes is meaningful and representative of DREs during
454 Mediterranean dust outbreaks.

455 **Another example of the last point above is that modis GM detects a plume (high AOD) covering**
456 **very few pixels in the western part of MSD (for example last row of figure 3). Then based on GM**
457 **the whole MSD domain is considered as the one that will provide the DRE. In this case the link on**
458 **GM used as a proxy in this work is very weak as it covers only a small part of the domain, plus**
459 **AODs are not compared. So also a number of episodic pixels should be included in these GM dust**
460 **episode restrictions. Or simply dust outbreak identification can be based on NNMB spatial and**
461 **NNMB-AOD absolute criteria as now the link with GM is really weak.**

462 Most of the content of this comment has already been answered. However, we would like to note that of
463 course intense dust outbreaks are not supposed to cover the entire Mediterranean, on the contrary, they
464 always cover a part of it, this is logical. However, this does not prevent us of talking about dust episodic
465 days over the Mediterranean basin whenever such dust outbreaks occur. And, moreover, it also does not
466 prevent us from computing DREs all over the Mediterranean basin, even averaging over it. Therefore,
467 there is not any problematic link in our concept and methodology combining the detection of dust
468 outbreaks with GM and the DRE computation with NNMB. Concerning the last sentence and suggestion
469 of the Referee, of course this is an option, i.e. dealing with detection of dust outbreaks and computing
470 the associated DREs solely using the NNMB model. However, this would be purely theoretical. On the
471 opposite, detecting intense dust outbreaks based on an observational approach, i.e. using MODIS
472 products, is more appropriate. Finally, as already stated in our responses to this Referee's previous
473 comments, a comparison of AODs has been made and it is discussed in the revised version of the
474 manuscript.

475 **In addition, in this case (and others e.g. west domain of fig. 3b) NNMB dust pixels cover less than**
476 **50% of the MSD. When averaging the 20 cases this percentage of pixels varies a lot. In the end**
477 **you are averaging and provide a result e.g. SW = -9.7. So some of the outbreaks contribute much**
478 **more and some others not, based on the dust coverage on the MSD only. Where can such statistics**
479 **be used?**

480 First, we would like to state that in the revised manuscript the regional DREs have been calculated
481 considering all the grid points without setting any criterion on the simulated dust AOD or on clouds (this
482 approach was initially followed). Therefore, at each forecast step and among the 20 desert dust outbreaks
483 the number of grid points is constant. This ensures that the spatial representativeness of the regional
484 DREs does not vary in time and among the studied cases (Figure 5).

485 **To summarize, if GM is not used for AOD validation and GM identifies as “dust episodic pixels”**
486 **only a fraction of the pixels used finally from NNMB for calculating dust DRE, then its use becomes**
487 **not important for this study. So if someone trusts NNMB for DRE calculations, then it is much**
488 **more easy to trust it also for dust outbreak identification.**

489 We think that our previous responses give a sufficient answer to the reviewer's summary comment.

490 **- There are more than 100 references and a lot of discussion about aerosol effects and model**
491 **applications, but very few about NNMB validation on e.g. AOD retrievals. And only one**
492 **(Ohmura) on BSRN radiation related validation. I think it is more essential to prove the validity**
493 **of AOD NNMB output (e.g. radiation) and intermediate parameters (e.g. AOD), than a numerous**
494 **studies cited here, with a very theoretical link to the paper.**

495 It is not the first time that NNMB is used, so validation of its AOD has already been done. In our paper,
496 we have included all the available studies regarding the evaluation of the simulated AODs relied on the
497 same NNMB version which is used here (Lines 294-306). Moreover, in the revised manuscript we are
498 providing the weblink of the SDS-WAS System (<https://sds-was.aemet.es/forecast-products/forecast-evaluation>) in which is presented the forecast evaluation of NNMB AODs, among other aerosol models,
499 utilizing ground-based (AERONET) and satellite (MODIS) retrievals as reference.
500

501 Concerning BSRN, we would like to remind and underline that it provides just reference radiation
502 measurements. The BSRN is considered the best global network of quality radiation measurements.

503 There is a very high number of scientific papers ([http://bsrn.awi.de/other/publications/reviewed-](http://bsrn.awi.de/other/publications/reviewed-scientific-papers-referring-to-bsrn/)
504 [scientific-papers-referring-to-bsrn/](http://bsrn.awi.de/other/publications/reviewed-scientific-papers-referring-to-bsrn/)) or reports ([http://bsrn.awi.de/other/publications/other-related-](http://bsrn.awi.de/other/publications/other-related-reports-and-papers/)
505 [reports-and-papers/](http://bsrn.awi.de/other/publications/other-related-reports-and-papers/)) referring to BSRN, so there is no need to make further reference to it than to the key
506 paper of Ohmura et al. (1998) which is commonly used as reference for BSRN data. The validity of
507 NMMB radiation fluxes is exactly proved through their comparison against BSRN measurements.

508 **- The validation using BSRN is incomplete. In the document and in the abstract you are talking**
509 **about this validation and 8 stations. Then in the manuscript only one station is shown. And from**
510 **that only 4 days. In order to validate the results a more comprehensive analysis of long term periods**
511 **of these 8 stations is needed. Probably Ohmura has answered some of the validation related**
512 **questions, but this paper focuses on “intense dust outbreaks”, and a specific model, so results might**
513 **differ from the Ohmura related ones.**

514 We would like to point out that the calculated biases (NMMB-BSRN) over the hindcast periods, for each
515 case and for each station (6 in total), are given already for the SW and LW radiation in Tables S2 and
516 S3, respectively and discussion (lines 882-887) refers to their results. In the main text, we have decided
517 to present just as an example the obtained results for the SW (first row in Figure 10) and LW (second
518 row in Figure 10) radiation for two dust outbreaks (22/2 -25/2/2004 and 21/4-24/4/2007) that affected
519 the Sede Boker station, for which concurrent AERONET retrievals were available. This allows us to give
520 a better insight regarding the factors that can affect the level of agreement between model and ground
521 observations. We agree with the reviewer that a long-term evaluation is valuable (i.e. identification of
522 systematic errors) but for our purpose focus is given only on specific desert dust outbreaks trying to
523 investigate if the inclusion of dust-radiation interaction in the numerical simulations can improve the
524 forecasting skills of the NMMB-MONARCH model.

525 **- There are several issues that have to be clarified/commented on the input parameters of the**
526 **model:**

527 **(i) Optical properties proposed in figure 2. Have been validated?**

528 The optical properties have not been validated. The model dust optical properties are based on single-
529 particle optical properties derived by the GOCART model (Chin et al., 2002) and refractive indices from
530 the Global Aerosol Data Set (GADS) (Koepke et al., 1997). Both datasets are very well known and very
531 much often used and cited in literature, and therefore we believe that there is no need for further
532 validation here.

533 **(ii) Water vapor, carbon dioxide, ozone, methane and oxygen. Where do you find these inputs?**

534 Water vapor comes from the model simulations. We used a fixed value of CO₂ (350 ppm), methane (1.5
535 ppm) and oxygen; and a seasonal climatology for ozone.

536 **(iii) Differences in dust optical properties of Sahara and middle East sources. What did you use**
537 **and how much uncertain are they? and what is the contribution of this uncertainty in the final**
538 **DRE budget?**

539 The dust single-particle optical properties and the emitted size distribution are constant throughout the
540 simulation domain without discriminating between different dust sources (Sahara, Middle East). At each
541 forecast step, the aerosol optical depth (AOD), the single scattering albedo (SSA) and the asymmetry
542 parameter (ASYM) have been produced based on the formulas presented in Pérez et al. (2006) utilizing

543 the simulated mass concentration, the GOCART single-particle optical properties and the refractive
544 indices from the Global Aerosol Data Set (GADS) which have been modified according to Sinyuk et al.
545 (2003), as it has been described in Pérez et al. (2011) (lines 331-336). Regarding the last question of the
546 reviewer, in order to be give an accurate answer a sensitivity analysis is required. More specifically, it
547 must be investigated how the variation of key aerosol optical properties (AOD, SSA and ASYM) will
548 affect the perturbations of the radiation budget and subsequently the associated impacts on dust AOD,
549 dust emission, meteorological variables and radiation. This is something that has not been done in the
550 present paper but it will be considered in a future work dedicated to all the aforementioned aspects
551 considering also other parameters (e.g., dust layer vertical extension) which can affect DREs.

552 **- BSRN and model differences in wavelength integrals of solar radiation. You mention: “These**
553 **differences might contribute to the level of agreement between model and observations; however,**
554 **are not discussed in our evaluation analysis”. I think this is an important issue that have to be**
555 **clearly discussed if a proper validation is included.**

556 For solar radiation, the NMMB-BSRN SW flux departures, attributed to the different spectral coverage
557 and integrals, are minor, varying from 1 to 1.5 % (higher values for the model), therefore they do not
558 affect substantially the agreement (in terms of biases) between model and measured fluxes.

559 **- As already mentioned AOD comparisons from MODIS and NNMB could add value to this work.**
560 **“The model’s ability to reproduce correctly the spatial patterns and values of dust AODs is crucial**
561 **for a successful computation of the dust DREs, since DREs are determined to a large extent by**
562 **AOD”. In addition you are mentioning modis uncertainty in section 2. Is this getting high (e.g. ~**
563 **0.5) for both sea and mostly surface retrievals when you examine AODs in the order of 2-3 based**
564 **on the table 1? And is this uncertainty already important for such outbreaks for the GM and**
565 **indirectly for the DRE related uncertainty?**

566 Actually, the uncertainty of C051 MODIS AOD retrievals is not reported in section 2, where only the
567 detection of dust outbreaks is described. The uncertainty of MODIS AOD retrievals over ocean is
568 $\pm 0.03 \pm 0.05 * AOD$ (Remer et al., 2002) while over land is higher and equal to $\pm 0.05 \pm 0.15 * AOD$ (Levy
569 et al., 2010). The maximum MODIS retrieved AOD, over both continental and maritime areas, do not
570 exceed 5, which means that the AOD uncertainties above sea and land, in absolute terms, are smaller
571 than 0.28 and 0.8, respectively. In our cases, but also in general, these maximum AOD uncertainties are
572 locally restricted and not recorded frequently (see Figures 3 and S1) while uncertainties are generally
573 smaller, and thus do not affect the GM. Moreover, they neither affect DREs, since as already explained
574 in our previous responses and in the manuscript, the DREs have been computed via the NMMB
575 simulations without setting any constrain depending on MODIS retrievals (i.e., availability, magnitude).

576 **- Table 2. These statistics are not referring to the model uncertainty but is an averaging of the**
577 **episodes provided by the GM. NNMB DRE uncertainty is much more useful for any future user of**
578 **these results. For example a systematic bias can not be identified here. This is also because the GM**
579 **thresholds are mostly subjective as:**

580 **(i) Mean AOD values on dust related areas do not have an important statistical meaning due to the**
581 **non normal distribution of AOD. It is clear that this is a published work and I have tried to follow**
582 **the previous work by Gkikas et al and the relative open discussion, describing the method.**
583 **However, as this is an open public statement I have to comment that AOD does not follow**

584 **necessarily a normal distribution so using the mean is not absolutely correct. Moreover, dust**
585 **outbreaks related pixels/locations can be characterized more from a bimodal distribution of AODs**
586 **when another (than dust) important AOD source is rarely present (e.g. most of the marine grids of**
587 **Mediterranean domain).**

588 First of all, as stated by the Referee, we would like to remind that the GM method has already been
589 published (Gkikas et al., 2013; 2016) just after the discussion that took place concerning the way of
590 computation of AOD thresholds, i.e. geometric versus arithmetic mean AOD values, which implies its
591 validity against similar arguments cited in this comment. Nevertheless, we can remind the following. We
592 agree with the Reviewer that AOD follows a log-normal rather than a Gaussian distribution, and that the
593 arithmetic mean and standard deviation are not probably the best metrics for the calculation of the AOD
594 thresholds, even though both primary statistics are widely applied in numerous aerosol studies. During
595 the review process of Gkikas et al. (2013), following a similar comment raised by one of the referees,
596 proposing to calculate the AOD thresholds based on the geometric mean and geometric standard
597 deviation, we recomputed the AOD thresholds and compared them to the typical ones already used (based
598 on arithmetic mean and standard deviation). Although there were found some differences in the
599 thresholds' magnitude, in general, the geographical patterns of AOD thresholds were similar for both
600 strong and extreme DD episodes. As for strong episodes, those differences were rather small, for example
601 typical AOD thresholds varied within the range 0.4-1.2 and the geometrical thresholds ranged from 0.4
602 to 1.6. On the other hand, larger differences existed for extreme DD episodes, with the typical thresholds
603 ranging from 0.6 to 2.2 while the geometric ones varying from 1 to more than 10. However, such
604 extremely high AOD values are extremely rare and using them would be unrealistic from the physical
605 point of view. For these reasons, it was decided to rely on GM methodology of Gkikas et al. (2013).

606 **(ii) GM: By definition high mean AOD values per pixel are closer to dust sources. That makes**
607 **possible that a pixel with high (in an absolute sense) AOD close to a dust source to be considered**
608 **non episodic and a pixel with lower AOD, away from the sources to be considered episodic. This**
609 **is ok, as it is just a matter of definition. But it gets more important when it is used for DRE**
610 **calculations. So, the latest can be problematic when you calculate DRE in dust outbreaks or filter**
611 **the outbreaks, as for the first example pixel (high AOD) it is not an outbreak and for the second**
612 **(lower AOD) it is characterized as an outbreak. The results using this method for DRE calculations**
613 **become not easily useful and applicable.**

614 The issue of the identification method of DD outbreaks based on pixel-level AOD values, has already
615 been addressed in our previous papers using the GM methodology, following similar comments to the
616 one made by the Referee here. It has been shown that any differences in terms of AOD thresholds and
617 dust outbreaks features (frequency, intensity) were not substantial.

618 However, the most important concerning the rest of Referee's comment referring to possible effects of
619 this issue on computed DREs here, we would like to clarify again that DREs are computed by NMMB
620 and have nothing to do with the AOD thresholds. It should be clear and kept in mind that GM
621 methodology is only used for the determination of days with intense dust outbreaks for which NMMB
622 then operates and makes computations of DREs all over the domain.

623 **- Last but very important, the paper is very long and in various cases the discussion includes a lot**
624 **of details that in the end confuse the reader on what is the important findings here and which are**
625 **not. Even for scientists in the field it becomes difficult to read. Authors have to try to reduce the**

626 **length of the manuscript keeping the important aspects of the results presented. Basically for**
627 **section 5 I would suggest to try to take out a lot of information that are secondary and to focus on**
628 **the important results.**

629 In the revised manuscript, following the suggestion of the Reviewer, we made an effort and reduced the
630 paper length by removing some parts which can be considered as secondary information. However, at
631 the same time, also following the Reviewers' suggestions, we added a discussion about the quantitative
632 intercomparison between MODIS and NMMB as well as about the potential improvements on short-term
633 forecasts of the temperature fields by the model. Therefore, the final length of the revised manuscript is
634 similar to that of the original manuscript. We believe that any further shortening of the manuscript would
635 be at the expense of its quality and scientific content.

636 **Minor comments:**

637 **Line 141: it has already mentioned previously.**

638 It has been modified.

639 **Line 173: developed – improved**

640 Done.

641 **Table 1: episodes = grid cells**

642 We think that is already clearly stated in the caption.

643 **The overall approach of this paper is valuable and worth publishing. I strongly believe that after**
644 **the above revisions, corrections and additional analysis it will be essentially upgraded and then it**
645 **could be published in the ACP journal.**

646

647

648

649

650

651

652

653

654

655

656

657

658

659

660

Direct radiative effects during intense Mediterranean desert dust outbreaks

Antonis Gkikas^{1,2}, Vincenzo Obiso², Carlos Pérez García-Pando², Oriol Jorba², Nikos Hatzianastassiou³, Lluís Vendrell², Sara Basart², Stavros Solomos¹, Santiago Gassó⁴ and José María Baldasano^{2,4}

¹Institute for Astronomy, Astrophysics, Space Applications and Remote Sensing, National Observatory of Athens, Athens, 15236, Greece

²Earth Sciences Department, Barcelona Supercomputing Center, Barcelona, Spain

³Laboratory of Meteorology, Department of Physics, University of Ioannina, Ioannina, Greece

⁴Environmental Modelling Laboratory, Technical University of Catalonia, Barcelona, Spain

Corresponding author: Antonis Gkikas (agkikas@noa.gr)

Abstract

The direct radiative effect (DRE) during 20 intense and widespread dust outbreaks that affected the broader Mediterranean basin over the period March 2000 – February 2013, has been calculated with the NMMB-MONARCH model at regional (Sahara and European continent) and short range temporal (84 h) scales. According to model simulations, the maximum dust aerosol optical depths (AODs) range from ~2.5 to ~5.5 among the identified cases. At midday, dust outbreaks induce locally a NET (shortwave plus longwave) strong atmospheric warming (DRE_{ATM} values up to 285 Wm⁻²; Niger-Chad; dust AODs up to ~5.5), a strong surface cooling (DRE_{NETSURF} values down to -337 Wm⁻²) whereas they strongly reduce the downward radiation at the ground (DRE_{SURF} values down to -589 Wm⁻² over the Eastern Mediterranean, for extremely high dust AODs, 4.5 – 5). During nighttime, reverse effects of smaller magnitude are found. At the top of the atmosphere (TOA), positive (planetary warming) DREs up to 85 Wm⁻² are found over highly reflective surfaces (Niger-Chad; dust AODs up to ~5.5) while negative (planetary cooling) DREs down to -184 Wm⁻² (Eastern Mediterranean; dust AODs 4.5 – 5) are computed over dark surfaces at noon. Dust outbreaks significantly affect the mean regional radiation budget, with NET DREs ranging from -8.5 to 0.5 Wm⁻², from -31.6 to 2.1 Wm⁻², from -22.2 to 2.2 Wm⁻² and from -1.7 to 20.4 Wm⁻² for TOA, SURF, NETSURF and ATM, respectively. Although the shortwave DREs are larger than the longwave ones, the latter are comparable or even larger at TOA, particularly over the Sahara at midday. As a response to the strong surface daytime cooling, dust outbreaks cause a reduction of the regional sensible and latent heat fluxes by up to 45 Wm⁻² and 4 Wm⁻², respectively, averaged over

Deleted: of

Formatted: Justified

Deleted: of

Deleted: during

Deleted: regional

Deleted: The DREs have been calculated based on short-term simulations (84 hours) for a domain covering the Sahara and most part of the European continent.

Deleted: desert

Deleted:) in areas (

Deleted:)

Deleted: affected by

Deleted: (

Deleted: esert d

Deleted: regional clear-sky

Deleted: values

Deleted: 13

Deleted: 9

Deleted: 2

Deleted: 6

Deleted: 43

Deleted: 4

Deleted: 6

Deleted: 3

Deleted: 3

Deleted: 9

Deleted: 3

Deleted: 28

Deleted: (SW)

Deleted: (LW)

Deleted: during daytime

726 land areas of the simulation domain. Dust outbreaks reduce the temperature at 2 meters by up to 4 K
727 during daytime, whereas a reverse tendency of similar magnitude is found during nighttime. Depending
728 on the vertical distribution of dust loads and time, mineral particles heat (cool) the atmosphere by up to
729 0.9 K (0.8 K) during daytime (nighttime) within atmospheric dust layers. Beneath and above the dust
730 clouds, mineral particles cool (warm) the atmosphere by up to 1.3 K (1.2 K) at noon (night). On a regional
731 mean basis, negative feedbacks on the total emitted dust (reduced by 19.5 %) and dust AOD (reduced by
732 6.9 %) are found when dust interacts with the radiation. Through the consideration of dust radiative
733 effects in numerical simulations, the model positive/negative biases for the downward surface SW/LW
734 radiation, with respect to Baseline Surface Radiation Network (BSRN) measurements, are reduced. In
735 addition, they also reduce the model near-surface (at 2 meters) nocturnal cold biases by up to 0.5 K
736 (regional averages), as well as the model warm biases at 950 and 700 hPa, where the dust concentration
737 is maximized, by up to 0.4 K. However, improvements are relatively small and do not happen in all
738 episodes because other model first order errors may dominate over the expected improvements, and the
739 misrepresentation of the dust plumes' spatiotemporal features and optical properties may even produce
740 a double penalty effect. The enhancement of dust forecasts via data assimilation techniques may
741 significantly improve the results.

742 1. Introduction

743 Dust aerosols through their interaction with the incoming solar (shortwave, SW) and the outgoing
744 terrestrial (longwave, LW) radiation, perturb the radiation budget of the Earth-Atmosphere system and
745 redistribute the energy therein. The induced perturbation of the radiation fields by dust particles, the so-
746 called dust radiative effect, takes place through three processes of increasing complexity affecting the
747 energy budgets at the surface, into the atmosphere and at the top of the atmosphere (TOA). The first one,
748 known as direct radiative effect (DRE) and referred as REari (aerosol-radiation interactions) in the latest
749 report of the Intergovernmental Panel on Climate Change (IPCC, Boucher et al., 2013), is caused by the
750 absorption and scattering of the SW radiation (Sokolik et al., 2001) and the absorption and re-emission
751 of the LW radiation by mineral particles (Heinold et al., 2008). Due to the perturbation of the radiation
752 fields by dust aerosols, the energy budget both at the surface and into the atmosphere is modified and the
753 signal of these impacts is evident in atmospheric stability/instability conditions associated with cloud
754 development and precipitation. These rapid adjustments, which have been earlier referred as semi-direct
755 effects (Hansen et al., 1997), are induced by the dust REari on surface energy budget and atmospheric
756 profile (Boucher et al., 2013) contributing to the Effective Radiative Forcing (ERFari). Moreover, dust
757
758

Deleted: When dust radiative effects are taken into account in numerical simulations, the total emitted dust and dust AOD, computed on a regional mean basis, are decreased (negative feedback) by 19.5% and 6.9%. The

Deleted: improves the model predictive skills. More specifically, it reduces

Deleted: and

Deleted: and

Deleted: respectively,

768 aerosols due to their ability to serve as cloud condensation nuclei (CCN) and ice nuclei (IN), modify the
769 physical (Twomey, 1974; Albrecht, 1989) and optical properties of clouds (Pincus and Baker, 1994),
770 which consist the major regulators of the Earth-Atmosphere system's radiation budget (Lohmann and
771 Feicher, 2005). This chain of complex processes, involving aerosol-cloud-interactions (ACI) and the
772 subsequent modifications of the radiation fields, constitute the indirect impact of mineral particles on
773 radiation, which is characterized by the largest uncertainties, even larger than those of the dust direct and
774 semi-direct effects. In the latest IPCC report (IPCC, 2013), the formerly known as indirect effects have
775 been renamed to Effective Radiative Forcing (ERF_{aci}) including the modification of radiation by clouds
776 as well as the subsequent changes (rapid adjustments) of clouds' physical/microphysical/optical
777 properties (Boucher et al., 2013).

778 Several studies have been conducted aiming at estimating the dust direct/semi-direct (e.g. Pérez et al.,
779 2006; Helmert et al., 2007; Zhao et al., 2010; Nabat et al., 2015a) and indirect effects (e.g. Sassen et al.,
780 2003; Seigel et al., 2013). Specifically, numerous studies have been carried out either by means of
781 numerical modelling (e.g. Solmon et al., 2012; Woodage and Woodward, 2014) or through the synergy
782 of observations and radiative transfer codes (Di Sarra et al., 2011; Valenzuela et al., 2012) or solely based
783 on aerosol observations (e.g. Yang et al., 2009; Zhang et al., 2016) and their findings either referred to
784 extended (e.g. Spyrou et al., 2013) or limited time periods (e.g. Nabat et al., 2015b) or to specific desert
785 dust outbreaks (e.g. Pérez et al., 2006; Santese et al., 2010; Stanelle et al., 2010). The investigation of
786 dust radiative effects is a scientific issue of great concern since it is documented that mineral particles,
787 through their interaction with the radiation, can affect atmospheric processes from short (weather) to long
788 (climate) temporal scales. To this aim, many research efforts were dedicated to the investigation of dust
789 impacts on the convective activity (Mallet et al., 2009), sea surface temperature (Foltz and McPhaden,
790 2008), hydrological cycle (Miller et al., 2004b), hurricanes (Bretl et al., 2015), boundary layer dynamics
791 (Heinold et al., 2008) and monsoons (Solmon et al., 2008; Vinoj et al., 2014).

792 The direct impact of dust aerosols is expressed by the sign and the magnitude of the DRE values,
793 which are defined as the anomalies (perturbation) of the radiation fields attributed to dust-radiation direct
794 interaction, considering as a reference (control) an atmospheric state where mineral particles are not a
795 radiatively active substance. Based on this, negative and positive DREs indicate a cooling (loss of energy)
796 and a warming effect (gain of energy), respectively. Nevertheless, the sign of the DREs varies between
797 the SW and LW spectrum (Osborne et al., 2011) as well as within the Earth-Atmosphere system. More
798 specifically, due to the attenuation (through scattering and absorption) of the SW radiation, dust aerosols
799 warm the atmosphere and cool the surface (Huang et al., 2014), while reverse tendencies are revealed at

- Deleted: through t
- Deleted: it is described
- Deleted: the
- Deleted: and compared to the other two dust radiative effects (i.e., direct and semi-direct)
- Deleted:
- Deleted: uncertainties
- Deleted: , attributed to aerosol-cloud interactions (aci),

808 longer wavelengths attributed to the absorption and re-emission of LW radiation by the mineral particles
809 (Sicard et al., 2014a). Between the two spectrum ranges, the SW DREs are larger compared to the LW
810 ones, in absolute terms, explaining thus their predominance when the corresponding calculations are
811 made for the NET (SW+LW) radiation (e.g. Pérez et al., 2006; Zhu et al., 2007; Woodage and Woodward,
812 2014). The perturbations of the radiation budget at the surface and into the atmosphere determine the
813 DRE at TOA (e.g. Kumar et al., 2014), which indicates the increase (planetary cooling) or the decrease
814 (planetary warming) of the outgoing radiation from the Earth-Atmosphere system and is relevant to dust
815 climatic effects (Christopher and Jones, 2007).

816 The scientific importance of investigating the dust direct impacts on radiation has been notified in
817 previous studies where it was shown that the consideration of the dust-radiation interactions may improve
818 the forecasting ability of weather models (Pérez et al., 2006) and can reduce the observed biases of the
819 LW radiation at TOA between models and satellite retrievals (Haywood et al., 2005). The dust direct
820 impacts are highly variable both in space (e.g. Zhao et al., 2010) and time (e.g. Osipov et al., 2015)
821 attributed to several parameters related either to dust aerosols' physical and optical properties or to
822 external factors (e.g. surface type), which determine both the sign and the magnitude of the DREs (Liao
823 and Seinfeld, 1998). One of the most important factor is the composition of mineral particles determining
824 the spectral variation of the refractive index (Müller et al., 2009; Petzold et al., 2009; Perlwitz et al.,
825 2015a, b; Pérez García-Pando et al., 2016) and subsequently their absorption efficiency (Mallet et al.,
826 2009), which are both critical in radiation transfer studies, and are also dependent on the mixing state
827 (either external or internal) of dust aerosols (Scarnato et al., 2015). Under clear skies, apart from mineral
828 particles' optical properties, the shape (Wang et al., 2013a), the emitted dust size distribution (Mahowald
829 et al., 2014), the surface albedo (Tegen et al., 2010) as well as the vertical distribution of dust aerosols
830 (Mishra et al., 2015) have been recognized as determinant factors for the DRE calculation. On the
831 contrary, when clouds are present, the position of dust layers with regards to clouds defines the sign and
832 the magnitude of DREs at TOA (Yorks et al., 2009; Meyer et al., 2013; Choobari et al., 2014; Zhang et
833 al., 2014).

834 The dust radiative effects become important under specific conditions of very high concentrations, so-
835 called events or episodes or outbreaks. Such episodes occur frequently over the broader Mediterranean
836 basin (Gkikas et al., 2013), due to its vicinity to the world's major dust sources situated across the
837 northern Africa (Sahara) and Middle East deserts (Ginoux et al., 2012). Dust particles are mobilized over
838 these areas by strong winds (Schepanski et al., 2009) being uplifted to the free troposphere due to strong
839 convection in the boundary layer (Cuesta et al., 2009) and are transported towards the Mediterranean due

Deleted: et al.

841 to the prevailing synoptic circulation (Gkikas et al., 2015). Under these conditions, dust particles over
842 the Mediterranean are recorded at very high concentrations as it has been confirmed either by satellite
843 (e.g. Moulin et al., 1998; Guerrero-Rascado et al., 2009; Rémy et al., 2015) and ground retrievals (e.g.
844 Kubilay et al., 2003; Toledano et al., 2007) or by surface PM₁₀ measurements (e.g. Rodríguez et al.,
845 2001; Querol et al., 2009; Pey et al., 2013).

Deleted: atmospheric (synoptic)

846 Among the different aerosol types that co-exist in the Mediterranean (Lelieveld et al., 2002; Basart et
847 al., 2009), dust is the one causing the greatest perturbation of the SW and LW radiation, especially during
848 desert dust outbreaks (e.g. Di Sarra et al., 2008; Di Biagio et al., 2010). Thus, a number of studies focused
849 on Mediterranean dust outbreaks' impacts on the SW (Meloni et al., 2004; Gómez-Amoet al., 2011;
850 Antón et al., 2012; Di Sarra et al., 2013; Obregón et al., 2015), LW (Antón et al., 2014; Sicard et al.,
851 2014a) and NET (Di Sarra et al., 2011; Romano et al., 2016) radiation. However, the obtained results
852 were representative at a local scale and considering the high spatial variability of desert dust outbreaks,
853 the optimum solution of assessing in a comprehensive way their impacts on weather and climate is
854 provided by atmospheric-dust models. To this aim, the induced DREs by the Mediterranean desert dust
855 outbreaks have been analyzed through short-term numerical simulations (Pérez et al., 2006; Santese et
856 al., 2010; Remy et al., 2015) while similar studies have been conducted either at a seasonal (Nabat et al.,
857 2015a) and annual scale (Nabat et al., 2012) or for extended time periods (Spyrou et al., 2013; Nabat et
858 al., 2015b) pointing out the key role of desert dust aerosols in the Mediterranean climate.

Deleted: , revealing strong perturbations of the energy budget within the Earth-Atmosphere system, which in turn affect atmospheric processes. Moreover,

859 The overarching goals of the present study are: (i) the assessment of the short-term direct radiative
860 effects (DREs) on the Earth-Atmosphere system's radiation budget, induced during intense
861 Mediterranean desert dust outbreaks, based on regional model simulations, (ii) the assessment of the
862 associated impacts on temperature and sensible/latent heat fluxes, (iii) the investigation of possible
863 feedbacks on dust AOD and dust emission and (iv) the assessment of the model's predictive skills, in
864 terms of reproducing temperature and radiation fields, when dust-radiation interactions are taken into
865 account in numerical simulations. To this aim, 20 intense and widespread desert dust outbreaks that
866 affected the broader area of the Mediterranean basin, over the period March 2000 – February 2013, have
867 been identified based on an objective and dynamic satellite algorithm, which utilizes daily multi-sensor
868 satellite retrievals (Section 2). It must be highlighted that through the consideration of a large dataset of
869 desert dust outbreaks is ensured the robustness of our findings, providing thus the opportunity to have a
870 clear view of dust outbreaks' impacts on radiation as well as about the associated impacts on
871 meteorological variables (e.g. temperature). For each dust outbreak, through short-term (84 h) numerical
872 simulations of the regional NMMB-MONARCH model (Section 3), the DREs are calculated at TOA,

Deleted: by

Formatted: Font: 12 pt, Not Italic

878 surface and into the atmosphere, both at grid point (geographical distributions) and regional scale level
879 (Section 5.2), for the SW, LW and NET (SW+LW) radiation. In addition, are examined the impacts of
880 the Mediterranean desert dust outbreaks on the sensible/latent heat fluxes (Section 5.3) and on the surface
881 temperature (Section 5.4) as well as the potential feedbacks on dust AOD and dust emissions (Section
882 5.5). The last part of the study (Sections 5.6 and 5.7) investigates the potential improvement of the
883 model's forecasting ability in terms of reproducing the temperature and radiation fields when dust-
884 radiation interactions are included in numerical simulations. A summary is made and conclusions are
885 drawn in Section 6.

886

887 2. Selection of desert dust outbreaks

888

889 In the present study, 20 intense and widespread desert dust outbreaks that affected the broader area of
890 the Mediterranean basin, over the period March 2000 – February 2013, are analyzed. The studied desert
891 dust outbreaks have been identified using an objective and dynamic satellite algorithm introduced in
892 Gkikas et al. (2013; flowchart in their Figure 2) and further improved in Gkikas et al. (2016). The
893 algorithm utilizes daily $1^\circ \times 1^\circ$ latitude-longitude resolution satellite retrievals, derived from MODerate
894 resolution Imaging Spectroradiometer (MODIS; Remer et al., 2005), Total Ozone Mapping Spectrometer
895 (TOMS; Torres et al., 1998) and Ozone Monitoring Instrument (OMI; Torres et al., 2007) observations.
896 The MODIS-Terra (Collection 051) aerosol optical depth at 550 nm (AOD_{550nm}), Ångström exponent (α),
897 fine fraction (FF) and effective radius (r_{eff} , available only over sea) products are used in the algorithm
898 along with EP-TOMS and OMI-Aura Aerosol Index (AI). Using these products, the algorithm takes into
899 account information regarding aerosols' load (AOD), size (FF , α and r_{eff}) and absorbing/scattering ability
900 (AI) which is necessary for the identification of dust.

901 Only a brief discussion of the algorithm operation is given here, whereas a detailed description is
902 provided in Gkikas et al. (2013). The satellite algorithm is applied to each individual $1^\circ \times 1^\circ$ grid cell of
903 the Mediterranean Satellite Domain (29° N - 47° N and 11° W - 39° E, MSD, red rectangle in Figure 1),
904 separately over land and sea surfaces, during the period March 2000 – February 2013. For each grid cell,
905 from the series (2000-2013) of daily AOD_{550nm} values, the mean ($Mean$) and the associated standard
906 deviation (Std) of AOD_{550nm} are calculated. Based on these two primary statistics, two threshold (or cut-
907 off) levels being equal to $Mean+2*Std$ and $Mean+4*Std$, are defined. By comparing each daily AOD
908 value to the two thresholds, the algorithm determines whether an aerosol episode (or event) occurs over
909 an $1^\circ \times 1^\circ$ grid cell (or pixel) in that day or not, and labels it as strong or extreme, depending on which
910 AOD threshold is exceeded (lower or higher). Thereby, the term “aerosol episode” refers to pixel-level

Deleted: developed

Deleted: u

Deleted: ar

Deleted:

915 episodic (extremely high loading) aerosol conditions and it is used with this meaning henceforth.
916 Subsequently, in order to characterize the identified pixel-level episodes as desert dust (DD) ones,
917 appropriate thresholds for α , FF , r_{eff} and AI are used, based on existing knowledge about relevant physical
918 properties (size and absorbing/scattering ability) of dust. According to the algorithm, a strong or extreme
919 pixel-level DD episode occurs if $\alpha \leq 0.7$, $FF \leq 0.4$, $r_{eff} > 0.6 \mu\text{m}$ and $AI > 1$ (conditions should be met
920 simultaneously).

921 Based on the satellite algorithm's outputs, for each day of the study period it is calculated the total
922 number of grid cells over which a strong or an extreme DD episode has taken place. Subsequently, from
923 the overall series of 4748 days over the study period, are kept only those in which at least 30 grid cells
924 with a DD episode (either strong or extreme) have been recorded. This criterion was first adopted by
925 Gkikas et al. (2015), who analyzed the atmospheric circulation evolution patterns favoring the occurrence
926 of dust outbreaks over the broader Mediterranean basin, in order to keep and study the most extensive
927 ones (in terms of the number of pixel-level DD episodes). In a next step, the days satisfying the defined
928 criterion (i.e. days where at least 30 pixel-level DD episodes have been occurred) are ranked based on
929 their regional MODIS-Terra AODs averaged over the "dust episodic" pixels within the geographical
930 limits of the MSD. If two or more consecutive days are satisfying the defined criteria, then the day with
931 the maximum number of DD episodes is selected. The final dataset consists of 20 intense Mediterranean
932 desert dust outbreaks listed in a chronological order in Table 1.

933 The majority of the selected desert dust outbreaks (55 % or 11 out of 20) took place in spring (March-
934 April-May) when massive dust loads originating in the Sahara Desert are transported towards the central
935 and eastern parts of the Mediterranean (Gkikas et al., 2013; Pey et al., 2013). Four widespread desert
936 dust outbreaks affected mainly the western sector of the MSD in summer (July, August), while five dust
937 outbreaks were recorded across the central and eastern parts of the basin in winter (January, February).
938 Among the selected cases, the number of pixel-level **total (strong plus extreme)** DD episodes in the MSD
939 varies from 30 (28 July 2005, western-central Mediterranean) to 85 (31 July 2001, western
940 Mediterranean). **Almost in all cases, the number of extreme DD episodes is higher than those for the
941 strong ones spanning from 20 (28 July 2005) to 51 (8 May 2002) and from 3 (24 February 2006) to 56
942 (31 July 2001), respectively. Likewise, the intensity (in terms of AOD at 550 nm) of total DD episodes**
943 ranges from 0.74 (31 July 2001) to 2.96 (2 March 2005), being in general higher in winter while
944 moderate-to-high intensities are recorded in spring. Based on the information in Table 1, the selected
945 study cases correspond to widespread and intense dust outbreaks that occurred in various parts of the

Deleted: (or grid cell)

Formatted: Font: 12 pt

Formatted: Font: 12 pt

Formatted: Font: 12 pt

Formatted: Font: 12 pt

Deleted: ,whereas

Deleted: ir

949 Mediterranean, and therefore they are representative and appropriate for further studying their radiative
950 effects.

951
952
953

954 3. Model description

955
956 In the present section, the main features of the meteorological driver (Section 3.1.1) and the dust
957 module (Section 3.1.2) used in the regional NMMB-MONARCH (Multiscale Online Nonhydrostatic
958 Atmosphere Chemistry) model, previously known as NMMB/BSC-Dust, are described. The version
959 (v1.0) of the NMMB-MONARCH model used here contributes to different model inter-comparisons like
960 the International Cooperative for Aerosol Prediction (ICAP) initiative and the Sand and Dust Storm
961 Warning Advisory and Assessment System (SDS-WAS), a project developed under the umbrella of the
962 World Meteorological Organization (WMO) with focus on improving capabilities of sand and dust storm
963 forecasts. For brevity reasons, only the main characteristics of the model are discussed here since a
964 thorough description is provided in Pérez et al. (2011, and references therein) as well as in recent
965 publications presenting its developments and applications in gas-phase chemistry (Badia et al., 2017),
966 volcanic ash dispersion (Marti et al., 2017) and data assimilation (Di Tomaso et al., 2017) studies. The
967 spectral variation of the GOCART dust optical properties, utilized as inputs to the radiation transfer
968 scheme, is presented in Section 3.2, whereas the model set up used in our experiments is given in Section
969 3.3.

970
971
972
973
974

971 3.1. The NMMB-MONARCH model

973 3.1.1. The NMMB atmospheric model

975 The Non-hydrostatic Multiscale Model NMMB (Janjic, 2004; Janjic and Black, 2007; Janjic et al.,
976 2011) is a unified atmospheric model developed at the National Centers for Environmental Prediction
977 (NCEP) (Janjic et al., 2001; Janjic, 2003). A powerful element of the model constitutes its non-
978 hydrostatic dynamical core, activated depending on the resolution, providing the capability to be used
979 for applications spanning at a wide range of temporal (from short- to long-term) and spatial (from
980 regional to global) scales. An additional dynamic feature of the NMMB is the consideration of various
981 parameterization schemes which can be incorporated into the numerical simulations. In our experiments,
982 the parameterization schemes of Betts-Miller-Janjic (Betts, 1986; Betts and Miller, 1986; Janjic, 1994,
983 2000), Ferrier (Ferrier et al., 2002), Mellor-Yamada-Janjic (Janjic et al., 2001) and Monin-Obukhov

Deleted: The occurrence of intense desert dust outbreaks during the first half of the year is favored either by the predominance of intense low pressure systems across the Mediterranean basin (Varga et al., 2014; Gkikas et al., 2015) or by their eastwards shift (Saharan depressions) across the northern coasts of Africa (Alpert and Ziv, 1989). In both seasons, dust transport from the northern Africa deserts towards the Mediterranean is induced by the prevailing southerly or southwesterly airflow (Barkan et al., 2005; Meloni et al., 2008). Some of the identified desert dust outbreaks here, have been also analyzed in previous studies related to particulate matter levels (Kanakidou et al., 2010), chemical speciation (Theodosi et al., 2010), dust layers' vertical structure (Amiridis et al., 2009; DeSouza-Machado et al., 2010), dust radiative effects (Di Sarra et al., 2011), dust modelling (Carnevale et al., 2012) and prevailing synoptic conditions favoring the occurrence of dust events (Nastos, 2012).

Deleted: simulations

1003 (Monin and Obukhov, 1954) have been utilized for the convection, cloud microphysics, turbulence and
1004 surface layer, respectively, as well as the NOAH land model (Ek et al., 2003). Moreover, only the
1005 greenhouse gases are taken into account and not the emitted short lived atmospheric gases. The model's
1006 dynamic equations, in the horizontal plane, are solved on the Arakawa B grid (Arakawa and Lamb, 1977)
1007 while in vertical the general hybrid pressure-sigma coordinate (Simmons and Burridge, 1981) is utilized.
1008 For regional simulations, a rotated longitude-latitude coordinated system is used (the Equator is running
1009 through the middle of the integration domain) enabling therefore more uniform grid distances.

1010 3.1.2. The Dust component

1011
1012
1013 The main components of the desert dust life cycle, regarding mineral particles' production in the
1014 source areas, transport and removal from atmosphere, are considered in the dust component of the
1015 MONARCH model, which is embedded into the NMMB model. The size intervals as well as the effective
1016 radii for each one of the 8 dust bins, representing clay-originated sub-micron (bins 1-4) and silt-originated
1017 coarse (bins 5-8) particles, that are considered in the dust module were adopted from Pérez et al. (2006).
1018 The mass of each bin is calculated at each time step, grid point and layer, while the median mass diameter
1019 and the geometric standard deviation of the sub-bin distribution are fixed to 2.524 μm and 2.0 μm ,
1020 respectively. In the existing version of the NMMB-MONARCH model, dust aerosols are externally
1021 mixed and hydrophobic. All the required parameters regulating dust emission and mobilization namely
1022 the: (i) surface wind speed, (ii) turbulence, (iii) land use type, (iv) vegetation cover, (v) erodibility, (vi)
1023 surface roughness, (vii) soil texture and (viii) soil moisture, are considered in the dust emission scheme
1024 (Pérez et al., 2011). The vertical dust flux for each dust size bin is proportional to the horizontal sand
1025 flux while several parameters are tuned to match observations that are mainly available far away from
1026 the sources. Coarse dust aerosols are removed efficiently from the atmosphere through sedimentation,
1027 which is solved implicitly in each model layer. For the description of dust aerosols' wet removal, a
1028 mechanism which is more effective for fine mineral particles, parameterizations representing in- and
1029 below-cloud scavenging are included in the NMMB-MONARCH in which the grid-scale cloud
1030 microphysical scheme of Ferrier and the convective adjustment scheme of Betts-Miller-Janjic are utilized
1031 (Pérez et al., 2011). The ability of the NMMB-MONARCH model to reproduce accurately the dust
1032 aerosol fields has been confirmed through evaluation studies, relied on global and regional annual
1033 simulations (Pérez et al., 2011), as well as by utilizing measurements from experimental campaigns as
1034 reference data (Haustein et al., 2012). Moreover, the reliability of the model in terms of reproducing the
1035 Saharan dust patterns over Cape Verde as well as to simulate dust vertical profiles has been confirmed

Deleted: , both at regional and global

Deleted: scale

Deleted: ve

1039 through the analyses made by Gama et al. (2015) and Biniotoglou et al. (2015), respectively. In addition,
1040 the predictive skills of the NMMB-MONARCH model, in comparison with other regional models, have
1041 been assessed for a specific dust outbreak (Huneus et al., 2016) that affected the western parts of the
1042 Mediterranean and Europe. Finally, in the framework of the SDS-WAS ([https://sds-](https://sds-was.aemet.es/forecast-products/forecast-evaluation)
1043 [was.aemet.es/forecast-products/forecast-evaluation](https://sds-was.aemet.es/forecast-products/forecast-evaluation)), the evaluation of the simulated dust fields (over
1044 Sahara, Middle East and Mediterranean) produced by 12 models, versus ground-based (AERONET) and
1045 spaceborne (MODIS) retrievals, reveals that the NMMB-MONARCH is ranked at the highest positions.

Deleted: Finally

Formatted: English (United States)

1047 3.2. *Radiative transfer model and dust optical properties*

Deleted: Radiation transfer scheme

1048 For the description of dust aerosols interaction both with the SW, and LW radiation, the RRTMG
1049 (Rapid Radiative Transfer Model for Global Circulation Models, Iacono et al., 2008) radiative transfer
1050 model is coupled with the dust module. RRTMG consists a modified version of the RRTM which is a
1051 broadband radiative transfer model that includes the molecular absorption of the SW (by water vapor,
1052 carbon dioxide, ozone, methane and oxygen) and LW (by water vapor, carbon dioxide, ozone, methane,
1053 nitrous oxide, oxygen, nitrogen and halocarbons) radiation. Even though the basic physics and absorption
1054 coefficients utilized in RRTM (Mlawer et al., 1997) remain unchanged in RRTMG, several updates
1055 regarding computational efficiency and representation of subgrid-scale cloud variability have been
1056 implemented (Iacono et al., 2008). Through these adjustments, it has been improved the efficiency of the
1057 RRTMG in global circulation model (GCM) applications with a minimal loss of accuracy (Iacono et al.,
1058 2008). In the RRTMG, the total number of quadrature points (g points) used to calculate radiances has
1059 been reduced from 224 to 112 and from 256 to 140 for the shortwave and longwave spectrum,
1060 respectively. In addition, for the short wavelengths, the discrete ordinates algorithm DISORT (Stammes
1061 et al., 1998) has been replaced by a two-stream radiation transfer solver (Oreopoulos and Baker, 1999).
1062 All the updates applied in the RRTMG radiation transfer code are listed in the Atmospheric and
1063 Environmental Research (AER) radiative transfer web site (<http://rtweb.aer.com/>). Based on evaluation
1064 studies, the comparison of the RRTMG clear-sky SW and LW fluxes versus RRTM_SW and LBLRTM,
1065 respectively, has revealed that its accuracy at short wavelengths is within 3 Wm^{-2} whereas at long
1066 wavelengths is 1.5 Wm^{-2} . As inputs to the radiation transfer scheme, the aerosol optical depth (AOD,
1067 measure of the aerosol load), the single scattering albedo (SSA, expresses the fraction of scattering to
1068 total extinction) and the asymmetry parameter (ASYM, measures the degree of symmetry of the phase
1069 function between the forward and backward hemispheres) are required. In the present version (v1.0) of

Deleted: shortwave (

Deleted:)

Deleted: longwave (LW)

Formatted: English (United States)

Deleted: Mlawer et al., 1997;

Deleted: on

Deleted: scheme

Deleted: considered

Deleted: quadratic

Deleted: <http://www.rtweb.aer.com/>

Formatted: Default Paragraph Font, Font: (Default)
+Body (Calibri), 11 pt, Italic, English (United States)

Formatted: Default Paragraph Font, Font: (Default)
+Body (Calibri), Not Italic

Deleted: percentage

Deleted: expresses the angular distribution of the scattered radiation

1085 the model, the calculation of dust optical properties is made based on the formulas presented in Pérez et
1086 al. (2006), by using the mass concentration simulated by the NMMB-MONARCH model, the single-
1087 particle optical properties derived by the GOCART model (Chin et al., 2002), and the refractive indices
1088 from the Global Aerosol Data Set (GADS) (Koepke et al., 1997) which have been modified using Sinyuk
1089 et al. (2003), as described in Pérez et al. (2011). The spectral variation of the single-particle dust optical
1090 properties for each bin, namely the mass extinction coefficient, the single scattering albedo and the
1091 asymmetry parameter are shown in Figures 2-i, 2-ii and 2-iii, respectively. Their calculation for each dust
1092 size bin and at each spectral band is made based on the Mie code (Mishchenko et al., 2002) assuming
1093 homogeneous and spherical dust particles. For the other types of tropospheric aerosols (sulfate, organic
1094 carbon, black carbon, and sea salt), the GOCART monthly climatological AOD, SSA and ASYM values
1095 for the year 2000, are utilized.

1096 3.3. Model set-up configuration

1097 In our experiments, the simulation domain (NMMB-MONARCH Simulation Domain, NSD, outer
1098 domain in Figure 1) covers the Sahara (dust sources areas), the Mediterranean (mid-range dust transport
1099 areas) as well as most of the European continent (long-range dust transport areas). The horizontal
1100 resolution is equal to 0.25° x 0.25° degrees and 40 sigma-hybrid pressure levels up to 50 hPa are used in
1101 vertical. The atmospheric model's fundamental time step is set to 25 seconds. The simulations have been
1102 made for each one of the 20 identified Mediterranean desert dust outbreaks (see Section 2) considering
1103 a spin-up and a forecast period, using 1° x 1° NCEP final analyses (FNL) as initial and 6-h boundary
1104 conditions. More specifically, for each case, a hindcast period of 84 hours starts at 00 UTC of the day
1105 (see the second column in Table 1) when the desert dust outbreak has been identified according to the
1106 defined criteria (explained in Section 2). In order to ensure a more “realistic” initial state of the
1107 atmosphere, a 10-day spin-up before the initialization of the forecast period is simulated, where the
1108 model's meteorology is reinitialized every 24 hours. During the forecast periods, for the computation of
1109 the aerosol radiative effects, two configurations of the model were run. In the first one (RADON), all
1110 aerosol types interact with radiation while in the second one the corresponding interactions are
1111 deactivated (RADOFF). It must be clarified that in the RADON experiment, the perturbation of the
1112 radiation fields is mainly caused by dust aerosols, which are dynamically calculated, while the
1113 contribution of the other aerosol species depends on climatological optical properties derived from
1114 GOCART. However, since the selected cases refer to desert dust outbreaks, the term “dust-radiation
1115 interactions” instead of “aerosol-radiation interactions” is used throughout the manuscript.

Deleted: and

Formatted: Font: (Default) Times New Roman, 12 pt, No underline, Font color: Auto

Deleted: it has been

Deleted: For

Deleted: dust

Deleted: s

Deleted: the short- and longwave

1124

1125

1126

1127

1128

1129

1130

1131

1132

1133

1134

1135

1136

1137

1138

1139

1140

1141

1142

1143

1144

1145

1146

1147

1148

1149

1150

1151

1152

1153

1154

1155

1156

1157

4. Calculation of the dust direct radiative effects

The direct radiative effects (DREs), expressed in Wm^{-2} , are computed at the top of the atmosphere (TOA), into the atmosphere (ATM), and at the surface, for the downwelling (SURF) and the absorbed (NETSURF) radiation, for the shortwave (SW), longwave (LW) and NET (SW+LW) radiation. The calculations are made according to the following formulas:

$$DRE_{TOA} = F_{TOA,RADOFF}^{\uparrow} - F_{TOA,RADON}^{\uparrow} \text{ (Eq. 1)}$$

$$DRE_{SURF} = F_{SURF,RADON}^{\downarrow} - F_{SURF,RADOFF}^{\downarrow} \text{ (Eq. 2)}$$

$$DRE_{NETSURF} = (F_{SURF,RADON}^{\downarrow} - F_{SURF,RADON}^{\uparrow}) - (F_{SURF,RADOFF}^{\downarrow} - F_{SURF,RADOFF}^{\uparrow}) = F_{NETSURF,RADON} - F_{NETSURF,RADOFF} \text{ (Eq. 3)}$$

$$DRE_{ATM} = DRE_{TOA} - DRE_{NETSURF} \text{ (Eq. 4)}$$

At TOA (Eq.1), DREs are calculated through the subtraction of the RADON (dust-radiation interaction is activated) from the RADOFF (dust-radiation interaction is deactivated) outputs of the upward (\uparrow) radiative fluxes (F) and express the loss (cooling effect or planetary cooling) or the gain (warming effect or planetary warming) of energy within the Earth-Atmosphere system when are negative and positive, respectively. At the surface, DREs are computed for both the downwelling (\downarrow) (SURF, Eq. 2) and the net (downward minus upward) radiation (NETSURF, Eq. 3). Both DREs indicate a dust-induced surface cooling or warming when they get negative or positive values, respectively. Finally, on energy within the Earth-Atmosphere system, the DRE_{ATM} is calculated by subtracting the $DRE_{NETSURF}$ from the DRE_{TOA} values (Eq. 4) and quantifies the impact (warming or cooling) of dust outbreaks on the atmospheric radiation budget. The DREs are based on the subtraction of two independent model runs. Therefore, our results represent the radiative anomalies induced by dust aerosols including both the direct effect and the rapid response of atmospheric constituents such as humidity and clouds (semi-direct effects).

5. Results

5.1. Comparison of model and satellite AODs

Deleted: ¶

Deleted: fast

Deleted: DREs are analyzed both at grid point (geographical distributions) and at regional scale levels and the obtained results will be discussed in Section 5.2.

1163 Before dealing with the DREs, the ability of the model to reproduce satisfactorily the dust AOD fields
1164 is assessed using MODIS-Terra AOD_{550nm} retrievals as reference data. The results of the intercomparison
1165 between the daily satellite AODs (left column in Fig. 3) and the modelled (right column in Fig. 3) AODs
1166 at 12 UTC (instantaneous fields) are presented here for three of the 20 identified desert dust outbreaks
1167 (see Section 2), which took place on 2nd March 2005 (upper row in Fig. 3), 19th May 2008 (middle row
1168 in Fig. 3) and 2nd August 2012 (bottom row in Fig. 3) and affected the eastern, central and western parts
1169 of the Mediterranean basin, respectively. The corresponding maps for the remaining 17 cases are
1170 illustrated in Figure S1. Note, that the evaluation of the model outputs versus the satellite measurements
1171 is restricted within the geographical limits of the MSD (red rectangle in Fig. 1), since the satellite
1172 algorithm used for identification of the desert dust outbreaks is applied only to this region (see Section
1173 2). Moreover, in order to eliminate the spatial inconsistencies between the two products, we have
1174 regridded the model outputs from their raw spatial resolution (0.25° x 0.25°) to 1° x 1° matching them
1175 with the satellite retrievals.

Deleted: dust

1177 According to the MODIS-Terra observations on 2nd March 2005, a dust plume extends from the Gulf
1178 of Sidra to the southern parts of Greece, with AODs up to 5 (Fig. 3 i-a). As shown in Fig. 3 i-b, the model
1179 on this day simulates high dust AOD_{550nm} values (1-3.25) along a dust plume, extending from Algeria to
1180 the Black Sea, which affects the eastern parts of the Mediterranean Sea. Through the intercomparison of
1181 satellite and model AODs, it is revealed that the desert dust outbreak is slightly shifted eastwards while
1182 the maximum dust AODs are lower than those retrieved by the satellite sensor. The second desert dust
1183 outbreak occurred on 19th May 2008 and affected the central sector of the MSD. According to MODIS
1184 (Fig. 3 ii-a), the intensity of dust loads is maximized (up to 4) in the central parts of the Mediterranean
1185 Sea (southeastern of Sicily). This is also reproduced by the model, although somewhat higher AODs are
1186 found over the central and southern parts of Italy (Fig. 3 ii-b). In spite of this, however, there is a clearly
1187 good model performance in reproducing the dust event that hit the central Mediterranean. An ever better
1188 agreement between the model and satellite AODs, in terms of spatial variability and intensity of dust
1189 loads, is found for the desert dust outbreak of August 2nd 2012, that affected the westernmost parts of the
1190 Mediterranean, with highest AODs (up to 2-2.5) from the Alboran Sea down to the coastal areas of
1191 Morocco (Figs. 3 iii-a,b).

Deleted: is able to reproduce satisfactorily the spatial patterns of AOD on this day, with high d

Deleted: 4

Deleted: ing

Deleted: .

Deleted: ing

Moved (insertion) [1]

1192 Apart from a qualitative comparison between MODIS and NMMB-MONARCH, the performance of
1193 the model has been assessed also quantitatively. More specifically, for each desert dust outbreak the
1194 spatial correlation coefficient (R) values as well as the absolute biases (defined as NMMB-MODIS) have
1195 been calculated considering only the grid cells where a DD episode (either strong or extreme) has been

1203 identified by the satellite algorithm. In Figure S2, are presented the computed regional R (Fig. S2-ii) and
1204 bias (Fig. S2-iii) scores while the stacked bars (Fig. S2-i) illustrate the number of strong, extreme and
1205 total DD episodes (available also in Table 1). Among the studied cases, it is revealed a strong variation
1206 of R values (Figure S2-ii) reflecting the diversity of the model's capability in terms of capturing the
1207 spatial patterns of the desert dust outbreaks. These drawbacks result mainly from displacements of the
1208 simulated dust patterns with respect to the observed ones. The best performance is found on 22 Feb 2004
1209 (R=0.82) in contrast to 23 Jan 2009 where the correlation coefficient is zero. In 7 out of 20 cases, the R
1210 values are higher than 0.5 while in 7 cases vary between 0.2 and 0.4 indicating a weak-to-moderate
1211 performance of the model. In the remaining 6 dust events, the spatial agreement between MODIS and
1212 NMMB is characterized poor (R<0.2). As it concerns the bias, in absolute terms, in all the events negative
1213 values are recorded ranging from -2.3 (24 Feb 2006) to -0.17 (19 May 2008). This finding shows that the
1214 model underestimates consistently the intensity of the desert dust outbreaks which have been analyzed
1215 in the present study.

1216 According to the evaluation analysis, the model's ability in terms of reproducing satisfactorily the
1217 dust fields varies strongly case-by-case while the simulated intensity of the desert dust outbreaks is lower
1218 with respect to the satellite retrievals. Therefore, both facts can raise questions regarding the accuracy of
1219 the computed DREs in some cases since the perturbations of the radiation fields are determined to a large
1220 extent by AOD (e.g. Hatzianastassiou et al., 2004; Pérez et al., 2006; Papadimas et al., 2012).
1221 Nevertheless, several factors affect/determine the level of agreement between observed and simulated
1222 AODs providing a reasonable explanation about the discrepancies found between MODIS and NMMB-
1223 MONARCH. The most important is the temporal inconsistency between the two products. More
1224 specifically, the satellite retrievals correspond to daily averages whereas the model products are
1225 representative for a specific forecast time (instantaneous fields). Considering the high variability of
1226 aerosols' loads, particularly under episodic conditions, this temporal discrepancy imposes a limitation
1227 when a quantitative comparison between MODIS and NMMB is attempted. This can explain the
1228 observed differences found either on the intensity or on the spatial patterns of the desert dust events.
1229 Also, it must be considered that artifacts of the satellite retrievals (e.g. clouds contamination,
1230 representativeness/homogeneity within the 1° x 1° grid cell) may lead to higher AODs as it has been
1231 shown in relevant evaluation studies (e.g. Gkikas et al., 2016). Moreover, due to the inability of the
1232 MODIS Dark Target (DT) algorithm to retrieve aerosol optical properties over desert areas as well as
1233 under cloudy conditions, in a significant part of the study region there are not available satellite

1234 observations (white areas in Figs. 3 i-a, ii-a and iii-a) restricting thus their comparison with the model
1235 outputs which provide full spatial coverage.

1237 5.2. Direct radiative effects (DREs)

1239 5.2.1. Geographical distributions

1240
1241 For each desert dust outbreak, the TOA, ATM, SURF and NETSURF DREs have been computed for
1242 the SW, LW and NET radiation, according to the formulas presented in Section 4. Just as an example, in
1243 Figure 4 are illustrated the geographical patterns of the instantaneous NET (SW+LW) DRE_{TOA} (second
1244 column), DRE_{ATM} (third column), DRE_{SURF} (fourth column) and $DRE_{NETSURF}$ (fifth column) values, at
1245 12 h (first row), 24 h (second row), 36 h (third row) and 48 h (fourth row) after the initialization of the
1246 model forecast on 2nd August 2012 at 00 UTC, along with the simulated patterns of dust AOD at 550 nm
1247 on the same day and time (first column). For brevity reasons only the results for the allwave (NET) are
1248 given, while the SW and LW DREs and their contribution to NET DREs are discussed in the regional
1249 analysis (next sub-section). The corresponding patterns for each desert dust outbreak are given in Figures
1250 S3 – S21 in the supplementary material. Moreover, for each desert dust outbreak, the minimum and
1251 maximum clear-sky NET DREs at grid point level, during the simulation period, are presented in Table
1252 S1.

1253 Based on the model outputs, at 12 h, an arc shaped dust plume affected the western parts of the Sahara,
1254 the Canary Islands, the maritime areas off the Moroccan coasts, the southern parts of the Iberian
1255 Peninsula and the western Mediterranean Sea (Fig. 4). During the forecast period, the spatial features of
1256 the desert dust outbreak do not reveal a remarkable variability, with maximum AODs (up to 3) across
1257 Mali, Mauritania, Western Sahara and in the Canary Islands. At a first glance, it is evident that the DRE
1258 patterns are driven by those of the desert dust outbreaks whereas small scale isolated features of
1259 extremely high/low DREs mainly result from slight “shifts” of clouds between the two independent
1260 model runs. Moreover, it is apparent that both the sign and the magnitude of DREs vary among TOA,
1261 surface and atmosphere as well as with time (day or night). During daytime (12 h and 36 h) the DREs
1262 are driven by their SW components which significantly exceed the LW ones. Through absorption and
1263 scattering of solar radiation by mineral particles, the downwelling radiation at the ground (SURF) is
1264 reduced by up to 308 Wm^{-2} , indicating a strong surface cooling (bluish colors) in areas where the dust
1265 AOD is maximized like Mauritania or south Algeria. During nighttime (24 and 48 h), the sign of the
1266 DRE_{SURF} values is reversed and their magnitude decreases compared to that at 12 and 36 h. This is
1267 because during the night the DRE_{SURF} values are identical to the LW DRE ones, which are positive,

Moved up [1]: The second desert dust outbreak occurred on 19th May 2008 and affected the central sector of the MSD. According to MODIS (Fig. 3 ii-a), the intensity of dust loads is maximized (up to 4) in the central parts of the Mediterranean Sea (southeastern of Sicily). This is also reproduced by the model, although somewhat higher AODs are found over the central and southern parts of Italy (Fig. 3 ii-b). In spite of this, however, there is a clearly good model performance in reproducing the dust event that hit the central Mediterranean. An ever better agreement between the model and satellite AODs, in terms of spatial variability and intensity of dust loads, is found for the desert dust outbreak of August 2nd 2012, that affected the westernmost parts of the Mediterranean, with highest AODs (up to 2-2.5) from the Alboran Sea down to the coastal areas of Morocco (Figs. 3 iii-a,b).

Deleted: There is a good agreement between the model and the satellite over areas where the satellite measurements are available, highlighting the ability of the model to capture satisfactorily the spatial features of dust loads. Nevertheless, several factors affect the level of agreement between model outputs and satellite observations and for this reason only a qualitative intercomparison is attempted. The most important of them are related to the differences regarding the spatiotemporal resolution and the aerosol optical depth product. MODIS provides daily total AODs at $1^\circ \times 1^\circ$ spatial resolution in contrast to the NMMB-MONARCH model which produces instantaneous dust AODs at $0.25^\circ \times 0.25^\circ$ spatial resolution. Moreover, due to the inability of the MODIS Dark Target (DT) algorithm to retrieve aerosol optical properties over desert areas as well as under cloudy conditions, in a significant part of the study region there are not available satellite observations (white areas in Figs. 3 i-a, ii-a and iii-a) restricting thus their comparison with the model outputs which provide full spatial coverage.¶

Deleted: The model’s ability to reproduce correctly the spatial patterns and values of dust AODs is crucial for a successful computation of the dust DREs, since DREs are determined to a large extent by AOD (e.g. Hatzianastassiou et al., 2004; Pérez et al., 2006; Papadimas et al., 2012).

Deleted: According to the simulated atmospheric circulation patterns (results not shown here), strong near surface winds prevail across a convergence zone (in western Sahara) developed between a low pressure system with its center in Mauritania-Mali and the Azores subtropical anticyclone. At 700 hPa (~ 3000 meters), the uplifted mineral particles are transported towards the western Mediterranean due to the prevailing strong southwesterly winds (~30 knots) off the Moroccan coasts. Similar synoptic conditions have been presented in Cluster 2 in Gkikas et al., (2015), who studied the atmospheric circulation evolution related to the occurrence of desert dust episodes over the Mediterranean.¶

Deleted: It must be mentioned that the limits of the DREs’ colorbars in Figure 4 are set equal to -300 and 300 Wm^{-2} in order to facilitate the intercomparison among the different levels within the Earth-Atmosphere system, the comparison between day and night DREs and the visualization of our results.

Deleted: h

Deleted: h

1328 implying extra downwelling LW radiation at the surface, by up to 58 Wm^{-2} , emitted by the overlying
1329 dust. This effect, leading to night surface warming, is more visible over specific parts of Sahara that host
1330 high dust loads, e.g. in its western parts. The geographical patterns of $\text{DRE}_{\text{NETSURF}}$ are very similar to
1331 those of DRE_{SURF} , as expected, since they only differ by the net upward radiation at the surface, which
1332 in turn is determined by the surface albedo (for the SW radiation) and temperature (for the LW radiation).
1333 Based on our results, the negative (surface cooling) and positive (surface warming) $\text{DRE}_{\text{NETSURF}}$ values
1334 can reach down to -290 Wm^{-2} (eastern Atlantic Ocean) and up to 42 Wm^{-2} (western Sahara) during day
1335 and night, respectively. Among our studied cases (see Table S1) the instantaneous NET DRE_{SURF} and
1336 $\text{DRE}_{\text{NETSURF}}$ values at noon can be as large as -589 Wm^{-2} and -337 Wm^{-2} , respectively, in agreement with
1337 relevant results reported in previous studies dealing with the radiative impacts of dust intrusions in the
1338 Mediterranean (Pérez et al, 2006; Remy et al., 2015), in west Africa (Heinold et al., 2008; Mallet et al.,
1339 2009) and in Asia (Wang et al., 2009; Singh and Beegum et al., 2013).

1340 The occurrence of desert dust outbreaks results in a strong perturbation of the atmospheric radiation
1341 budget, attributed to the interaction of dust aerosols with the SW and LW radiation. More specifically,
1342 during daytime (i.e. 12 and 36 h), mineral particles absorb radiation at short wavelengths warming thus
1343 the atmosphere as indicated by the positive instantaneous NET DRE_{ATM} values in Figure 4 (third
1344 column), reaching up to 189 Wm^{-2} over the dust affected areas. Our calculated noon atmospheric DREs
1345 (Table S1) are comparable to those reported by Heinold et al. (2008; 2011) and significantly lower
1346 compared to those in Pérez et al. (2006), who found DRE_{ATM} values higher than 500 Wm^{-2} in land areas
1347 with dust $\text{AOD} > 3$ during a desert outbreak that affected the Mediterranean on 12th April 2002. We note
1348 that Pérez et al. (2006) used complex refractive indices taken from the Global Aerosol Data Set (GADS)
1349 that have been shown to be excessively absorbing, which may partly explain their high DRE_{ATM} values.
1350 During night, negative DRE_{ATM} values (down to -45 Wm^{-2} in Algeria and Mali) are computed in the dust
1351 affected areas indicating an atmospheric cooling because of the emission of LW radiation by mineral
1352 particles (Wang et al., 2013b).

1353 The sign and magnitude of DRE_{TOA} (Eq. 4) are regulated by $\text{DRE}_{\text{NETSURF}}$ and DRE_{ATM} . At noon and
1354 above cloud-free areas, there is a distinct change of DRE_{TOA} sign over oceanic and desert areas affected
1355 by dust loads (note for example the red colors over the dusty western Sahara Desert regions, e.g.
1356 Mauritania, against blue colors off the African coasts). This change of the DRE_{TOA} sign is due to the
1357 difference in surface albedo of the two types of surface (water and desert), in combination with dust high
1358 AODs and low-to-moderate single scattering albedo enhancing solar absorption by dust above highly
1359 multiple reflecting surfaces. Such a reverse of DRE_{TOA} sign has been also reported in previous studies

Deleted: DRE for NETSURF expresses the amount of radiation absorbed at the ground and is calculated through the subtraction of the upward from the downward surface radiative fluxes (see Eq. 3). Therefore, the differences between DRE_{SURF} and $\text{DRE}_{\text{NETSURF}}$ are regulated by the upward component, which in turn is determined by the surface albedo and temperature for the SW and LW radiation, respectively. For this reason, the negative differences (i.e. $\text{DRE}_{\text{SURF}} - \text{DRE}_{\text{NETSURF}}$) at noon are maximized over highly reflective areas, while the positive ones at night are observed in land areas where the surface cooling during sunlight hours is maximized (i.e. reduction of the surface temperature during day leads to reduction of the emitted longwave radiation during night).

Deleted: h

Deleted: .

Deleted: In order to highlight the strong instantaneous atmospheric warming induced by the desert dust outbreaks, we have compared our results with similar ones obtained by previous studies that have been relied on long-term model simulations. Zhao et al., (2011) found that the average net atmospheric warming across the Sahara Desert, over the period April-September 2006, can be higher than 30 Wm^{-2} based on regional simulations of the WRF-Chem model. According to global simulations conducted at climatic scales (e.g. Woodage and Woodward, 2014), dust aerosols can increase the absorbed radiation into the atmosphere (warming effect) by up to 20 Wm^{-2} across the Northern Africa. Radiative transfer computations of SW DRE_{ATM} for the 2000-2007 period by Papadimas et al. (2012) reported local values of a few decades up to about 100 Wm^{-2} in spring and summer above the Sahara Desert.

1392 (e.g. Santese et al., 2010; Nabat et al., 2012; Papadimas et al., 2012). Over highly reflective surfaces (i.e.
1393 deserts), the atmospheric warming is enhanced since dust aerosols absorb not only the incoming solar
1394 radiation but also the radiation reflected by the surface. At the same time, the amount of the absorbed
1395 radiation at the ground is reduced by the attenuation of the SW radiation and by the increase of the back
1396 reflected radiation at the surface. The combination of these processes results in a predominance of the
1397 atmospheric warming over surface cooling and subsequently to positive DRE_{TOA} values (planetary
1398 warming), which can be as large as 85 Wm^{-2} according to our simulations (Table S1). On the contrary,
1399 when dust aerosols are suspended over dark surfaces (i.e. maritime areas), the condition is reversed and
1400 negative DRE_{TOA} values down to -184 Wm^{-2} (Table S1) are calculated, revealing thus a strong planetary
1401 cooling. Nevertheless, the positive DRE_{TOA} values exceeding 300 Wm^{-2} , which are recorded in maritime
1402 areas off the western African coasts, are associated with the existence of absorbing dust aerosols
1403 superimposed over low- and mid-level clouds. During night, the atmospheric cooling offsets the surface
1404 warming, both induced by the desert dust outbreaks, and for this reason the DRE_{TOA} values are almost
1405 negligible (do not exceed 10 Wm^{-2} in absolute terms over cloud free areas) indicating an almost null dust
1406 direct radiative effect. Our model computed dust induced planetary warming above western Africa is
1407 comparable to similar results reported in previous studies focusing on the same or similar desert areas
1408 (e.g. Mallet et al., 2009; Pérez et al., 2006; Wang et al., 2010; Nabat et al., 2012; Kalenderski and
1409 Stenchikov, 2016).

1411 5.2.2. Regional mean results

1412 In order to show more clearly temporal patterns, DREs were also averaged over the NSD (outer
1413 NMMB Simulation Domain in Figure 1), SDD (Sahara Desert Domain, green rectangle in Figure 1) and
1414 MSD (Mediterranean Satellite Domain, red rectangle in Figure 1) domains, for each desert dust outbreak,
1415 separately for the NET, SW and LW radiation. Then, in a further step, DRE values have been averaged
1416 over the 20 dust outbreaks every three hours during the forecast period (84 hours). Thus, the time series
1417 of regional mean and associated standard deviation (shaded areas) all-sky TOA (black curve), SURF
1418 (purple curve), NETSURF (blue curve) and ATM (red curve) DREs are depicted in Figure 5.

1420 The SW DREs (upper row in Fig. 5) are positive in the atmosphere (ATM, warming effect) and
1421 negative at the surface (SURF and NETSURF, cooling effect) throughout the entire forecast period,
1422 revealing a distinct diurnal cycle with marked maximum values around noon over all three domains. A
1423 careful look, however, reveals some differences between the sub-regions. Thus, in NSD (first column)
1424 and SDD (second column) the maximum DRE_{ATM} values increase slightly with time from 22.3 to 22.7

Deleted: and is characterized by a clear contrast between red and blue colors (planetary warming and cooling, respectively) over adjacent continental and oceanic areas

Deleted: , although differences also exist with regards to the magnitude or spatial DRE_{TOA} patterns. These differences are attributed to the different magnitude and spatial patterns of AOD values (dust loads) associated with the different studied dust outbreaks, and also to differences in dust microphysical and optical properties (Colarco et al., 2014)

Deleted: Only cloud free grid points, in both model configurations (RADON and RADOFF), with RADON dust AOD_{550nm} values higher/equal than 0.05 have been considered in this analysis.

Deleted: clear

Deleted: clear-sky

Deleted: 30

Deleted: 35

1442 Wm^{-2} and from 29.1 to 31.6 Wm^{-2} , respectively, while in contrast they decrease in MSD (third column)
 1443 from 21 to 18.5 Wm^{-2} . Respectively, the negative DRE_{SURF} values (surface cooling) reach down to -33.1
 1444 Wm^{-2} in the NSD and 45.3 Wm^{-2} in the SDD, while in the Mediterranean area reach down to -34.8 Wm^{-2} .
 1445 In addition, the magnitude of DRE_{SURF} and $\text{DRE}_{\text{NETSURF}}$ values in NSD and MSD slightly decrease
 1446 while an increasing trend (in absolute terms) is recorded in the SDD. The opposite tendencies found for
 1447 both sub-regions (i.e., SDD and MSD) for the atmospheric and surface DREs are attributed to the increase
 1448 and decrease of dust AOD over the Sahara (Figure S22-ii) and the Mediterranean (Figure S22-i),
 1449 respectively. As it concerns the SW $\text{DRE}_{\text{NETSURF}}$ values, their temporal variation is identical to the
 1450 corresponding ones for DRE_{SURF} ; however, the former ones are lower by up to 14.6 Wm^{-2} , in absolute
 1451 terms. The most noticeable difference between the two sub-domains (i.e. SDD and MSD) is encountered
 1452 for the DRE_{TOA} at noon. Over bright desert surfaces, dust outbreaks warm the Earth-Atmosphere system
 1453 as indicated by the positive DRE_{TOA} values (up to 3.2 Wm^{-2}) while over the darker (mostly covered by
 1454 sea) surfaces of the Mediterranean, the mineral particles induce a planetary cooling with DRE_{TOA} values
 1455 ranging from -12 to -4 Wm^{-2} . In both subdomains, the strongest planetary cooling is found at early
 1456 morning and afternoon hours with negative SW DRE_{TOA} values down to -11.9 Wm^{-2} and -11.6 Wm^{-2}
 1457 over Sahara and Mediterranean, respectively. On the contrary, DRE_{TOA} values decrease towards noon,
 1458 due to increasing solar absorption and decreasing scattering by dust under smaller solar zenith angles.
 1459 Finally, the regional SW DREs have been analyzed also separately over land and sea surfaces for the
 1460 three subdomains (results not shown here) revealing that the computed DREs are mainly driven by the
 1461 corresponding perturbations simulated over continental regions.

1462 The regional all-sky DREs have been also computed for the LW spectrum (middle row in Figure 5)
 1463 revealing reverse effects of lower magnitude (in absolute terms) with respect to the corresponding ones
 1464 found at short wavelengths. Due to the emission of LW radiation by the mineral particles, desert dust
 1465 outbreaks induce an atmospheric cooling (negative LW DRE_{ATM} values) and increase the amount of the
 1466 downward LW radiation at the surface (positive LW DRE_{SURF} values). Both DRE_{ATM} and DRE_{SURF} levels
 1467 do not reveal remarkable temporal variation ranging from -4.8 to -2.2 Wm^{-2} and from 1.4 to 3.7 Wm^{-2} ,
 1468 respectively, over the Sahara where the maximum values are found. On the contrary, from the timeseries
 1469 of the LW DREs for TOA and NETSURF it is evident the existence of a diurnal cycle with maximum
 1470 and minimum values around noon and during nighttime, respectively. Moreover, both DRE_{TOA} and
 1471 $\text{DRE}_{\text{NETSURF}}$ values are higher than zero, throughout the simulation period, indicating a warming LW
 1472 radiative effect. More specifically, the regional LW DRE_{TOA} ranges from 0.2 to 1.6 Wm^{-2} and
 1473 $\text{DRE}_{\text{NETSURF}}$ varies between 1.7 and 4 Wm^{-2} for the whole simulation domain (NSD). The corresponding

- Deleted: .
- Formatted: No underline, Font color: Auto, Superscript
- Deleted: 30
- Deleted: 22
- Deleted: 50
- Formatted: No underline, Font color: Auto, Superscript
- Deleted: the NMMB and the Sahara domain
- Deleted: 57
- Deleted: SDD
- Deleted: do not change with time, against a slight decrease in MSD to -40 Wm^{-2}
- Deleted: Hence, our results show that during the first 36 forecast hours, the computed DRE_{SURF} and $\text{DRE}_{\text{NETSURF}}$ values in MSD are larger than in SDD, while SDD is the source area of dust outbreaks. This can be explained by the fact that the massive dust loads originating across the Sahara "enter" ve...
- Deleted: 15
- Formatted: ...
- Deleted: 20
- Deleted: 10
- Formatted: ...
- Formatted: ...
- Deleted: 14
- Formatted: ...
- Deleted: 1
- Formatted: ...
- Deleted: 25
- Formatted: ...
- Deleted: 1
- Formatted: ...
- Formatted: Font: 12 pt, No underline, Font color: Auto
- Deleted: Finally, due to the gradually decreasing desert du...
- Deleted: clear
- Deleted: 8
- Deleted: 9
- Deleted: 4.3
- Deleted: in the NSD and SDD while slightly lower values...
- Deleted: 1
- Deleted: 3
- Deleted: 4
- Deleted: 2
- Deleted: 9
- Deleted: 8

1532 maximum DREs for the SDD and MSD are higher by up to 3.6 Wm^{-2} and lower by up to 1.1 Wm^{-2} ,
 1533 respectively. Dust aerosols act like greenhouse gases (Miller and Tegen, 1998) trapping the outgoing
 1534 terrestrial radiation while at the same time emit radiation at longer wavelengths back to the ground
 1535 explaining thus the positive LW DREs for TOA (planetary warming) and NETSURF (surface warming).
 1536 In addition, the aforementioned LW DREs (TOA and NETSURF) covariate with time revealing that the
 1537 sign and the magnitude of the LW DRE_{TOA} are determined by the perturbation of the surface radiation
 1538 budget (LW $\text{DRE}_{\text{NETSURF}}$) since the LW DRE_{ATM} values are almost constant throughout the simulation
 1539 period. This is in contrast to the corresponding finding for the SW radiation where the dust outbreaks'
 1540 impact on the Earth-Atmosphere system's radiation budget is regulated by the perturbation of the
 1541 radiation fields into the atmosphere (ATM) and at the surface (NETSURF). Finally, between SDD and
 1542 MSD remarkably stronger LW DREs are found for the former domain due to the higher dust loads over
 1543 the Sahara as well as due to the larger size of mineral particles close to the source areas.

1544 As it has been shown from the above analysis, the dust DREs between short and long wavelengths are
 1545 reverse (except at TOA over the Sahara around midday) and in order to assess the impact of desert dust
 1546 outbreaks in the whole spectrum the regional all-sky NET (SW+LW) DREs have been also analyzed
 1547 (bottom row in Fig. 5). During sunlight hours, the NET DREs result from the compensation of the SW
 1548 and LW effects while during night the NET and the LW DREs are equal attributed to the absence of SW
 1549 radiation. Based on our results, in the NSD, the DRE_{TOA} , DRE_{SURF} , $\text{DRE}_{\text{NETSURF}}$ and DRE_{ATM} range from
 1550 -8.5 to 0.5 Wm^{-2} , from -31.6 to 2.1 Wm^{-2} , from -22.2 to 2.2 Wm^{-2} and from -1.7 to 20.4 Wm^{-2} ,
 1551 respectively. In the SDD, the corresponding NET DREs vary from -9.3 to 5.9 Wm^{-2} , from -42.2 to 3.5
 1552 Wm^{-2} , from -2.3 to 3.6 Wm^{-2} and from -3.5 to 27.2 Wm^{-2} , respectively. Over the Mediterranean, the DREs
 1553 for TOA range from -10.7 to 0.5 Wm^{-2} , for SURF from -33.6 to 1.7 Wm^{-2} , for NETSURF from -26.7 to
 1554 1.7 Wm^{-2} and for ATM from -1.3 to 19.3 Wm^{-2} .

1555 At noon, the SW planetary cooling dominates over the LW planetary warming resulting thus to
 1556 negative DRE_{TOA} values over the simulation (NSD) and the Mediterranean (MSD) domains. On the
 1557 contrary, in the SDD, both SW and LW DRE_{TOA} are positive due to the higher surface albedo and the
 1558 trapping of the surface upward LW radiation by mineral particles, respectively, leading to a net warming
 1559 of the Earth-Atmosphere system. In the atmosphere, for the three domains, the negative LW DREs offset
 1560 by about 8-26% the positive SW ones resulting to an overall warming effect (positive NET DRE_{ATM})
 1561 around midday. Moreover, at noon, the increase of the absorbed LW radiation at the ground offsets the
 1562 decrease of the absorbed SW radiation by about 14-18% resulting in a NET surface cooling (negative

Deleted: 0....5... Wm^{-2} and lower by up to 1.2

Deleted: clear...ll-sky NET (SW+LW) DREs have been also analyzed (bottom row in Fig. 5). During sunlight hours, the NET DREs result from the compensation of the SW and LW effects while during night the NET and the LW DREs are equal attributed to the absence of SW radiation. Based on our results, in the NSD, the DRE_{TOA} , DRE_{SURF} , $\text{DRE}_{\text{NETSURF}}$ and DRE_{ATM} range from -8.513.9...to 0.52.6... Wm^{-2} , from -3143...6 to 2.14... Wm^{-2} , from -226...23...to 2.23.9... Wm^{-2} and from -13...7 to 20.48... Wm^{-2} , respectively. In the SDD, the corresponding NET DREs vary from -11...9 ... to 7...1 9 Wm^{-2} , from -46...2.3 ... to 4...3 ... Wm^{-2} , from -24.7... to 4.2...6 Wm^{-2} and from -4.1...5 to 30...7.2 Wm^{-2} , respectively. Over the Mediterranean, the DREs for TOA range from -23...0.7 to 0.9 ... Wm^{-2} , for SURF from -53...3.5 ... to 4...1 ... Wm^{-2} , for NETSURF from -39...6.4 7 to 4...2 ... Wm^{-2} and for ATM from -4 ...3 to 25...9.5 ... 3 Wm^{-2} . Moreover, due to the reduction of the desert dust outbreaks' intensity for increasing forecast hours (Figure S2-i) the associated direct radiative effects are also reduced within the MSD.

Deleted: counterbalances ...ominates over the LW planetary warming resulting thus to almost zero...egative DRE_{TOA} values (null effect) ...ver the whole ...imulation (NSD) and the Mediterranean (MSD) domains (NSD)... On the contrary, in the SDD, both SW and LW DRE_{TOA} are positive due to the higher surface albedo and the trapping of the surface upward LW radiation by mineral particles, respectively, leading to a net warming of the Earth-Atmosphere system. In the broader Mediterranean area (MSD), the SW effects at TOA (planetary cooling) dominate over the corresponding effects at longer wavelengths (planetary warming) explaining thus the negative NET DRE_{TOA} values (planetary cooling)...n the atmosphere, for the three domains, the negative LW DREs offset by about 12...-14...6% the positive SW ones resulting to an overall warming effect (positive NET DRE_{ATM}) around midday. Moreover, at noon, the increase of the absorbed LW radiation at the ground offsets the decrease of the absorbed SW radiation by about 20...4-24

1658 NET DRE_{NETSURF}) over the simulation domain. The corresponding levels for the SDD and MSD vary
1659 from 2.4 to 2.6% and from 0.9 to 1.3%, respectively.

1660 Beyond the hourly and day-to-day variability of dust DREs, the results were averaged over the total
1661 84-hour simulation period and the results are given, for the three domains, in Table 2, separately for the
1662 SW, LW and NET radiation. At TOA, desert dust outbreaks cause a net planetary cooling with all-sky
1663 NET DRE_{TOA} values equal to -2.6 ± 3.2 , -1.3 ± 5 and -3.8 ± 3.8 Wm⁻² for the NSD, SDD and MSD,
1664 respectively. Note, that due to the very strong temporal variability of DREs at TOA, the computed
1665 standard deviations are higher than the averages in the NSD and SDD in contrast to MSD where are
1666 equal. The negative averaged NET DRE_{TOA} in SDD is attributed to the planetary cooling found at early
1667 morning and afternoon hours. Wang et al. (2011) showed that when solar altitude is low (i.e. high solar
1668 zenith angle) DRE at TOA is getting negative even over high-albedo deserts. Similar results reported
1669 also by Banks et al. (2014), who studied the daytime cycle of dust DREs during the Fennec campaign
1670 held in the central Sahara in June 2011. Our results for the DRE_{TOA} in the MSD are within the ranges
1671 reported in previous studies (e.g. Valenzuela et al., 2012; Sicard et al., 2014 a;b) dealing with dust
1672 intrusions in the Mediterranean. In the atmosphere, mineral particles cause an overall atmospheric
1673 warming with NET DRE_{ATM} levels varying from 6.9 ± 8.3 (MSD) to 7.8 ± 11.7 Wm⁻² (SDD). On average,
1674 dust outbreaks reduce the downwelling NET radiation at the ground (DRE_{SURF}) by up to -14.7 ± 14.6 Wm⁻²
1675 (NSD), -18.0 ± 19.3 Wm⁻² (SDD) and -14.2 ± 14 Wm⁻² (MSD) while the corresponding DRE_{NETSURF}
1676 levels are equal to -9.6 ± 10.2 Wm⁻², -9.1 ± 11.2 Wm⁻² and -10.8 ± 11.2 Wm⁻², respectively. Our results for
1677 the SW and LW radiation in the SDD are in a good agreement with the annual averages for the year 2008
1678 presented by Nabat et al. (2012) over Northern Africa.

1679 5.3. Impact on sensible and latent heat fluxes

1680 As it has been shown in previous section, dust outbreaks exert a strong perturbation of the surface
1681 radiation budget by reducing and increasing the absorbed NET radiation at the ground during day and
1682 night, respectively. As a response to these disturbances, the surface heat fluxes, both sensible (SH) and
1683 latent (LE), associated with the transfer of energy (heat) and moisture between surface and atmosphere,
1684 also change in such a way trying to balance the gain or the loss of energy at the ground (Miller and Tegen,
1685 1998). Subsequently, variations of SH and LE have impact on the components of the hydrological cycle
1686 (Miller et al., 2004b) as well as on the turbulent kinetic energy and momentum transfer which in turn
1687 affect near surface winds and dust emission (Pérez et al., 2006). Moreover, Marcella and Eltahir (2014)
1688 and Kumar et al. (2014) have shown that due to the presence of dust aerosols into the atmosphere, the

Deleted: 5... to 28...% and from 14... to 15...%, respectively. In addition, the increase of the downwelling LW radiation at the ground offsets by up to 8% the decrease of the downward SW radiation resulting in negative NET DRE_{SURF} values across the Sahara Desert (i.e. SDD).

Deleted: The results are similar for the three domains, as to their physical meaning, i.e. dust produces a SW cooling/heating of surface/atmosphere, resulting in a planetary SW cooling, against a LW heating/cooling of surface/atmosphere, yielding a planetary LW heating. ...t TOA, desert dust outbreaks cause a net planetary cooling with clear...ll-sky NET DRE_{TOA} values equal to -3.4 ± 5.6 , 1.6 ± 6.1 and -8.2 ± 8.2 Wm⁻² for the NSD, SDD and MSD, respectively. Note, that due to the very strong temporal variability of DREs at TOA, the computed standard deviations are considerably ...higher than the averages in the NSD and SDD in contrast to MSD where are equal. Yoshioka et al., (2007), based on long-term simulations, reported a negative DRE_{TOA} (-4.73 Wm⁻²) averaged over North Africa (mean dust AOD equal to 0.39) and Heald et al. (2014) found that the all-sky NET DRE_{TOA} values vary from -3 to 4 Wm⁻² across the Sahara for the year 2010. Woodage and Woodward (2014) and Zhao et al., (2011) calculated positive DREs at TOA, averaged for the northwestern Africa, equal to 4.74 Wm⁻² and 0.83 Wm⁻², respectively. ...he negative averaged NET DRE_{TOA} in SDD is attributed to the planetary cooling found at early morning and afternoon hours. Wang et al. (2011) showed that when solar altitude is low (i.e. high solar zenith angle) DRE at TOA is getting negative even over high-albedo deserts. Similar results reported also by Banks et al. (2014), who studied the daytime cycle of dust DREs during the Fennec campaign held in the central Sahara in June 2011. Our results for the DRE_{TOA} in the MSD are within the ranges reported in previous studies (e.g. Valenzuela et al., 2012; Sicard et al., 2014 a;b) dealing with dust intrusions in the Mediterranean. From the comparison of the SW and LW DRE_{TOA}, it is found that the LW planetary warming offsets the SW planetary cooling by 33.3% in the NSD, by 52.9% in the SDD and by 15.4% in the MSD. ...n the atmosphere, mineral particles cause an overall atmospheric warming with NET DRE_{ATM} levels varying from 6.97 to 11.7 Wm⁻² (MSD) to 8.3 to 13.17 Wm⁻² (SDD) while the offset of the SW atmospheric warming by the LW atmospheric cooling ranges from 31.1% to 33.6% among the study domains... On an average, dust outbreaks reduce the downwelling NET

Deleted: .1...2

Deleted: 9

Deleted: 22...4.7...±23.6...4 Wm⁻² (MSD) while the corresponding DRE_{NETSURF} levels are equal to -9.11 ± 13.04 Wm⁻², -9.9 ± 12.14 Wm⁻² and -15.06 ± 17.15 Wm⁻², respectively. Our results for the SW and LW radiation in the SDD are in a good agreement with the annual averages for the year 2008 presented by Nabat et al. (2012) over Northern Africa. Santese et al.

Formatted: No underline, Font color: Auto, English (United States)

Formatted: No underline, Font color: Auto, English (United States)

Formatted: No underline, Font color: Auto, English (United States)

1878 daytime surface sensible heat fluxes are reduced leading to a reduction of the planetary boundary layer
1879 (PBL) height.

1880 Here, we are investigating the impact of desert dust outbreaks on SH and LE over the simulation
1881 domain (NSD). It must be clarified that our analysis is restricted only above land areas since we are
1882 looking at short ~~range effects and the atmospheric driver is not coupled with an ocean model~~. The
1883 timeseries of the regional SH and LE values, over the forecast period, based on the RADON (red curve)
1884 and RADOFF (blue curve) configurations of the model are presented in Figures 6-i (for SH) and 6-ii (for
1885 LE). Each curve corresponds to the mean levels calculated from the 20 desert dust outbreaks while the
1886 shaded areas represent the associated standard deviations. According to our results, SH is characterized
1887 by a diurnal variation with maximum values ($\sim 350 \text{ Wm}^{-2}$) at noon and minimum ones ($\sim -30 \text{ Wm}^{-2}$)
1888 during nighttime (Fig. 6-i). Nevertheless, during sunlight hours, the surface sensible heat fluxes simulated
1889 in the RADON experiment are lower by up to 45 Wm^{-2} in comparison to the RADOFF outputs. At night,
1890 an opposite tendency is recorded and the RADON SH fluxes are higher by up to 2 Wm^{-2} than the
1891 corresponding fluxes based on the RADOFF configuration of the model. The reverse effects on SH
1892 levels, over the western parts of the Sahara, between daytime and nighttime as well as the diurnal
1893 variability of their magnitude have been pointed out by Zhao et al. (2011). Based on the paired t-test, the
1894 differences between RADOFF and RADON SH values are statistical significant at 95% confidence level
1895 throughout the forecast period. At local scale (geographical distributions), among the studied cases, in
1896 areas where the desert dust outbreaks' intensity is maximized, the SH fluxes are reduced by up to 150
1897 Wm^{-2} during day and increased by up to 50 Wm^{-2} during night. Our findings are consistent with those
1898 presented by Mallet et al. (2009) and Rémy et al. (2015) who analyzed the impact of dust storms on
1899 sensible heat fluxes over W. Africa and Mediterranean, respectively, and substantially higher than the
1900 instantaneous perturbations of SH calculated by Kumar et al. (2014), who studied a dust outbreak that
1901 occurred in northern India (17-22 April 2010).

1902 The diurnal variation of the latent heat fluxes (Fig. 6-ii) is identical to that of sensible heat fluxes;
1903 however, LE levels are remarkably lower than the regional averages of SH. This is attributed to the lower
1904 soil water content and limited evaporation in arid regions (Ling et al., 2014). Based on our simulations,
1905 LE values at noon gradually decrease both for the RADOFF (blue) and RADON (red) experiments over
1906 the forecast period attributed to the too moist initialization of the model (Note that the model is initialized
1907 with FNL analysis produced by a different model (GFS)). Nevertheless, the latter LE values are lower
1908 than the former ones by up to 4 Wm^{-2} indicating that desert dust outbreaks reduce the latent heat fluxes
1909 leaving from the ground. The reliability of this finding is further supported by the fact that the RADOFF-

Deleted: -term effects and also in the existing version of the NMMB-MONARCH model the atmospheric driver is not coupled with an ocean model

Deleted: leading thus to a predominance of the sensible heat fluxes

Deleted: probably

1916 RADON differences are statistically significant at 95% confidence level. During night, the RADON LE
1917 values are slightly higher (less than 0.5 Wm^{-2}) with respect to the corresponding ones simulated in the
1918 RADOFF configuration. The instantaneous reduction and increase of LE (results not shown here) can be
1919 as large as -100 Wm^{-2} and $20\text{-}30 \text{ Wm}^{-2}$, respectively. Finally, in contrast to SH, the spatial features of LE
1920 anomalies are not identical with those of $\text{DRE}_{\text{NETSURF}}$ since other parameters (e.g. soil moisture) regulate
1921 also the latent heat fluxes (Marcella and Eltahir, 2014).

Deleted: are substantially higher than the regional perturbations and

1922 *5.4. Impact on temperature fields*

1923
1924
1925 Through the perturbation of the radiation it is expected that desert dust outbreaks will affect also the
1926 temperature fields. In order to quantify these impacts, the temperature differences between the RADON
1927 and RADOFF simulations, both at 2 meters and in vertical, are analyzed. In Figure 7, are displayed the
1928 RADON-RADOFF anomaly maps of temperature at 2 meters at 12 (i), 24 (ii), 36 (iii) and 48 (iv) hours
1929 after the initialization of the forecast period on 2nd August 2012 at 00 UTC. At noon, the highest negative
1930 biases (down to -4 K) are observed over land areas where the intensity of dust loads is high (see the first
1931 and third row in the first column in Fig. 4) due to the strong reduction of the NET radiation reaching the
1932 ground by the mineral particles. Similar findings, under dust episode conditions, have been also reported
1933 by previous studies conducted for the Mediterranean (Pérez et al., 2006), across the Sahara (Helmert et
1934 al., 2007; Heinold et al., 2008; Stanelle et al., 2010) and in East Asia (Kumar et al., 2014; Ling et al.,
1935 2014). Over dust-affected maritime areas, due to the higher heat capacity of the sea, the temperature
1936 differences between the RADON and RADOFF experiments are almost negligible at these time scales.
1937 During nighttime, dust aerosols emit radiation at thermal wavelengths increasing thus the near surface
1938 temperature when the dust-radiation interactions are included into the numerical simulations (RADON
1939 experiment). For this reason, the RADON-RADOFF temperature differences at 2 meters become positive
1940 (up to 4 K) at 24 and 48 forecast hours over land areas where the “core” of the dust plume is observed.
1941 The reduction and the increase of the near surface temperature during daytime and nighttime,
1942 respectively, either solely or as a combined result indicate that the temperature diurnal range is reduced
1943 due to desert dust outbreaks.

Deleted: by the mineral particles

1944 The vertical distribution of dust layers determines their impacts on radiation with altitude which in
1945 turn modify the temperature profiles (Meloni et al., 2015) and subsequently affect convection (Ji et al.,
1946 2015), cloud development (Yin and Chen, 2007), precipitation (Yin et al., 2002) and wind profiles
1947 (Choobari et al., 2012). In order to investigate the impacts of desert dust outbreaks on temperature fields
1948 into the atmosphere, we have reproduced the altitude-latitude cross sections (up to 8 km above mean sea

1952 level, m.s.l.) of RADON-RADOFF temperature differences on 4 April 2003 at 12 UTC along the
1953 meridional 30° E (Fig. 8 ii-a) and on 7 March 2009 at 00 UTC along the meridional 10° E (Fig. 8 ii-b).
1954 In addition, the corresponding cross sections of dust concentration (in kg m^{-3}) are shown in Figures 8 i-
1955 a and 8 i-b, respectively. At midday, an elevated dust layer extends from 1.5 to 6 km m.s.l., between 23°
1956 N and 33° N, with dust concentrations up to $0.8 \times 10^{-6} \text{ kg m}^{-3}$ while a low elevated dust layer extends from
1957 the surface up to 1.5 km m.s.l., between 27° N and 31° N, with concentrations up to $10^{-6} \text{ kg m}^{-3}$ (Fig 8 i-
1958 a). Along the cross-section, the simulated columnar dust AOD at 550 nm reaches up to 1.21. Based on
1959 the cross section of temperature differences (Fig. 8 ii-a), dust aerosols via the absorption of solar radiation
1960 warm the atmospheric layers by up to 0.8-0.9 K between altitudes where the high-elevated dust layer is
1961 located. On the contrary, below the dust cloud, mineral particles cool the lowest tropospheric levels (by
1962 up to 1.3 K) by attenuating the incoming solar radiation. Note that between the parallels 31° N and 35°
1963 N, where dust loads are recorded at low altitudes (below 2 km), higher temperatures by up to 0.3 K are
1964 simulated in the RADON experiment with respect to RADOFF, revealing thus an atmospheric warming
1965 near surface. Also, it must be considered that in this area mineral particles are suspended over sea, where
1966 the impacts on sensible heat fluxes are negligible, making therefore evident the dust warming effect at
1967 low atmospheric levels in contrast to land areas (parallels between 27° N and 31° N), where the near
1968 surface temperature is reduced because of the reduction of the sensible heat fluxes, as it has been shown
1969 also by Pérez et al. (2006, Fig. 10). Therefore, the vertical distribution of dust loads plays a significant
1970 role regarding their impact on near surface temperature which in turn may affect winds and subsequently
1971 dust emission (Stanele et al., 2010; Huang et al., 2014). Above the high-elevated dust layer, negative
1972 RADON-RADOFF temperature differences (down to -0.3 K) are found indicating an atmospheric
1973 cooling attributed to the dust albedo effect (Spyrou et al., 2013).

1974 In the second example, on 7th March 2009 at 00 UTC, a dust layer extends from the southern parts of
1975 the NSD domain to the northern parts of Tunisia, between surface and 4 km m.s.l. (Fig. 8 i-b). Along the
1976 dust plume, with AODs reaching up to 1.40, moderate concentrations (up to $0.5 \times 10^{-6} \text{ kg m}^{-3}$) are
1977 simulated between 15° N and 20° N, low (less than $0.2 \times 10^{-6} \text{ kg m}^{-3}$) between 20° N and 25° N while the
1978 maximum ones (higher than $2 \times 10^{-6} \text{ kg m}^{-3}$) are recorded between 25° N and 35° N. Due to the emission
1979 of LW radiation by mineral particles, dust aerosols cool the atmospheric layers (Otto et al., 2007) in
1980 which they reside, by up to 0.8 K, and increase the temperature, by up to 0.4 K, just above the dust layer.
1981 Between the bottom of the dust layer and surface, positive RADON-RADOFF temperature differences
1982 (i.e. warming) up to 1.2 K are calculated as indicated by the red colors following the model topography

Deleted: (through scattering and absorption)

(grey shaded). Nevertheless, this near surface warming is “interrupted”, being null or even reverse (i.e. cooling), in areas where the dust layer abuts the ground.

Deleted: Mineral particles emit LW radiation and trap the outgoing terrestrial radiation explaining thus the warming effect of dust outbreaks close to the ground during nighttime.

5.5. Feedbacks on dust emission and dust aerosol optical depth

In the present section, focus is given on the investigation of the potential feedbacks on dust AOD (at 550 nm) and dust emissions attributed to dust radiative effects. To this aim, the timeseries of the regional averages and the associated standard deviations, throughout the forecast period (84 hours), calculated from the 20 desert dust outbreaks for both parameters, based on the RADON (red) and RADOFF (blue) experiments, are analyzed and the obtained results are shown in Figure 9. Over the simulation period, the RADOFF dust AOD_{550nm} gradually increases from 0.31 to 0.34 in contrast to the corresponding outputs from RADON that are gradually decreasing down to 0.29 (Fig. 9-i). The positive RADOFF-RADON differences of dust AOD, indicating a negative feedback when the dust-radiation interactions are considered into the numerical simulations, are getting evident 12 hours (0.005 or 2%) after the initialization of the forecast period and amplify with time (up to 0.036 or 12%), being also statistical significant (paired t-test, confidence level at 95%) at each forecast step. The observed negative feedbacks on dust AOD have been also pointed out in relevant studies (Pérez et al., 2006; Wang et al., 2010) carried out for specific desert dust outbreaks. Through the comparison of the mean dust AOD levels, calculated over the 84-h simulation period, based on RADON (0.288) and RADOFF (0.308) simulations, it is revealed a statistical significant reduction by 0.02 (6.9 %) attributed to the dust radiative effects. Among the 20 desert dust outbreaks, these reductions vary from 1% (22 February 2004) to 12.5% (27 January 2005) and are statistical significant at 95 % confidence level in all cases.

Deleted: ; however, the reductions of mineral particles' loads were significantly higher compared to our calculations corresponding to averages of the 20 studied desert dust outbreaks. More specifically, Pérez et al. (2006) found a reduction of the regional dust AOD by up to 35-45 % and in Wang et al. (2010) the corresponding reductions were ranging between 10 and 45%

A similar analysis has been also made for the dust emissions (in kg m⁻²) aggregated over the whole simulation domain (NSD, outer domain in Figure 1) and the overall results are given in Figure 9-ii. Dust emissions are maximized around midday (Cowie et al., 2014) and are very weak during night. Based on the RADOFF simulation, the highest amounts of emitted dust are increased from 2 to 2.5 kg m⁻² throughout the hindcast period. This increasing tendency is encountered also in the RADON experiment but the emitted dust amount is lower. The positive RADOFF-RADON anomalies during daytime range from 0.1 to 0.4 kg m⁻² and are statistical significant at 95% confidence level based on the paired t-test. Therefore, desert dust outbreaks exert a negative feedback on dust emission explaining thus the reduction of dust AOD. The lower amounts of emitted dust, modelled based on the RADON configuration, result from a chain of processes triggered by the surface cooling which decreases the turbulent flux of sensible heat into the atmosphere, weakening the turbulent mixing within the PBL and the downward transport

Deleted: First, for each case and in each forecast step, the dust emissions from all grid points within the NSD are aggregated. Then, the mean and the standard deviation values are computed from the 20 desert dust outbreaks which are analyzed and the overall results are given in Figure 9-ii. Moreover, the total dust emissions at each forecast step are added and the obtained results, separately for the RADON and RADOFF configuration of the model, are provided into the parentheses in the legend of Figure 9-ii.

Deleted: ; however, the dust emission is lower compared to the simulation in which the dust-radiation interactions are neglected (RADOFF)

2039 of momentum to the surface and subsequently reduces surface wind speed and dust emission (Miller et
2040 al., 2004a; Pérez et al., 2006).

2041 During the simulation period, the total emitted amount of desert dust (~~parentheses in the legend of~~
2042 ~~Figure 9-ii~~) is equal to 18.279 and 21.849 kg m⁻² based on the RADON and RADOFF, respectively.
2043 Therefore, desert dust outbreaks cause a negative feedback on dust emissions reducing them by 3.57 kg
2044 m⁻² (-19.5%). This reduction ~~is~~ consistent in all the studied cases of our analysis varying from 0.6 kg m⁻²
2045 (~10%, 24 February 2006) to 6.6 kg m⁻² (~34%, 2 August 2012). Negative feedbacks on dust AOD and
2046 dust emissions have been also pointed out in previous studies based on short- (e.g. Ahn et al., 2007;
2047 Rémy et al., 2015) and long-term (e.g. Perlwitz et al., 2001; Zhang et al., 2009) simulations. Woodage
2048 and Woodward (2014) relied on climatic simulations of the HiGEM model, found a positive feedback
2049 on global dust emissions which is in contradiction with findings reported in the majority of the existing
2050 studies. The authors claimed that this discrepancy could be explained by the absence of mineral particles
2051 with a radius larger than 10 µm in the emitted dust size distribution leading thus to an underestimation
2052 of the LW effects. It must be clarified that according to our results negative feedbacks on dust emission
2053 are found at a regional scale. Stanelle et al. (2010) showed that the vertical distribution of dust aerosols
2054 determines their impacts on atmospheric stability and wind patterns and subsequently the associated
2055 feedbacks on dust emissions which can be even positive at a local scale. This highlights the importance
2056 of studying the potential feedbacks on mineral particles' loads as well as on their emissions spatially by
2057 analyzing all the contributor factors.

Deleted: (i.e. positive RADOFF-RADON differences) is

2058 5.6. Assessment of the radiation at the ground

2059 The performance of the NMMB-MONARCH model in terms of reproducing the downward SW and
2060 LW radiation is assessed using as reference data ground measurements derived from the Baseline Surface
2061 Radiation Network (BSRN, Ohmura et al., 1998). Through this analysis it is attempted to quantify
2062 objectively the potential improvements of the model's predictive skills attributed to the inclusion of the
2063 dust radiative effects into the numerical simulations. Globally, 59 BSRN stations are installed at different
2064 climatic zones providing radiation measurements (<http://bsrn.awi.de/>) of high accuracy at very high
2065 temporal resolution (1 min) (Roesch et al., 2011). For the evaluation analysis, we have used the global
2066 (direct and diffuse) shortwave and longwave downwelling radiation at the ground measured at 6 stations
2067 (magenta star symbols in Figure 1) located in Spain (Izana, Cener), France (Palaiseau, Carpentras),
2068 Algeria (Tamanrasset) and Israel (Sede Boker).

Deleted: , a project of the Data and Assessments Panel from the Global Energy and Water Cycle Experiment (GEWEX, <http://www.gewex.org/>) under the umbrella of the World Climate Research Programme (WCRP, <https://www.wcrp-climate.org/>)

2077 In Figure 10, are presented the timeseries of the measured (red curve) SW (i-) and LW (ii-) radiation
2078 at Sede Boker and the corresponding model outputs based on the RADON (black curve) and the
2079 RADOFF (blue curve) experiments, for the periods 22 February 2004 00 UTC – 25 February 2004 12
2080 UTC (-a) and 21 April 2007 00 UTC – 24 April 2007 12 UTC (-b). In the bottom row of Fig. 10 are also
2081 provided the temporal evolution of the model dust AOD_{550nm} and the Level 2 AERONET total AOD_{500nm}
2082 (red x symbols) retrieved via the O’Neill algorithm (O’Neill et al., 2003). Moreover, the AERONET
2083 Ångström exponent (alpha) retrievals (denoted with green x symbols) are used as an indicator of coarse
2084 or fine particles predominance into the atmosphere. For the comparison between model and observations,
2085 the nearest grid point to the stations’ coordinates is utilized. In Sede Boker, the model’s grid point
2086 elevation is 465 m being slightly lower than the AERONET (480 m) and BSRN (500 m) stations, and
2087 therefore these small altitude differences do not affect substantially the intercomparison results.
2088 Likewise, the SW and LW radiation are measured from 0.295 to 2.8 μm and from 4 to 50 μm,
2089 respectively, while the spectral intervals in the model’s radiation transfer scheme span from 0.2 to 12.2
2090 μm and from 3.3 to 1000 μm in the shortwave and longwave spectrum, respectively. These differences
2091 might contribute to the level of agreement between model and observations; however, are not discussed
2092 in our evaluation analysis.

2093 In both examples presented here, but also for the rest of our dataset, the model captures better the
2094 temporal variation of the downwelling SW in contrast to the LW radiation at the ground with correlation
2095 coefficients (R) higher than 0.96 and between 0.63 and 0.85, respectively. However, the model-BSRN
2096 biases vary strongly in temporal terms because of the inability of the model to reproduce adequately the
2097 amount of the suspended mineral particles. For the first desert dust outbreak (left column in Fig. 10),
2098 during the first forecast day, the maximum measured SW radiation is higher by about 150 Wm⁻² than the
2099 simulated RADON outputs and slightly lower than the corresponding RADOFF levels. The former is
2100 explained by the facts that the model reproduces the dust peak earlier than actually recorded according
2101 to AERONET observations (see Figure 10 iii-a) and it develops low-level clouds (cloud fractions
2102 between 0.5 and 0.6) while the latter one is attributed to the absence of radiative effects. For the rest of
2103 the simulation period, the model overestimates and underestimates the shortwave and longwave
2104 radiation, respectively, due to its deficiency to reproduce (underestimation) the amount of dust aerosols.
2105 More specifically, based on AERONET retrievals, AOD and alpha levels vary from 0.2 to 0.4 and from
2106 0.2 to 0.7, respectively, indicating the existence of dust loads of moderate intensity. On the contrary, the
2107 simulated dust AOD at 550 is less than 0.1 in both model configurations characterized by a “flat”
2108 behavior in temporal terms. Over the simulation period (22 February 2004 00 UTC – 25 February 2004

Deleted: (minimum Euclidean distance)

Deleted: dust

2111 12 UTC), the mean SW (LW) radiation based on BSRN, RADON and RADOFF is equal to 221.6 Wm⁻²
2112 (290.0 Wm⁻²), 255.4 Wm⁻²(266.4 Wm⁻²) and 272.7 Wm⁻²(264.7 Wm⁻²), respectively. Thanks to the
2113 consideration of the dust radiative effects, the positive model-BSRN biases in the shortwave spectrum
2114 are reduced from 51.1 Wm⁻² (RADOFF-BSRN) to 33.9 Wm⁻² (RADON-BSRN) while the negative
2115 model-BSRN biases in the longwave spectrum are reduced from -25.3 Wm⁻² (RADOFF-BSRN) to -23.6
2116 Wm⁻² (RADON-BSRN).

2117 In the second case which is analyzed (right column in Fig. 10), two peaks are simulated with dust
2118 AOD_{550nm} values up to 0.9 (midday on 23rd April 2007) and 0.5 (afternoon on 21st April 2007). For the
2119 major one, the model clearly overestimates aerosol optical depth with respect to AERONET retrievals in
2120 which AOD (red x symbols) varies between 0.2 and 0.3 and alpha (green x symbols) ranges from 0.3 to
2121 0.5 while the second one cannot be confirmed due to the lack of ground observations. Note, that between
2122 09 UTC and 15 UTC on 23rd April 2007, the model underestimates the SW radiation by up to 200 Wm⁻²
2123 while overestimates the LW radiation by up to 150 Wm⁻² (maximum overestimations throughout the
2124 simulation period) due to the misrepresentation of the dust AODs. Even higher model overestimations
2125 of the SW radiation are observed at 12 UTC on 22 April 2007, attributed mainly to the inability of the
2126 model to reproduce satisfactorily clouds, since the negative model-AERONET differences of AOD
2127 cannot explain these large discrepancies in radiation. Clouds play an important role in such comparisons,
2128 particularly when their features are not well reproduced by the model, leading to large overestimations
2129 or underestimations, by up to 600 Wm⁻² in absolute terms among the studied cases of the present analysis,
2130 as it has been pointed out in previous studies (e.g. Spyrou et al., 2013). Finally, the model (RADON)
2131 overestimation of the SW radiation reaching the ground, by up to 200 Wm⁻² at 09 UTC on 21 April 2007,
2132 is probably associated with underestimation of the simulated dust AOD since fair weather conditions are
2133 forecasted and confirmed by the true color MODIS-Terra images ([http://modis-
2134 atmos.gsfc.nasa.gov/IMAGES/](http://modis-atmos.gsfc.nasa.gov/IMAGES/)). For the SW radiation, the positive NMMB-BSRN biases during the
2135 simulation period (21 April 2007 00 UTC – 24 April 2007 12 UTC) are reduced from 69.0 Wm⁻² to 40.9
2136 Wm⁻² when dust-radiation interactions are activated (RADON) while lower positive biases for the LW
2137 radiation are calculated (0.7 Wm⁻²) when dust-radiation interactions are deactivated (RADOFF).
2138 Summarizing, in the majority of the studied desert dust outbreaks here, positive and negative model-
2139 observations biases are found for the downwelling SW (Table S2) and LW (Table S3) radiation,
2140 respectively, which are reduced when the dust-radiation interactions are activated. On the contrary,
2141 similar improvements are not evident on the correlation coefficients since are not found remarkable
2142 differences between RADON-BSRN and RADOFF-BSRN R values (results not shown).

Deleted: 1

Deleted: 2

2145 5.7. Assessment of the temperature fields versus analysis datasets

2146 The forecasting performance of the NMMB-MONARCH model has been also assessed for the
2147 temperature fields, utilizing as reference final analyses (FNL) derived from the National Centers for
2148 Environmental Prediction database (<http://rda.ucar.edu/>). The evaluation of both model configurations
2149 (RADON and RADOFF) against FNL temperature at 2 meters and at 17 pressure levels into the
2150 atmosphere is made at a regional scale for the NSD. For the former intercomparison, only land grid points
2151 are taken into account, while for the latter one it is not applied any criterion regarding the surface type
2152 (land or sea). The evaluation of the model is made by considering grid points where the dust AOD is
2153 higher/equal than 0.1, 0.5 and 1.0, respectively. In order to overcome spatial inconsistencies between
2154 model and analyses, the model outputs have been regridded from their raw spatial resolution ($0.25^\circ \times$
2155 0.25° degrees) to $1^\circ \times 1^\circ$ degrees to match FNL. We note that analyses datasets are only “best” estimates
2156 of the observed states of the atmosphere and the surface produced by combining a model (in this case
2157 GFS) and available observations through data assimilation techniques. Analysis datasets are more poorly
2158 constrained by observations over certain regions including the arid and dusty ones, and more dependent
2159 on the model’s behavior. This is even more relevant for surface variables such as 2-m temperature which
2160 may heavily depend on the underlying model’s soil scheme.

2161 In Figure 11, are presented the regional biases (model-FNL) of temperature at 2 meters for the
2162 RADON (red curve) and RADOFF (blue curve) experiments, averaged from the 20 desert dust outbreaks
2163 every 6 hours of the hindcast period, considering only land grid points where the dust AOD is
2164 higher/equal than: (i) 0.1, (ii) 0.5 and (iii) 1.0. In order to avoid misleading interpretations, attributed to
2165 possible error compensations as a result of an erroneously representation of the dust patterns or optical
2166 properties (see Section 5.1), the corresponding root mean square error (RMSE) values have been
2167 calculated as well (Figure S23). The combination of these two skill scores (bias and RMSE) can provide
2168 information regarding the model departures (i.e., cold or warm biases) and how much “sensitive” is the
2169 level of agreement between NMMB-FNL due to large errors (outliers). Regardless the dust AOD
2170 threshold, cold biases are found during night and early morning hours, warm biases are calculated in the
2171 afternoon while the minimum biases in absolute terms appear at noon. According to our results, under
2172 low desert dust conditions (Fig. 11-i), the agreement between model and FNL is better when the dust
2173 radiative effects are neglected (RADOFF) during daytime, while slightly lower RADON-FNL biases
2174 compared to RADOFF-FNL ones are found during night. These trivial nocturnal “corrections” are not
2175 evident in the RMSE timeseries and therefore are not so trustworthy. At noon, the RADOFF-FNL biases

Deleted: ,except for the radiation (Section 5.6),

Deleted: since the atmospheric driver is not coupled with an ocean model

Deleted: representing low, moderate and intense dust load conditions

Deleted: of

2184 are almost zero (less than 0.1 K) whereas negative RADON-FNL biases (down to -0.27 K) are computed
2185 due to the surface cooling induced by the mineral particles. For moderate dust AODs (Fig. 11-ii), during
2186 night, the model-FNL temperature biases are lower, being in agreement also with the associated RMSE
2187 values (Fig. S23-ii), for the RADON configuration (less than 1 K) in contrast to the RADOFF simulation
2188 (less than 1.4 K) and these improvements are statistically significant at 95% confidence level.
2189 Nevertheless, at midday, the RADOFF-FNL biases are similar to those found for the lowest dust AOD
2190 threshold (Fig. 11-i), while the model cold biases, varying from -1.15 K (84 h) to -0.55 K (12 h), are
2191 amplified when the dust-radiation interactions are activated (RADON). The “corrections” of the near
2192 surface temperature forecasts during nighttime become more evident and statistically significant, when
2193 only land areas affected by intense dust loads (dust AOD ≥ 1.0) are considered in the NMMB-FNL
2194 comparison. Under these high dust AODs, the increase of air temperature at 2 meters due to the dust LW
2195 DREs reduces the existing cold biases and the RADON RMSE levels (Fig. S23-iii). Therefore, the
2196 improvements on model’s predictability of temperature at 2 meters when accounting for dust-radiation
2197 interactions, are more evident when the intensity of dust loads increases.

2198 The potential impacts of the dust radiative effects inclusion on the model’s forecasting ability have
2199 been also investigated for the temperature fields in vertical. For this purpose, from the 20 desert dust
2200 outbreaks, the temperature model-FNL biases at 17 pressure levels (from 1000 to 100 hPa) have been
2201 calculated for the RADOFF (black curve) and RADON (red curve) and the obtained results are illustrated
2202 in Figure 12. The corresponding vertical profiles for the RMSE are given in Figure S24. The assessment
2203 results are presented only 24 (a) and 48 (b) hours after the initialization of the forecast period since are
2204 not found remarkable differences between the two model configurations at noon (i.e. 12 and 36 UTC).

2205 Based on our findings, model warm biases are found between 950 and 700 hPa where most of the dust
2206 is confined (brown curve). For the lowest dust AOD threshold, these positive model-FNL biases reach
2207 up to 0.245 K and 0.313 K at 24 and 48 forecast hours, respectively, when mineral particles are not
2208 treated as radiatively active substance (RADOFF). On the contrary, when dust-radiation interactions are
2209 activated (RADON) the corresponding biases are reduced down to 0.155 K and 0.239 K, respectively,
2210 indicating a better model performance which is further supported by the fact that these improvements are
2211 statistical significant (95 % confidence level). In addition, slightly lower RMSEs are also calculated for
2212 the RADON configuration between 925 and 700 hPa (Fig. S24-i). Similar but more evident results are
2213 found when the dust AOD threshold increases from 0.1 to 0.5 (middle row in Figures 12 and S24-ii).
2214 More specifically, at 24 forecast hours, the RADON-FNL temperature differences do not exceed 0.321
2215 K in contrast to the corresponding biases between RADOFF and FNL which can be as high as 0.512 K.

Deleted: in

2217 At 48 forecast hours, between altitudes where the dust concentrations are maximized, the red curve
 2218 (RADON-FNL) is close to the blue thick line which represents the ideal score (i.e. zero biases), while
 2219 the RADOFF warm biases can reach up to 0.443 K. As it has been shown in Section 5.4 (see Fig. 8 ii-b),
 2220 due to the emission of longwave radiation by the mineral particles there is a temperature reduction within
 2221 the atmospheric layers in which they are confined and a slight warming above the dust layer. The former
 2222 effect explains the statistically significant reduction of the model warm biases between 950 and 700 hPa
 2223 whereas the latter one could explain the slight statistically significant reduction of the model cold biases
 2224 recorded between 600 and 500 hPa (see Fig. 12 ii-a). According to the RMSE vertical profiles, between
 2225 the two altitude ranges (950-700 hPa and 600-500 hPa), the better performance of the RADON
 2226 configuration is evident only at pressure levels where the main amount of dust is simulated (Fig. S24 ii-
 2227 a and ii-b). For the highest dust AOD threshold, at 24 forecast hours (Fig. 12 iii-a), the agreement of
 2228 temperature profiles between RADON and FNL is better compared to RADOFF-FNL whereas at 48
 2229 forecast hours depends on altitude (Fig. 12 iii-b). Summarizing, thanks to the consideration of the dust
 2230 radiative effects the predictive skills of the NMMB-MONARCH model in terms of reproducing
 2231 temperature fields within the atmosphere are improved as it has been pointed also in previous relevant
 2232 studies (Pérez et al., 2006; Wang et al., 2010; Wang and Niu, 2013). However, the improvements are
 2233 relatively small. The consideration of dust-radiation interactions does not always lead to a better model
 2234 performance since other model first order errors may dominate over the expected improvements. Also
 2235 the representation of dust plumes' spatiotemporal features and optical properties, particularly the AOD
 2236 and SSA, may produce double penalty effects. In this sense, the enhancement of dust forecasts via data
 2237 assimilation techniques may significantly improve the results.

2238 6. Summary and conclusions

2239 In the present study, the direct radiative effects (DREs) during 20 intense and widespread
 2240 Mediterranean desert dust outbreaks, that took place during the period March 2000 – February 2013,
 2241 have been analyzed based on short-term (84 hours) regional simulations of the NMMB-MONARCH
 2242 model. The identification of desert dust outbreaks has been accomplished via an objective and dynamic
 2243 algorithm utilizing as inputs daily 1° x 1° satellite retrievals providing information about aerosols' load,
 2244 size and nature. DREs have been calculated at the top of the atmosphere (TOA), into the atmosphere
 2245 (ATM), and at the surface, for the downwelling (SURF) and the absorbed (NETSURF) radiation, for the
 2246 shortwave (SW), longwave (LW) and NET (SW+LW) radiation. At a further step, the impacts on sensible
 2247 and latent heat fluxes as well as on temperature at 2 meters and into the atmosphere have been

Deleted: . Our findings are in agreement with previous studies in which similar evaluations have been made either against analyses datasets

Deleted:) or weather station observations (

Deleted: induced by

Deleted: (Gkikas et al., 2013; 2016)

Deleted: ,available at 1° x 1° spatial resolution,

Deleted: (AOD)

Deleted: (FF, α)

Deleted: (AI)

Deleted: The obtained results have been presented through geographical distributions as well as at regional level by averaging the clear-sky DREs over the whole simulation domain (NSD), the Sahara Desert (SDD) and the broader Mediterranean basin (MSD) sub-domains.

Deleted: of desert dust outbreaks

2266 investigated. Moreover, the potential feedbacks on dust emission and dust AOD have been assessed at
 2267 regional scale representative for the simulation domain used in our experiments. In the last part of our
 2268 study, focus was given on the potential improvements on model's predictive skills, attributed to the
 2269 inclusion of dust radiative effects into the numerical simulations, in terms of reproducing the downward
 2270 SW/LW radiation at the ground as well as the temperature fields. The main findings obtained from the
 2271 present analysis are summarized below.

Deleted: ,attributed to dust-radiation interactions,

2272
 2273 **Direct Radiative Effects**

- 2274 ➤ DREs into the atmosphere and at the surface are driven by the dust outbreaks' spatial features
 2275 whereas at TOA, the surface albedo plays a crucial role, particularly under clear sky conditions.
- 2276 ➤ At noon, dust outbreaks induce a strong surface cooling with instantaneous NET DRE_{SURF} and
 2277 DRE_{NETSURF} values down to -589 Wm⁻² and -337 Wm⁻², respectively.
- 2278 ➤ Through the absorption of the incoming solar radiation by the mineral particles, dust outbreaks
 2279 cause a strong atmospheric warming effect (by up to 319 Wm⁻²) around midday.
- 2280 ➤ At TOA, during daytime, positive DREs up to 85 Wm⁻² (planetary warming) are found over
 2281 highly reflective areas while negative DREs down to -184 Wm⁻² (planetary cooling) are computed
 2282 over dark surfaces.
- 2283 ➤ During nighttime, reverse effects of lower magnitude are found into the atmosphere and at the
 2284 surface with maximum instantaneous NET DRE_{SURF}, DRE_{NETSURF} and DRE_{ATM} values equal to
 2285 83 Wm⁻², 50 Wm⁻² and -61 Wm⁻² whereas at TOA due to the offset of the atmospheric cooling
 2286 by the surface warming, the DRE_{TOA} values are almost negligible (less than 10 Wm⁻²).
- 2287 ➤ The regional NET all-sky DREs for the NSD range from -8.5 to 0.5 Wm⁻², from -31.6 to 2.1 Wm⁻²,
 2288 from -22.2 to 2.2 Wm⁻² and from -1.7 to 20.4 Wm⁻² for TOA, SURF, NETSURF and ATM,
 2289 respectively.
- 2290 ➤ The contribution of the LW DREs to the NET ones is comparable or even larger, particularly over
 2291 the Sahara at midday.

Formatted: No underline, Font color: Auto, Subscript

Formatted: No underline, Font color: Auto, Superscript

Deleted: <#>Similar spatial patterns are revealed for the absorbed radiation at the ground; however, the magnitude of the NET DRE_{NETSURF} values is lower in comparison with the corresponding DREs for SURF.¶

Deleted: <#>can increase the

Deleted: <#>radiation budget (warming effect)

Deleted: surfaces indicating a planetary warming w

Deleted: indicating a strong planetary cooling.

Deleted: clear

Deleted: 13

Deleted: 9

Deleted: 2

Deleted: 6

Deleted: 43

Deleted: 4

Deleted: 6

Deleted: 3

Deleted: 3

Deleted: 9

Deleted: 3

Deleted: 8

Deleted: <#>For the regional clear-sky NET DREs at TOA, the calculated positive DREs (7.1 Wm⁻²) in the SDD and the negative DREs (-15 Wm⁻²) in the MSD at noon indicate a planetary warming and cooling in the Sahara and in the Mediterranean, respectively.¶
 <#>Over the 84 hours forecast period, the LW surface warming offsets by up to 37.7% the SW surface cooling whereas the LW atmospheric cooling offsets by 33.6% the SW atmospheric warming.¶
 <#>At TOA, the corresponding LW/SW ratios vary from 15.4% (MSD) to 52.9% (SDD); however, t

2292
 2293
 2294 **Sensible and latent heat fluxes**

- 2329 ➤ As a response to the surface radiation budget perturbations, desert dust outbreaks reduce the
2330 sensible heat fluxes (regional averages taking into account only land grid points) by up to 45 Wm^{-2}
2331 2 during daytime while reverse tendencies of lower magnitudes are found during night (2 Wm^{-2}).
2332 ➤ Locally, the aforementioned values can reach down to -150 Wm^{-2} and up to 50 Wm^{-2} .
2333 ➤ At noon, dust outbreaks reduce also the surface latent heat fluxes by up to 4 Wm^{-2} and 100 Wm^{-2}
2334 2 at a regional and grid point level, respectively. At night, the regional and the instantaneous LE
2335 levels are increased by up to 0.5 Wm^{-2} and 30 Wm^{-2} , respectively.
2336

2337 **Impact on temperature fields**

- 2338
2339 ➤ Due to the attenuation of the incoming solar radiation and the emission of radiation at thermal
2340 wavelengths, both induced by dust aerosols, temperature at 2 meters reduces and increases during
2341 day and night, respectively, by up to 4 K in absolute terms in land areas where the dust loads are
2342 intense (AODs higher than 2).
2343 ➤ At noon, dust outbreaks warm the atmosphere by up to 0.9 K between altitudes where elevated
2344 dust layers are located and cool the lowest tropospheric levels by up to 1.3 K, due to the reduced
2345 surface sensible heat fluxes.
2346 ➤ Due to the emission of LW radiation and the trapping of the outgoing terrestrial radiation by dust
2347 aerosols, the nocturnal temperature decreases by up to 0.8 K in atmospheric altitudes where
2348 mineral particles are confined, whereas between the bottom of the dust layer and the surface, the
2349 air-temperature increases by up to 1.2 K.
2350

2351 **Feedbacks on dust AOD and dust emission**

- 2352
2353 ➤ The total emitted amount of dust is reduced by 19.5% (statistically significant at 95% confidence
2354 level) over the forecast period when dust DREs are included into the numerical simulations,
2355 revealing thus a negative feedback on dust emissions.
2356 ➤ Among the studied cases, the corresponding percentages range from -34% (2 August 2012) to -
2357 10% (24 February 2006) and are statistical significant (95% confidence level) in all cases.
2358 ➤ As a consequence of the lower amount of mineral particles emitted in the atmosphere, negative
2359 feedbacks are also found on the mean regional dust $\text{AOD}_{550\text{nm}}$ which is decreased by 0.02 (6.9%)
2360 with respect to the control experiment (RADOFF).

Deleted: maximized

2362 ➤ Statistically significant reductions of the regional dust AOD_{550nm}, varying from 1% (22 February
2363 2004) to 12.5% (27 January 2005), are found in all the studied cases when dust-radiation
2364 interactions are activated (RADON).

2365

2366 Assessment of model's predictive skills

2367

2368 ➤ Through the evaluation of the model's forecast outputs of the SW and LW downwelling radiation
2369 at the ground against surface measurements derived by the BSRN network, it is revealed a
2370 reduction of the modelled positive (for SW) and negative (for LW) biases attributed to the
2371 consideration of dust radiative effects. However, model's accuracy is critically affected by its
2372 ability to represent satisfactorily aerosols' and clouds' spatiotemporal features, highlighting thus
2373 their key role when such comparisons are attempted.

2374 ➤ Under high dust load conditions (AODs higher/equal than 0.5), the nocturnal model-FNL
2375 negative regional biases of temperature at 2 meters are reduced by up to 0.5 K (95% statistically
2376 significant) in the RADON experiment. On the contrary, these temperature "corrections" are not
2377 evident during daytime revealing thus that other model errors (particularly those introduced by
2378 the soil model) can dominate over the expected improvements attributed to the consideration of
2379 dust-radiation interactions in the numerical simulations.

2380 ➤ The model regional warm biases found at 24 and 48 hours after the initialization of the forecast
2381 period, between pressure levels (950 and 700 hPa) where the dust concentration is maximized,
2382 are reduced by up to 0.4 K (95% statistically significant) in the RADON experiment.

2383 ➤ In general, the bias and RSME reductions achieved are relatively small. We recall that the model
2384 simulations show underestimation and spatiotemporal mismatches compared to MODIS. A future
2385 study may consider the potential benefit of AOD data assimilation in the model to better
2386 reproduce the magnitude and spatial features of the events and therefore to further improve the
2387 weather forecast itself.

2388

2389 Acknowledgments

2390

2391 The MDRAF project has received funding from the European Union's Seventh Framework Programme
2392 for research, technological development and demonstration under grant agreement no 622662. O. Jorba
2393 and S. Basart acknowledge the grant CGL2013-46736 and the AXA Research Fund. C. Pérez García-
2394 Pando acknowledges long-term support from the AXA Research Fund, as well as the support received

Deleted: downwelling

Deleted: for the SW and LW radiation, respectively,

Deleted: the

Deleted: highlighting

Deleted: of other model errors

Formatted: Font: Bold

2400 [through the Ramón y Cajal programme \(grant RYC-2015-18690\) and grant CGL2017-88911-R of the](#)
2401 [Spanish Ministry of Economy and Competitiveness. Simulations were performed with the Marenostrum](#)
2402 [Supercomputer at the Barcelona Supercomputing Center \(BSC\).](#) Simulations were performed with the
2403 Marenostrum Supercomputer at the Barcelona Supercomputing Center (BSC). We would like to thank
2404 the principal investigators maintaining the BSRN sites used in the present work. The authors would like
2405 thank the Arnon Karnieli for his effort in establishing and maintaining SEDE_BOKER_AERONET site.

2406 References

2407
2408
2409 Ahn, H. J., Park, S. U., and Chang, L. S.: Effect of direct radiative forcing of Asian dust on the
2410 meteorological fields in East Asia during an Asian dust event period, *J. Appl. Meteorol.*, 46, 1655–1681,
2411 doi:10.1175/JAM2551.1, 2007.

2412
2413 Albrecht, B. A.: Aerosols, cloud microphysics, and fractional cloudiness, *Science*, 245, 1227–1230,
2414 1989.

2415
2416 [Antón, M., Valenzuela, A., Cazorla, A., Gil, J. E., Fernández-Gálvez, J., Lyamani, H., Foyo-Moreno, I.,](#)
2417 [Olmo, F. J., and Alados-Arboledas, L.: Global and diffuse shortwave irradiance during a strong desert](#)
2418 [dust episode at Granada \(Spain\), *Atmos. Res.*, 118, 232–239, doi:10.1016/j.atmosres.2012.07.007, 2012.](#)

2419
2420 Antón, M., Valenzuela, A., Mateos, D., Alados, I., Foyo-Moreno, I., Olmo, F.J., Alados-Arboledas, L.:
2421 Longwave aerosol radiative effects during an extreme desert dust event in Southeastern Spain, *Atmos.*
2422 *Res.*, 148, 18–23, doi:10.1016/j.atmosres.2014.05.022, 2014.

2423
2424 Arakawa, A. and Lamb, V. R.: Computational design of the basic dynamical processes of the UCLA
2425 general circulation model, *Meth. Comput. Phys.*, 17, 173–265, 1977.

2426
2427 Badia, A., Jorba, O., Voulgarakis, A., Dabdub, D., Pérez García-Pando, C., Hilboll, A., Gonçalves, M.,
2428 and Janjic, Z.: Description and evaluation of the Multiscale Online Nonhydrostatic Atmosphere
2429 Chemistry model (NMMB-MONARCH) version 1.0: gas-phase chemistry at global scale, *Geosci.*
2430 *Model Dev.*, 10, 609–638, doi:10.5194/gmd-10-609-2017, 2017.

Deleted: C. Pérez García-Pando acknowledges long-term support from the AXA Research Fund, as well as the support received through the Ramón y Cajal programme (grant RYC-2015-18690) of the Spanish Ministry of Economy and Competitiveness.

Deleted: Alpert, P. and Ziv, B.: The Sharav Cyclone: Observations and some theoretical considerations, *J. Geophys. Res.*, 94, 18495–18514, doi:10.1029/JD094iD15p18495, 1989.¶
¶ Amiridis, V., Kafatos, M., Perez, C., Kazadzis, S., Gerasopoulos, E., Mamouri, R. E., Papayannis, A., Kokkalis, P., Giannakaki, E., Basart, S., Daglis, I., and Zerefos, C.: The potential of the synergistic use of passive and active remote sensing measurements for the validation of a regional dust model, *Ann. Geophys.*, 27, 3155–3164, doi:10.5194/angeo-27-3155-2009, 2009.¶
¶

2450 Banks, J. R., Brindley, H. E., Hobby, M., and Marsham, J. H.: The daytime cycle in dust aerosol direct
2451 radiative effects observed in the central Sahara during the Fennec campaign in June 2011, *J. Geophys.*
2452 *Res.-Atmos.*, 119, 13861–13876, doi:10.1002/2014JD022077, 2014.

2453

2454 Basart, S., Pérez, C., Cuevas, E., Baldasano, J. M., and Gobbi, G. P.: Aerosol characterization in Northern
2455 Africa, Northeastern Atlantic, Mediterranean Basin and Middle East from direct-sun AERONET
2456 observations, *Atmos. Chem. Phys.*, 9, 8265-8282, https://doi.org/10.5194/acp-9-8265-2009, 2009.

2457

2458 Bergstrom, R. W., Pilewskie, P., Russell, P. B., Redemann, J., Bond, T. C., Quinn, P. K., and Sierau, B.:
2459 Spectral absorption properties of atmospheric aerosols, *Atmos. Chem. Phys.*, 7, 5937-5943,
2460 doi:10.5194/acp-7-5937-2007, 2007.

2461

2462 Betts, A. K.: A new convective adjustment scheme. Part 1: Observational and theoretical basis, *Q. J.*
2463 *Roy. Meteor. Soc.*, 112, 677–691, doi:10.1002/qj.49711247307, 1986.

2464 Betts, A. K. and Miller, M. J.: A new convective adjustment scheme. Part 2: Single column tests using
2465 GATE wave, BOMEX, ATEX and arctic air-mass data sets, *Q. J. Roy. Meteor. Soc.*, 112, 693–709,
2466 doi:10.1002/qj.49711247308, 1986.

2467 Biniotoglou, I., Basart, S., Alados-Arboledas, L., Amiridis, V., Argyrouli, A., Baars, H., Baldasano, J.
2468 M., Balis, D., Belegante, L., Bravo-Aranda, J. A., Burlizzi, P., Carrasco, V., Chaikovsky, A., Comerón,
2469 A., D'Amico, G., Filioglou, M., Granados-Muñoz, M. J., Guerrero-Rascado, J. L., Ilic, L., Kokkalis, P.,
2470 Maurizi, A., Mona, L., Monti, F., Muñoz-Porcar, C., Nicolae, D., Papayannis, A., Pappalardo, G.,
2471 Pejanovic, G., Pereira, S. N., Perrone, M. R., Pietruczuk, A., Posyniak, M., Rocadenbosch, F., Rodríguez-
2472 Gómez, A., Sicard, M., Siomos, N., Szkop, A., Terradellas, E., Tsekeri, A., Vukovic, A., Wandinger, U.,
2473 and Wagner, J.: A methodology for investigating dust model performance using synergistic
2474 EARLINET/AERONET dust concentration retrievals, *Atmos. Meas. Tech.*, 8, 3577-3600,
2475 doi:10.5194/amt-8-3577-2015, 2015.

2476

2477 Boucher, O., Randall, D., Artaxo, P., Bretherton, C., Feingold, G., Forster, P., Kerminen, V.-M., Kondo,
2478 Y., Liao, H., Lohmann, U., Rasch, P., Satheesh, S.K., Sherwood, S., Stevens, B., and Zhang, X.Y.: Clouds
2479 and Aerosols. In: *Climate Change 2013: The Physical Science Basis. Contribution of Working Group I*
2480 *to the Fifth Assessment Report of the Intergovernmental Panel on Climate Change* [Stocker, T.F., D.

Deleted: Barkan, J., Alpert, P., Kutiel, H., and Kishcha, P.:
Synoptics of dusttransportation days from Africa toward Italy
and central Europe. *J. Geophys. Res.*, 110, D07208,
doi:10.1029/2004JD005222,2005.

¶

2486 Qin, G.-K. Plattner, M. Tignor, S.K. Allen, J. Boschung, A. Nauels, Y. Xia, V. Bex and P.M. Midgley
2487 (eds.)). Cambridge University Press, Cambridge, United Kingdom and New York, NY, USA, pp. 571–
2488 658, doi:10.1017/CBO9781107415324.016, 2013.

2489
2490 Chin, M., Ginoux, P., Kinne, S., Torres, O., Holben, B. N., Duncan, B. N., Martin, R. V., Logan, J. A.,
2491 Higurashi, A., and Nakajima, T.: Tropospheric aerosol optical thickness from the GOCART model and
2492 comparisons with satellite and Sun photometer measurements, J. Atmos. Sci., 59, 461–483,
2493 doi:10.1175/1520-0469(2002)059<0461:TAOTFT>2.0.CO, 2002.

2494 Choobari, O. A., Zawar-Reza, P., Sturman, A.: Feedback between wind blown dust and planetary
2495 boundary-layer characteristics: sensitivity to boundary and surface layer parameterizations. Atmos.
2496 Environ., 61,294–304,<http://dx.doi.org/10.1016/j.atmosenv.2012.07.038>, 2012.

2497
2498 Choobari, O. A., Zawar-Reza, P., and Sturman, A.: The global distribution of mineral dust and its impacts
2499 on the climate system: A review, Atmos. Res., 138, 152-165, doi:10.1016/j.atmosres.2013.11.007, 2014.

2500
2501 Christopher, S. A. and Jones, T. A.: Satellite-based assessment of cloud-free net radiative effect of dust
2502 aerosols over the Atlantic Ocean, Geophys. Res. Lett., 34, L02810, doi:10.1029/2006GL027783, 2007.

2503
2504 Cowie, S. M., Knippertz, P., and Marsham, J. H.: A climatology of dust emission events from northern
2505 Africa using long-term surface observations, Atmos. Chem. Phys., 14, 8579-8597, doi:10.5194/acp-14-
2506 8579-2014, 2014.

2507 Cuesta, J., Marsham, J. H., Parker, D. J., and Flamant, C.: Dynamical mechanisms controlling the vertical
2508 redistribution of dust and the thermodynamic structure of the West Saharan atmospheric boundary layer
2509 during summer, Atmos. Sci. Lett., 10, 34–42, doi:10.1002/Asl.207, 2009.

2510 Di Biagio, C., di Sarra, A., and Meloni, D.: Large atmospheric shortwave radiative forcing by
2511 Mediterranean aerosol derived from simultaneous ground-based and spaceborne observations, and
2512 dependence on the aerosol type and single scattering albedo, J. Geophys. Res., 115, D10209,
2513 doi:10.1029/2009JD012697, 2010.

Deleted: Carnevale, C., Finzi, G., Pisoni, E., Volta, M., Kishcha, P., and Alpert, P.: Integrating Saharan dust forecasts into a regional chemical transport model: a case study over Northern Italy, Sci.Total Environ., 417–418, 224–231, 2012.¶

Deleted: Colarco, P. R., Nowottnick, E. P., Randles, C. A., Yi, B., Yang, P., Kim, K.-M., Smith, J. A., and Bardeen, C. G.: Impact of radiatively interactive dust aerosols in the NASAGEOS-5 climate model: Sensitivity to dust particle shape and refractive index, J. Geophys. Res.-Atmos., 119, 753–786, doi:10.1002/2013JD020046, 2014.

Deleted: DeSouza-Machado, S. G., Strow, L. L., Imbiriba, B., McCann, K., Hoff, R. M., Hannon, S. E., Martins, J. V., Tanré, D., Deuzé, J. L., Ducos, F., and Torres, O.: Infrared retrievals of dust using AIRS: Comparisons of optical depths and heights derived for a North African dust storm to other collocated EOS ATrain and surface observations, J. Geophys. Res., 115, D15201, doi:10.1029/2009JD012842, 2010.¶

Deleted: simultaneous

2533 Di Sarra, A., Pace, G., Meloni, D., De Silvestri, L., Piacentino, S., and Monteleone, F.: Surface shortwave
2534 radiative forcing of different aerosol types in the central Mediterranean, *Geophys. Res. Lett.*, 35, L02714,
2535 doi:10.1029/2007GL032395, 2008.

2536 Di Sarra, A., di Biagio, C., Meloni, D., Monteleone, F., Pace, G., Pugnaghi, S., and Sferlazzo, D.:
2537 Shortwave and longwave radiative effects of the intense Saharan dust event of 25–26 March 2010
2538 at Lampedusa (Mediterranean Sea), *J. Geophys. Res.*, 116, D23209, doi:10.1029/2011JD016238, 2011.

2539 Di Sarra, A., Fuà, D., and Meloni, D.: Estimate of surface direct radiative forcing of desert dust from
2540 atmospheric modulation of the aerosol optical depth, *Atmos. Chem. Phys.*, 13, 5647–5654,
2541 doi:10.5194/acp-13-5647-2013, 2013.

2542 Di Tomaso, E., Schutgens, N. A. J., Jorba, O., and Pérez García-Pando, C.: Assimilation of MODIS Dark
2543 Target and Deep Blue observations in the dust aerosol component of NMMB-MONARCH version 1.0,
2544 *Geosci. Model Dev.*, 10, 1107–1129, doi:10.5194/gmd-10-1107-2017, 2017.

2545

2546 Ek, M. B., Mitchell, K. E., Lin, Y., Rogers, E., Grunmann, P., Koren, V., Gayno, G., and Tarpley, J. D.:
2547 Implementation of Noah land surface model advances in the National Centers for Environmental
2548 Prediction operational mesoscale Eta model, *J. Geophys. Res.*, 108, 8851, doi:10.1029/2002JD003296,
2549 2003.

2550 Ferrier, B. S., Jin, Y., Lin, Y., Black, T., Rogers, E., and DiMego, G.: Implementation of a new grid-
2551 scale cloud and precipitation scheme in the NCEP Eta Model, in: *Proc. 15th Conf. on Numerical Weather
2552 Prediction*, 12–16 August 2002, San Antonio, TX, Amer. Meteor. Soc., pp. 280–283, 2002.

2553 Foltz, G. R. and McPhaden, M. J.: Impact of Saharan dust on tropical North Atlantic SST, *J. Climate*,
2554 21, 5048–5060, 2008.

2555 Gama, C., Tchepel, O., Baldasano, J. M., Basart, S., Ferreira, J., Pio, C., Cardoso, J., and Borrego, C.:
2556 Seasonal patterns of Saharan dust over Cape Verde—a combined approach using observations and
2557 modelling, *Tellus B*, 67, 24410, doi:10.3402/tellusb.v67.24410, 2015.

2558 Ginoux, P., Prospero, J. M., Gill, T. E., Hsu, N. C., and Zhao, M.: Global-scale attribution of
2559 anthropogenic and natural dust sources and their emission rates based on MODIS Deep Blue aerosol
2560 products, *Rev. Geophys.*, 50, RG3005, doi:10.1029/2012rg000388, 2012.

Deleted:

Deleted: -

2563 Gkikas, A., Hatzianastassiou, N., Mihalopoulos, N., Katsoulis, V., Kazadzis, S., Pey, J., Querol, X., and
2564 Torres, O.: The regime of intense desert dust episodes in the Mediterranean based on contemporary
2565 satellite observations and ground measurements, *Atmos. Chem. Phys.*, 13, 12135-12154,
2566 doi:10.5194/acp-13-12135-2013, 2013.

2567

2568 Gkikas, A., Houssos, E. E., Lolis, C. J., Bartzokas, A., Mihalopoulos, N. and Hatzianastassiou, N.:
2569 Atmospheric circulation evolution related to desert-dust episodes over the Mediterranean. *Q.J.R.*
2570 *Meteorol. Soc.*, 141: 1634–1645. doi: 10.1002/qj.2466, 2015.

2571

2572 Gkikas, A., Basart, S., Hatzianastassiou, N., Marinou, E., Amiridis, V., Kazadzis, S., Pey, J., Querol, X.,
2573 Jorba, O., Gassó, S., and Baldasano, J. M.: Mediterranean intense desert dust outbreaks and their vertical
2574 structure based on remote sensing data, *Atmos. Chem. Phys.*, 16, 8609-8642, doi:10.5194/acp-16-8609-
2575 2016, 2016.

2576

2577 Gómez-Amo, J. L., Pinti, V., Di Iorio, T., di Sarra, A., Meloni, D., Becagli, S., Bellantone, V., Cacciani,
2578 M., Fuà, D., and Perrone, M. R.: The June 2007 Saharan dust event in the central Mediterranean:
2579 Observations and radiative effects in marine, urban, and sub-urban environments, *Atmos. Environ.*, 45,
2580 5385–5493, 2011.

2581

2582 Guerrero-Rascado, J. L., Olmo, F. J., Avilés-Rodríguez, I., Navas-Guzmán, F., Pérez-Ramírez, D.,
2583 Lyamani, H., and Alados Arboledas, L.: Extreme Saharan dust event over the southern Iberian Peninsula
2584 in september 2007: active and passive remote sensing from surface and satellite, *Atmos. Chem. Phys.*, 9,
2585 8453-8469, doi:10.5194/acp-9-8453-2009, 2009.

2586

2587 Hansen, J., Sato, M., and Ruedy, R.: Radiative forcing and climate response, *J. Geophys. Res.*, 102,
2588 6831–6864, 1997.

2589

2590 Hatzianastassiou, N., Katsoulis, B., and Vardavas, I.: Sensitivity analysis of aerosol direct radiative
2591 forcings in the ultraviolet – visible wavelengths and consequences for the heat budget, *Tellus*, 56B, 368–
2592 381, 2004.

2593

2594 Haustein, K., Pérez, C., Baldasano, J. M., Jorba, O., Basart, S., Miller, R. L., Janjic, Z., Black, T.,
2595 Nickovic, S., Todd, M. C., Washington, R., Müller, D., Tesche, M., Weinzierl, B., Esselborn, M., and
2596 Schladitz, A.: Atmospheric dust modeling from meso to global scales with the online NMMB/BSC-Dust
2597 model – Part 2: Experimental campaigns in Northern Africa, *Atmos. Chem. Phys.*, 12, 2933-2958,
2598 doi:10.5194/acp-12-2933-2012, 2012.

2599

2600 Haywood, J., Allan, R., Culverwell, I., Slingo, T., Milton, S., Edwards, J., and Clerbaux, N.: Can desert
2601 dust explain the outgoing longwave radiation anomaly over the Sahara during July 2003? *J. Geophys.*
2602 *Res.*, 110, D05105, doi:10.1029/2004JD005232, 2005.

2603

2604 Heinold, B., Tegen, I., Schepanski, K., and Hellmuth, O.: Dust Radiative feedback on Saharan boundary
2605 layer dynamics and dust mobilization. *Geophys. Res. Lett.*, 35, L20817, doi:10.1029/2008GL035319,
2606 2008.

2607

2608 Helmert, J., Heinold, B., Tegen, I., Hellmuth, O., and Wendisch, M.: On the direct and semi-direct effect
2609 of Saharan dust over Europe: a modeling study, *J. Geophys. Res.*, 112, D11204,
2610 doi:10.1029/2006JD007444, 2007.

2611

2612 Huang, J., Wang, T., Wang, W., Li, Z., and Yan, H.: Climate effects of dust aerosols over East Asian
2613 arid and semi-arid regions, *J. Geophys. Res.*, 119, 11398–11416, doi:10.1002/2014JD021796, 2014.

2614

2615 Huneus, N., Basart, S., Fiedler, S., Morcrette, J.-J., Benedetti, A., Mulcahy, J., Terradellas, E., Pérez
2616 García-Pando, C., Pejanovic, G., Nickovic, S., Arsenovic, P., Schulz, M., Cuevas, E., Baldasano, J. M.,
2617 Pey, J., Remy, S., and Cvetkovic, B.: Forecasting the northern African dust outbreak towards Europe in
2618 April 2011: a model intercomparison, *Atmos. Chem. Phys.*, 16, 4967-4986, doi:10.5194/acp-16-4967-
2619 2016, 2016.

2620

2621 Iacono, M. J., Delamere, J. S., Mlawer, E. J., Shephard, M.W., Clough, S. A., and Collins, W. D.:
2622 Radiative forcing by long-lived greenhouse gases: Calculations with the AER Radiative transfer models,
2623 *J. Geophys. Res.*, 113, D13103, doi:10.1029/2008JD009944, 2008.

2624

Deleted: Heald, C. L., Ridley, D. A., Kroll, J. H., Barrett, S. R. H., Cady-Pereira, K. E., Alvarado, M. J., and Holmes, C. D.: Contrasting the direct radiative effect and direct radiative forcing of aerosols, *Atmos. Chem. Phys.*, 14, 5513-5527, doi:10.5194/acp-14-5513-2014, 2014.

2631 IPCC, 2013: *Climate Change 2013: The Physical Science Basis. Contribution of Working Group I to the*
2632 *Fifth Assessment Report of the Intergovernmental Panel on Climate Change* [Stocker, T.F., D. Qin, G.-
2633 K. Plattner, M. Tignor, S.K. Allen, J. Boschung, A. Nauels, Y. Xia, V. Bex and P.M. Midgley (eds.)].
2634 Cambridge University Press, Cambridge, United Kingdom and New York, NY, USA, 1535 pp,
2635 doi:10.1017/CBO9781107415324.

2636 Janjic, Z. I.: The step-mountain eta coordinate model: further developments of the convection, viscous
2637 sublayer, and turbulence closure schemes, *Mon. Weather Rev.*, 122, 927–945, doi:10.1175/1520-
2638 0493(1994)122<0927:TSMECM>2.0.CO;2, 1994.

Deleted: -

2639 Janjic, Z. I.: Comments on “Development and evaluation of a convection scheme for use in climate
2640 models”, *J. Atmos. Sci.*, 57, 3686–3686, doi:10.1175/1520- 0469(2000)057<3686:CODAEO>2.0.CO;2,
2641 2000.

Deleted: -

Deleted: -

2642 Janjic, Z. I., Gerrity, J. P., and Nickovic, S.: An alternative approach to non_hydrostatic modeling, *Mon.*
2643 *Weather Rev.*, 129, 1164–1178, doi:10.1175/1520- 0493(2001)129.0.CO;2, 2001.

2644

2645 Janjic, Z. I.: A non_hydrostatic model based on a new approach, *Meteorol. Atmos. Phys.*, 82, 271–285,
2646 doi:10.1007/s00703-001- 0587-6, 2003.

2647

2648 Janjic, Z. I.: A unified model approach from meso to global scales, *Geophys. Res. Abstr.*, 7, SRef-ID:
2649 1607–7962/gra/EGU05–A– 05582, 2005.

2650

2651 Janjic, Z. I. and Black, T.: A unified model approach from meso to global scales, *Geophys. Res. Abstr.*,
2652 9, SRef-ID: 1607–7962/gra/EGU2007–A–05025, 2007.

2653

2654 Janjic, Z.: Further development of the unified multiscale Eulerian model for a broad range of spatial and
2655 temporal scales within the new National Environmental Modeling System, EGU General Assembly
2656 2009, held 19–24 April 2009, Vienna, Austria, abstract #EGU2009-1587, 11, p. 1587, 2009.

2657

2658 Janjic, Z., Janjic, T., and Vasic, R.: A Class of conservative fourth order advection schemes and impact
2659 of enhanced formal accuracy on extended range forecasts, *Mon. Weather Rev.*, 0, null,
2660 doi:10.1175/2010MWR3448.1, 2011.

2664

2665 Ji, Z., Wang, G., Pal, J.S., Yu, M.: Potential climate effect of mineral aerosols over West_Africa. Part I:
2666 model validation and contemporary climate evaluation. *Clim. Dyn.*, 1–17, doi: 10.1007/s00382-015-
2667 2641-y, 2015.

2668

2669 Kalenderski, S. and Stenchikov, G.: High-resolution regional modeling of summertime transport and
2670 impact of African dust over the Red Sea and Arabian Peninsula, *J. Geophys. Res.*, 121, 6435-6458, doi:
2671 10.1002/2015JD024480, 2016.

2672 [Koepke, P., Hess, M., Schult, I., and Shettle, E. P.: Global aerosol data set. Tech. rep., Max-Planck
2673 Institut für Meteorologie, Hamburg, Germany, 1997.](#)

2674 Kubilay, N., Cokacar, T., and Oguz, T.: Optical properties of mineral dust outbreaks over the northeastern
2675 Mediterranean, *J. Geophys. Res.*, 108(D21), 4666, doi:10.1029/2003JD003798, 2003.

2676 Kumar, R., Barth, M. C., Pfister, G. G., Naja, M., and Brasseur, G. P.: WRF-Chem simulations of a
2677 typical pre-monsoon dust storm in northern India: influences on aerosol optical properties and radiation
2678 budget, *Atmos. Chem. Phys.*, 14, 2431–2446, doi:10.5194/acp-14-2431-2014, 2014.

2679 Lelieveld, J., Berresheim, H., Borrmann, S., et al.: Global air pollution crossroads over the
2680 Mediterranean, *Science*, 298, 794–799, 2002.

2681 Liao, H. and Seinfeld, J.: Radiative forcing by mineral dust aerosols: sensitivity to key variables, *J.*
2682 *Geophys. Res.*, 103, 31637–31645, 1998.

2683 Ling, X., Guo, W., and Fu, C.: Composite analysis of impacts of dust aerosols on surface atmospheric
2684 variables and energy budgets in a semiarid region of China, *J. Geophys. Res. Atmos.*, 119, 3107–3123,
2685 doi:10.1002/2013jd020274, 2014.

2686 Lohmann, U. and Feichter, J.: Global indirect aerosol effects: a review, *Atmos. Chem. Phys.*, 5, 715-737,
2687 doi:10.5194/acp-5-715-2005, 2005.

2688 Mahowald, N. M., Albani, S., Kok, J. F., Engelstaedter, S., Scanza, R., Ward, D. S., and Flanner, M. G.:
2689 The size distribution of desert dust aerosols and its impact on the Earth system, *Aeol. Res.*, 15, 53–71,
2690 doi:10.1016/j.aeolia.2013.09.002, 2014.

Deleted: Kanakidou, M., Mihalopoulos, N., Kalivitis, N., Tsigaridis, K., Kouvarakis, G., Koulouri, E., Gerasopoulos, E., Vrekoussis, M., and Myriokefalitakis, S.: Natural contributions to particulate matter levels over Europe – the experience from Greece, *International Conference on Science and Technology (CEST) 2007*, A-585-592, 2007.

2697 Mallet, M., Tulet, P., Serça, D., Solmon, F., Dubovik, O., Pelon, J., Pont, V., and Thouron, O.: Impact
2698 of dust aerosols on the radiative budget, surface heat fluxes, heating rate profiles and convective activity
2699 over West Africa during March 2006, *Atmos. Chem. Phys.*, 9, 7143-7160, doi:10.5194/acp-9-7143-2009,
2700 2009.

2701 Marcella, M.P., Eltahir, E.A.B.: The role of mineral aerosols in shaping the regional climate of West
2702 Africa. *J. Geophys. Res., Atmospheres*, 119, 1-14, doi:10.1002/2012JD019394, 2014.

2703

2704 Marti, A., Folch, A., Jorba, O., and Janjic, Z.: Volcanic ash modeling with the online NMMB-
2705 MONARCH-ASH v1.0 model: model description, case simulation, and evaluation, *Atmos. Chem. Phys.*,
2706 17, 4005-4030, doi:10.5194/acp-17-4005-2017, 2017.

2707

2708 McPeters, R.D., Bhartia, P. K., Krueger, A. J., Torres, O. and Herman, J. R.: Earth Probe Total Ozone
2709 Mapping Spectrometer (TOMS) Data Products User's Guide; NASA Technical Publication 1998-
2710 206895, 1998.

2711

2712 Meloni, D., di Sarra, A., Di Iorio, T., and Fiocco, G.: Direct radiative forcing of Saharan dust in the
2713 Mediterranean from measurements at Lampedusa island and MISR space-borne observations, *J.*
2714 *Geophys. Res.*, 109(D8), D08206, doi:10.1029/2003JD003960, 2004.

2715

2716 Meloni, D., Junkermann, W., di Sarra, A., Cacciani, M., De Silvestri, L., Di Iorio, T., Estellés, V.,
2717 Gómez-Amo, J. L., Pace, G., and Sferlazzo, D. M.: Altitude-resolved shortwave and longwave radiative
2718 effects of desert dust in the Mediterranean during the GAMARF campaign: Indications of a net daily
2719 cooling in the dust layer, *J. Geophys. Res.*, 120, 3386–3407, doi:10.1002/2014JD022312, 2015.

2720

2721 Meyer, K., Platnick, S., Oreopoulos, L., and Lee, D.: Estimating the direct radiative effect of absorbing
2722 aerosols overlying marine boundary layer clouds in the southeast Atlantic using MODIS and CALIOP,
2723 *J. Geophys. Res.-Atmos.*, 118, 4801–4815, doi:10.1002/jgrd.50449, 2013.

2724

2725 Miller, R. L. and Tegen, I.: Climate response to soil dust aerosols, *J. Climate*, 11, 3247–3267, 1998.

2726

Deleted: Meloni, D., di Sarra, A., Monteleone, F., Pace, G., Piacentino, S., and Sferlazzo, D.: Seasonal transport patterns of intense Saharan dust events at the Mediterranean island of Lampedusa, *Atmos. Res.*, 88, 134–148, doi:10.1016/j.atmosres.2007.10.007, 2008. ¶

2733 Miller, R. L., Perlwitz, J., and Tegen, I.: Feedback upon dust emission by dust radiative forcing through
2734 the planetary boundary layer, *J. Geophys. Res.*, 109, D24209, doi:10.1029/2004JD004912, 2004a.

2735

2736 Miller, R. L., Tegen, I., and Perlwitz, J.: Surface radiative forcing by soil dust aerosols and the hydrologic
2737 cycle, *J. Geophys. Res.*, 109(D4), D04203, doi:10.1029/2003JD004085, 2004b.

2738

2739 Mischenko, M., Travis, L. D., and Lacis, A. A.: Scattering, absorption and emission of light by small
2740 particles, Cambridge University Press, Cambridge, 2002.

2741

2742 Mishra, A.K., Koren, I., Rudich, Y.: Effect of aerosol vertical distribution on aerosol-radiation
2743 interaction: a theoretical prospect. *Heliyon* 1, e00036. <http://dx.doi.org/10.1016/j.heliyon.2015.e00036>,
2744 2015.

2745

2746 Mlawer, E. J., Taubman, S. J., Brown, P. D., Iacono, M. J., and Clough, S. A.: Radiative transfer for
2747 inhomogeneous atmospheres: RRTM, a validated correlated-k model for the longwave, *J. Geophys. Res.*,
2748 102, 16663–16682, doi:10.1029/97JD00237, 1997.

2749

2750 Monin, A. S. and Obukhov, A. M.: Osnovnye zakonomernosti turbulentnogo peremesivaniya v
2751 prizemnom sloe atmosfery, *Trudy geofiz. inst. AN SSSR*, 24, 163–187, 1954.

Formatted: Font: (Default) Times New Roman, 12 pt, No underline, Font color: Auto

2752 Moulin, C., Lambert, C. E., Dayan, U., Masson, V., Ramonet, M., Bousquet, P., Legrand, M., Balkanski,
2753 Y. J., Guelle, W., Martıcorena, B., Bergametti, G., and Dulac, F.: Satellite climatology of African dust
2754 transport in the Mediterranean atmosphere, *J. Geo- phys. Res.*, 103, 13137, doi:10.1029/98JD00171,
2755 1998.

Deleted: -

2756 Müller, T., Schladitz, A., Massling, A., Kaaden, N., Kandler, K., and Wiedensohler, A.: Spectral
2757 absorption coefficients and imaginary parts of refractive indices of Saharan dust during SAMUM-
2758 1, *Tellus B*, 61, 79–95, 2009.

2759

2760 Nabat, P., Solmon, F., Mallet, M., Kok, J. F., and Somot, S.: Dust emission size distribution impact on
2761 aerosol budget and radiative forcing over the Mediterranean region: a regional climate model approach,
2762 *Atmos. Chem. Phys.*, 12, 10545-10567, doi:10.5194/acp-12-10545-2012, 2012.

2763

2765 Nabat, P., Somot, S., Mallet, M., Sevault, F., Chiacchio, M., and Wild, M.: Direct and semi-direct aerosol
2766 radiative effect on the Mediterranean climate variability using a Regional Climate System Model, *Clim.*
2767 *Dynam.*, 44, 1127–1155, doi:10.1007/s00382-014-2205-6, 2015a.
2768
2769 Nabat, P., Somot, S., Mallet, M., Michou, M., Sevault, F., Driouech, F., Meloni, D., di Sarra, A., Di
2770 Biagio, C., Formenti, P., Sicard, M., Léon, J.-F., and Bouin, M.-N.: Dust aerosol radiative effects during
2771 summer 2012 simulated with a coupled regional aerosol–atmosphere–ocean model over the
2772 Mediterranean, *Atmos. Chem. Phys.*, 15, 3303–3326, doi:10.5194/acp-15-3303-2015, 2015b.
2773
2774 Obregón, M.A., Pereira, S., Salgueiro, V., Costa, M.J., Silva, A.M., Serrano, A., Bortoli, D.: Aerosol
2775 radiative effects during two desert dust events in August 2012 over the Southwestern Iberian Peninsula,
2776 *Atmos. Res.*, 153, 404–415, doi:10.1016/j.atmosres.2014.10.007, 2015.
2777
2778 Ohmura, A., Gilgen, H., Hegner, H., Müller, G., Wild, M., Dutton, E. G., Forgan, B., Fröhlich, C.,
2779 Philipona, R., Heimo, A., and König-Langlo, G.: Baseline Surface Radiation Network (BSRN/WCRP):
2780 New precision radiometry for climate research, *B. Am. Meteorol. Soc.*, 79, 2115–2136, 1998.
2781
2782 O’Neill, N. T., Eck, T. F., Smirnov, A., Holben, B. N., and Thulasiraman, S.: Spectral discrimination of
2783 coarse and fine mode optical depth, *J. Geophys. Res.*, 108, 4559, doi:10.1029/2002JD002975, 2003.
2784
2785 Oreopoulos, L., and Barker, H. W.: Accounting for subgrid-scale cloud variability in a multi-layer 1-D
2786 solar radiative transfer algorithm, *Q. J. R. Meteorol. Soc.*, 125, 301–330, 1999.
2787
2788 Osborne, S., Baran, A., Johnson, B., Haywood, J., Hesse, E., and Newman, S.: Short-wave and long-
2789 wave radiative properties of Saharan dust aerosol, *Q. J. Roy. Meteorol. Soc.*, 137, 1149–1167, 2011.
2790
2791 Osipov, S., Stenchikov, G., Brindley, H., and Banks, J.: Diurnal cycle of the dust instantaneous direct
2792 radiative forcing over the Arabian Peninsula, *Atmos. Chem. Phys.*, 15, 9537–9553, doi:10.5194/acp-15-
2793 9537-2015, 2015.
2794
2795 Otto, S., de Reus, M., Trautmann, T., Thomas, A., Wendisch, M., and Borrmann, S.: Atmospheric
2796 radiative effects of an in situ measured Saharan dust plume and the role of large particles, *Atmos. Chem.*
Phys., 7, 4887–4903, doi:10.5194/acp-7-4887-2007, 2007.

Deleted: Nastos, P. T.: Meteorological Patterns Associated with Intense Saharan Dust Outbreaks over Greece in Winter, *Adv. Meteorol.*, 2012, 828301, 17 pp., 2012.¶

2801
2802 Papadimas, C. D., Hatzianastassiou, N., Matsoukas, C., Kanakidou, M., Mihalopoulos, N., and Vardavas,
2803 I.: The direct effect of aerosols on solar radiation over the broader Mediterranean basin, *Atmos. Chem.*
2804 *Phys.*, 12, 7165-7185, doi:10.5194/acp-12-7165-2012, 2012.

2805
2806 Pérez, C., Nickovic, S., Pejanovic, G., Baldasano, J. M., and Özsoy, E.: Interactive dust-radiation
2807 modeling: A step to improve weather forecasts, *J. Geophys. Res.*, 111, 1–17, 2006.

2808
2809 Pérez, C., Haustein, K., Janjic, Z., Jorba, O., Huneeus, N., Baldasano, J. M., Black, T., Basart, S.,
2810 Nickovic, S., Miller, R. L., Perlwitz, J. P., Schulz, M., and Thomson, M.: Atmospheric dust modeling
2811 from meso to global scales with the online NMMB/BSC-Dust model – Part 1: Model description, annual
2812 simulations and evaluation, *Atmos. Chem. Phys.*, 11, 13001-13027, doi:10.5194/acp-11-13001-2011,
2813 2011.

2814
2815 Perlwitz, J., Tegen, I., and Miller, R.: Interactive soil dust aerosol model in the GISS GCM 1. Sensitivity
2816 of the soil dust cycle to radiative properties of soil dust aerosols, *J. Geophys. Res.*, 106, 18167–18192,
2817 2001.

2818
2819 Petzold, A., Rasp, K., Weinzierl, B., Esselborn, M., Hamburger, T., Dörnbrack, A., Kandler, K., Schütz,
2820 L., Knippertz, P., Fiebig, M., and Virkkula, A.: Saharan dust refractive index and optical properties from
2821 aircraft-based observations during SAMUM 2006, *Tellus B*, 61 118–130, 2009.

2822
2823 Pey, J., Querol, X., Alastuey, A., Forastiere, F., and Stafoggia, M.: African dust outbreaks over the
2824 Mediterranean Basin during 2001–2011: PM10 concentrations, phenomenology and trends, and its
2825 relation with synoptic and mesoscale meteorology, *Atmos. Chem. Phys.*, 13, 1395–1410, doi:
2826 10.5194/acp-13-1395-2013, 2013.

2827
2828 Pincus, R., and Baker, M.: Precipitation, solar absorption and albedo susceptibility in marine boundary
2829 layer clouds, *Nature*, 372, 250–252, 1994.

2830
2831 Querol, X., Pey, J., Pandolfi, M., Alastuey, A., Cusack, M., Pérez, N., Moreno, T., Viana, N.,
2832 Mihalopoulos, N., Kallos, G. and Kleanthous, S.: African dust contributions to mean ambient PM10

Deleted: c

2898 Scarnato, B. V., China, S., Nielsen, K., and Mazzoleni, C.: Perturbations of the optical properties of
2899 mineral dust particles by mixing with black carbon: a numerical simulation study, *Atmos. Chem. Phys.*,
2900 15, 6913-6928, doi:10.5194/acp-15-6913-2015, 2015.

2901

2902 Schepanski, K., Tegen, I., Todd, M. C., Heinold, B., Bönisch, G., Laurent, B., and Macke, A.:
2903 Meteorological processes forcing Saharan dust emission inferred from MSG-SEVIRI observations of
2904 subdaily dust source activation and numerical models, *J. Geophys. Res.*, 114, D10201,
2905 doi:10.1029/2008jd010325, 2009.

2906 Seigel, R. B., van den Heever, S. C., and Saleeby, S. M.: Mineral dust indirect effects and cloud radiative
2907 feedbacks of a simulated idealized nocturnal squall line, *Atmos. Chem. Phys.*, 13, 4467-4485,
2908 doi:10.5194/acp-13-4467-2013, 2013.

2909

2910 Sicard, M., Bertolín, S., Mallet, M., Dubuisson, P., and Comerón, A.: Estimation of mineral dust long-
2911 wave radiative forcing: sensitivity study to particle properties and application to real cases in the region
2912 of Barcelona, *Atmos. Chem. Phys.*, 14, 9213–9231, doi:10.5194/acp-14-9213-2014, 2014a.

2913

2914 Sicard, M., Bertolín, S., Muñoz, C., Rodríguez, A., Rocadenbosch, F. and Comerón, A.: Separation of
2915 aerosol fine- and coarse-mode radiative properties: Effect on the mineral dust longwave, direct radiative
2916 forcing, *Geophys. Res. Lett.*, 41, 6978–6985, doi:10.1002/2014GL060946, 2014.

2917

2918 Simmons, A. J. and Burridge, D. M.: An energy and angular momentum conserving vertical finite-
2919 difference scheme and hybrid vertical coordinates, *Mon. Weather Rev.*, 109, 758–766,
2920 doi:10.1175/1520-0493(1981)1092.0.CO;2, 1981.

2921

2922 Singh, S. and Beegum, S.N.: Direct radiative effects of an unseasonal dust storm at a western Indo
2923 Gangetic Plain station Delhi in ultraviolet, shortwave, and longwave regions, *Geophys. Res. Lett.*, 40,
2924 2444-2449, doi: 10.1002/grl.50496, 2013.

2925

2926 Sinyuk, A., Torres, O., and Dubovik, O.: Combined use of satellite and surface observations to infer the
2927 imaginary part of refractive index of Saharan dust, *Geophys. Res. Lett.*, 30, 1081,
2928 doi:10.1029/2002GL016189, 2003.

2929

2930 Sokolik, I. N., Winker, D., Bergametti, G., et al.: Introduction to special section: outstanding problems
2931 in quantifying the radiative impacts of mineral dust, *J. Geophys. Res.*, 106, 18 015–18 027, 2001.
2932
2933 Solmon, F., Mallet, M., Elguindi, N., Giorgi, F., Zakey, A., and Konare, A.: Dust aerosol impact on
2934 regional precipitation over Western Africa, mechanisms and sensitivity to absorption properties,
2935 *Geophys. Res. Lett.*, 35, 124705, doi:10.1029/2008GL035900, 2008.
2936
2937 Solmon, F., Elguindi, N., and Mallet, M.: Radiative and climatic effects of dust over West Africa, as
2938 simulated by a regional climate model, *Clim. Res.*, 2, 97–113, 2012.
2939
2940 Spyrou, C., Kallos, G., Mitsakou, C., Athanasiadis, P., Kalogeri, C., and Iacono, M. J.: Modeling the
2941 radiative effects of desert dust on weather and regional climate, *Atmos. Chem. Phys.*, 13, 5489–5504,
2942 doi:10.5194/acp-13-5489-2013, 2013.
2943
2944 Stanelle, T., Vogel, B., Vogel, H., Bäumer, D., and Kottmeier, C.: Feedback between dust particles and
2945 atmospheric processes over West Africa during dust episodes in March 2006 and June 2007, *Atmos.*
2946 *Chem. Phys.*, 10, 10771–10788, doi:10.5194/acp-10-10771-2010, 2010.
2947
2948 Tegen, I., Bierwirth, E., Heinold, B., Helmert, J., and Wendisch, M.: Effect of measured surface albedo
2949 on modeled Saharan dust solar radiative forcing, *J. Geophys. Res.*, 115, D24312,
2950 doi:10.1029/2009JD013764, 2010.
2951
2952 Toledano, C., Cachorro, V. E., de Frutos, A. M., Sorribas, M., Prats, N., and de la Morena, B. A.:
2953 Inventory of African desert dust events over the southwestern Iberian Peninsula in 2000–2005 with an
2954 AERONET Cimel Sun photometer, *J. Geophys. Res.*, 112, D21201, doi:10.1029/2006JD008307, 2007.
2955
2956 Torres, O., Bhartia P. K., Herman J. R., Ahmad Z., and Gleason, J.: Derivation of aerosol properties
2957 from satellite measurements of backscattered ultraviolet radiation: Theoretical bases. *J. Geophys. Res.*,
2958 103, 17 009–17 110, 1998.
2959

Deleted: Theodosi, C., Markaki, Z., and Mihalopoulos, N.:
Iron speciation, solubility and temporal variability in wet and
dry deposition in the Eastern Mediterranean, *Marine Chem.*,
120, 100–107, 2010.¶

2965 Torres, O., Tanskanen, A., Veihelman, B., Ahn, C., Braak, R., Bhartia, P. K., Veeffkind, P., and Levelt,
 2966 P.: Aerosols and Surface UV Products from OMI Observations: an overview, *J. Geophys. Res.*, 112,
 2967 D24S47, doi:10.1029/2007JD008809, 2007.

2968

2969 Twomey, S.: Pollution and the planetary albedo, *Atmos. Environ.*, 8, 1251–1256, 1974.

2970

2971 Valenzuela, A., Olmo, F. J., Lyamani, H., Antón, M., Quirantes, A., and Alados-Arboledas, L.: Aerosol
 2972 radiative forcing during African desert dust events (2005–2010) over Southeastern Spain, *Atmos. Chem.
 2973 Phys.*, 12, 10331–10351, doi:10.5194/acp-12-10331-2012, 2012.

2974

2975 Vinoj, V., Rasch, P. J., Wang, H., Yoon, J.-H., Ma, P.-L., Landu, K., and Singh, B.: Short-term
 2976 modulation of Indian summer monsoon rainfall by West Asian dust, *Nat. Geosci.*, 7, 308–313,
 2977 doi:10.1038/NGEO2107, 2014.

2978

2979 Wang, H., Zhang, X. Y., Gong, S. L., Chen, Y., Shi, G. Y., and Li, W.: Radiative feedback of dust aerosols
 2980 on the East Asian dust storms, *J. Geophys. Res.*, 115, D23214, doi:23210.21029/22009JD013430, 2010.

2981

2982 Wang, H., Zhao, T. L., Zhang, X. Y., and Gong, S. L.: Dust direct radiative effects on the earth-
 2983 atmosphere system over east Asia: Early spring cooling and late spring warming, *Chinese Sci. Bull.*, 56,
 2984 1020–1030, doi:10.1007/s11434-011-4405-3, 2011.

2985

2986 Wang, H. and Niu, T.: Sensitivity studies of aerosol data assimilation and direct radiative feedbacks in
 2987 modeling dust aerosols, *Atmos. Environ.*, 64, 208–218, doi:10.1016/j.atmosenv.2012.09.066, 2013.

2988

2989 Wang, Z. L., Zhang, H., Jing, X. W., and Wei, X. D.: Effect of non-spherical dust aerosol on its direct
 2990 radiative forcing, *Atmos. Res.*, 120, 112–126, doi:10.1016/j.atmosres.2012.08.006, 2013.

2991

2992 Wang, H., Shi, G. Y., Zhu, J., Chen, B., Che, H., and Zhao, T. L.: Case study of longwave contribution
 2993 to dust radiative effects over East Asia, *Chin. Sci. Bull.*, 30, 3673–3681, doi:10.1007/s11434-013-5752-
 2994 z, 2013.

2995

Deleted: Varga, G., Újvári, G., and Kovács, J.:
 Spatiotemporal patterns of Saharan dust outbreaks in the
 Mediterranean Basin, *Aeolian Res.*, 15, 151–160,
 doi:10.1016/j.aeolia.2014.06.005, 2014.

3001 Woodage, M.J., and Woodward, S.: U.K. HiGEM: Impacts of desert dust radiative forcing in a High-
3002 Resolution Atmospheric GCM, *J. Clim.*, 27, 5907-5928, 2014.
3003
3004 Yang, E.-S., Gupta, P., and Sundar, A. C.: Net radiative effect of dust aerosols from satellite
3005 measurements over Sahara, *Geophys. Res. Lett.*, 36, L18812, doi:10.1029/2009GL039801, 2009.
3006
3007 Yin, Y., Wurzler, S., Levin, Z., and Reisin, T. G.: Interactions of mineral dust particles and clouds: effects
3008 on precipitation and cloud optical properties, *J. Geophys. Res.*, 107, 4724, doi:10.1029/2001JD001544,
3009 2002.
3010
3011 Yin, Y. and Chen, L.: The effects of heating by transported dust layers on cloud and precipitation: a
3012 numerical study, *Atmos. Chem. Phys.*, 7, 3497-3505, doi:10.5194/acp-7-3497-2007, 2007.
3013
3014 Yorks, J. E., McGill, M., Rodier, S., Vaughan, M., Hu, Y., and Hlavka, D.: Radiative effects of African
3015 dust and smoke observed from Clouds and the Earth's Radiant Energy System (CERES) and Cloud-
3016 Aerosol Lidar with Orthogonal Polarization (CALIOP) data, *J. Geophys. Res.*, 114, D00H04,
3017 doi:10.1029/2009JD012000, 2009.
3018
3019 Zhang, D. F., Zakey, A. S., Gao, X. J., Giorgi, F., and Solomon, F.: Simulation of dust aerosol and its
3020 regional feedbacks over East Asia using a regional climate model, *Atmos. Chem. Phys.*, 9, 1095-1110,
3021 doi:10.5194/acp-9-1095-2009, 2009.
3022
3023 Zhang, Z., Meyer, K., Platnick, S., Oreopoulos, L., Lee, D., and Yu, H.: A novel method for estimating
3024 shortwave direct radiative effect of above-cloud aerosols using CALIOP and MODIS data, *Atmos. Meas.*
3025 *Tech.*, 7, 1777-1789, doi:10.5194/amt-7-1777-2014, 2014.
3026
3027 Zhang, Z., Meyer, K., Yu, H., Platnick, S., Colarco, P., Liu, Z., and Oreopoulos, L.: Shortwave direct
3028 radiative effects of above-cloud aerosols over global oceans derived from 8 years of CALIOP and
3029 MODIS observations, *Atmos. Chem. Phys.*, 16, 2877-2900, doi:10.5194/acp-16-2877-2016, 2016.
3030
3031 Zhao, C., Liu, X., Leung, L. R., Johnson, B., McFarlane, S. A., Gustafson Jr., W. I., Fast, J. D., and
3032 Easter, R.: The spatial distribution of mineral dust and its shortwave radiative forcing over North Africa:

Deleted: Yoshioka, M., Mahowald, N., Conley, A., Collins, W., Fillmore, D., and Coleman, D.: Impact of desert dust radiative forcing on Sahel precipitation: relative importance of dust compared to seasurface temperature variations, vegetation changes and greenhouse gas warming, *J. Climate*, 20, 1445-1467, 2007.¶

3040 modeling sensitivities to dust emissions and aerosol size treatments, Atmos. Chem. Phys., 10, 8821–
3041 8838, doi:10.5194/acp-10-8821-2010, 2010.

3042

3043 Zhao, C., Liu, X., Ruby Leung, L., and Hagos, S.: Radiative impact of mineral dust on monsoon
3044 precipitation variability over West Africa, Atmos. Chem. Phys., 11, 1879-1893, doi:10.5194/acp-11-
3045 1879-2011, 2011.

3046

3047 Zhu, A., Ramanathan, V., Li, F., and Kim, D.: Dust plumes over the Pacific, Indian, and Atlantic oceans:
3048 Climatology and radiative impact, J. Geophys. Res., 112, D16208, doi:10.1029/2007JD008427, 2007.

3049

3050

3051

3052

3053

3054

3055

3056

3057

3058

3059

3060

3061

3062

3063

3064

3065

3066

3067

3068

3069

3070

3071

Deleted: ¶
¶
¶
¶
¶
¶
¶
¶
¶
¶
¶
¶
¶
¶
¶
¶
¶
¶
¶
¶
¶
¶
¶

Table 1: List of the Mediterranean desert dust outbreaks which have been identified based on the satellite algorithm. In addition, the number of DD episodes (number of satellite grid cells at 1° x 1° spatial resolution where a DD episode has been identified), the regional intensity (in terms of AOD_{500nm}) calculated from the DD episodes as well as the dust affected parts of the Mediterranean domain are provided. ¶

Case ¶

Formatted: Justified, Line spacing: 1.5 lines

3095 **Table 1:** List of the Mediterranean desert dust outbreaks which have been identified within the geographical limits of the
 3096 MSD based on the satellite algorithm. In addition, the number of strong, extreme and total (strong plus extreme) DD episodes
 3097 (number of satellite grid cells at 1° x 1° spatial resolution where a DD episode has been identified), the regional intensity (in
 3098 terms of AOD_{550nm}) calculated from the total DD episodes as well as the dust affected parts of the Mediterranean domain are
 3099 provided.

<u>Case</u>	<u>Date</u>	<u>Strong DD episodes</u>	<u>Extreme DD episodes</u>	<u>Total DD episodes</u>	<u>Intensity</u>	<u>Affected parts of the Mediterranean domain</u>
<u>1</u>	<u>31 July 2001</u>	<u>56</u>	<u>29</u>	<u>85</u>	<u>0.74</u>	<u>Western</u>
<u>2</u>	<u>8 May 2002</u>	<u>20</u>	<u>51</u>	<u>71</u>	<u>1.60</u>	<u>Central</u>
<u>3</u>	<u>4 April 2003</u>	<u>23</u>	<u>30</u>	<u>53</u>	<u>1.42</u>	<u>Eastern</u>
<u>4</u>	<u>16 July 2003</u>	<u>38</u>	<u>45</u>	<u>83</u>	<u>0.98</u>	<u>Western and Central</u>
<u>5</u>	<u>22 February 2004</u>	<u>10</u>	<u>36</u>	<u>46</u>	<u>2.18</u>	<u>Central and Eastern</u>
<u>6</u>	<u>26 March 2004</u>	<u>28</u>	<u>38</u>	<u>66</u>	<u>1.45</u>	<u>Central and Eastern</u>
<u>7</u>	<u>27 January 2005</u>	<u>12</u>	<u>25</u>	<u>37</u>	<u>1.36</u>	<u>Central and Eastern</u>
<u>8</u>	<u>2 March 2005</u>	<u>8</u>	<u>37</u>	<u>45</u>	<u>2.96</u>	<u>Central and Eastern</u>
<u>9</u>	<u>28 July 2005</u>	<u>10</u>	<u>20</u>	<u>30</u>	<u>1.08</u>	<u>Western and Central</u>
<u>10</u>	<u>24 February 2006</u>	<u>3</u>	<u>42</u>	<u>45</u>	<u>2.92</u>	<u>Eastern</u>
<u>11</u>	<u>19 March 2006</u>	<u>11</u>	<u>28</u>	<u>39</u>	<u>1.37</u>	<u>Eastern</u>
<u>12</u>	<u>24 February 2007</u>	<u>8</u>	<u>34</u>	<u>42</u>	<u>2.29</u>	<u>Central and Eastern</u>
<u>13</u>	<u>21 April 2007</u>	<u>15</u>	<u>27</u>	<u>42</u>	<u>1.65</u>	<u>Central</u>
<u>14</u>	<u>29 May 2007</u>	<u>17</u>	<u>30</u>	<u>47</u>	<u>1.40</u>	<u>Eastern</u>
<u>15</u>	<u>10 April 2008</u>	<u>9</u>	<u>33</u>	<u>42</u>	<u>1.58</u>	<u>Central</u>
<u>16</u>	<u>19 May 2008</u>	<u>16</u>	<u>50</u>	<u>66</u>	<u>1.45</u>	<u>Central</u>
<u>17</u>	<u>23 January 2009</u>	<u>4</u>	<u>32</u>	<u>36</u>	<u>2.65</u>	<u>Eastern</u>
<u>18</u>	<u>6 March 2009</u>	<u>18</u>	<u>23</u>	<u>41</u>	<u>1.41</u>	<u>Eastern</u>
<u>19</u>	<u>27 March 2010</u>	<u>10</u>	<u>29</u>	<u>39</u>	<u>1.43</u>	<u>Central</u>
<u>20</u>	<u>2 August 2012</u>	<u>12</u>	<u>23</u>	<u>35</u>	<u>1.20</u>	<u>Western</u>

3100
 3101
 3102
 3103
 3104
 3105
 3106
 3107
 3108
 3109
 3110
 3111
 3112
 3113
 3114
 3115
 3116
 3117
 3118
 3119
 3120
 3121
 3122

3123 **Table 2:** Mean and standard deviation of all-sky DRE_{TOA} , DRE_{SURF} , $DRE_{NETSURF}$ and DRE_{ATM} values, over the simulation
 3124 period (84 hours), calculated in the NSD, SDD and MSD domains for the SW, LW and NET radiation. Blue and red
 3125 background colors indicate negative (cooling effect) and positive (warming effect) DREs, respectively.

Deleted: clear

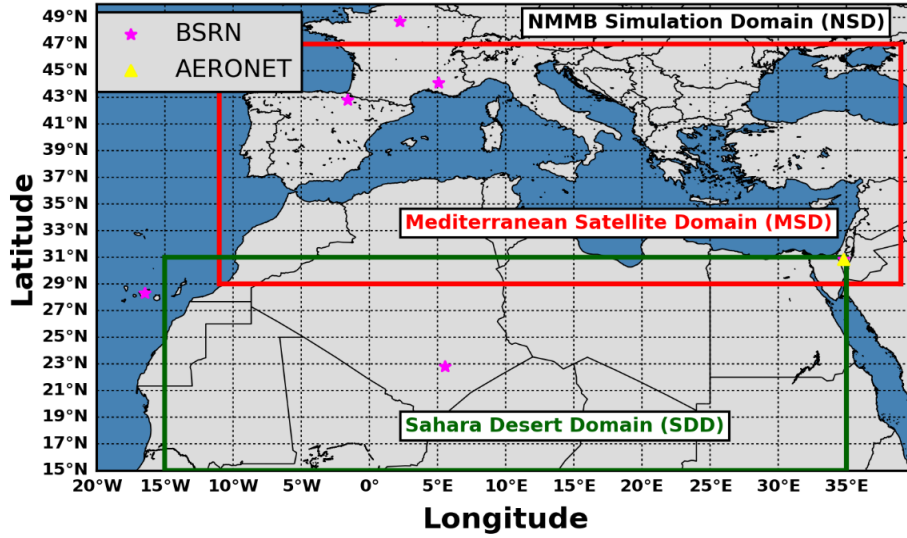
		DRE_{TOA}	DRE_{SURF}	$DRE_{NETSURF}$	DRE_{ATM}
NSD	SW	-3.5±3.4	-16.3±14.3	-12.5±11	9.0±9.3
	LW	0.9±0.5	1.7±0.4	3.0±0.9	-2.0±0.4
	NET	-2.6±3.2	-14.7±14.6	-9.6±10.2	7.0±9.0
SDD	SW	-2.8±5	-20.8±18.8	-14.1±12.8	11.4±12.2
	LW	1.4±1.1	2.8±0.7	5.0±1.8	-3.6±0.8
	NET	-1.3±5	-18.0±19.3	-9.1±11.2	7.8±11.7
MSD	SW	-4.5±4	-15.4±13.8	-12.8±11.6	8.3±8.5
	LW	0.7±0.3	1.2±0.4	2.1±0.5	-1.4±0.3
	NET	-3.8±3.8	-14.2±14	-10.8±11.2	6.9±8.3

3126

3127

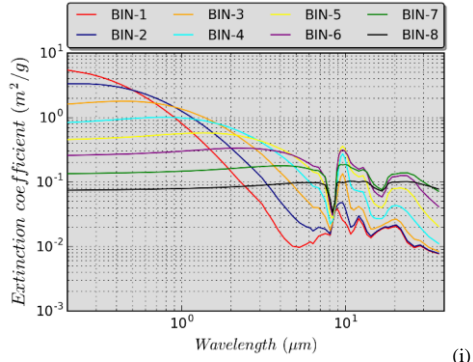
3128

3129

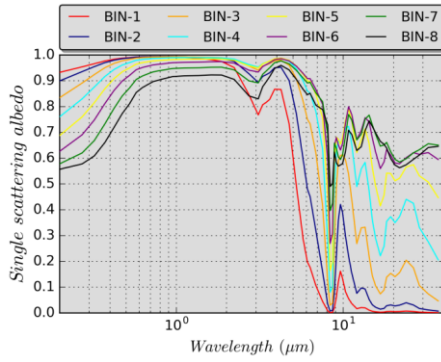


3131 **Figure 1:** Geographical limits of the: (i) NMMB Simulation Domain (NSD, outer domain), (ii) Mediterranean Satellite
 3132 Domain (MSD, red rectangle) and (iii) Sahara Desert Domain (SDD, green rectangle). With the magenta star symbols are
 3133 depicted the locations of the BSRN stations and with the yellow triangle is denoted the location of the AERONET Sede Boker
 3134 station.
 3135

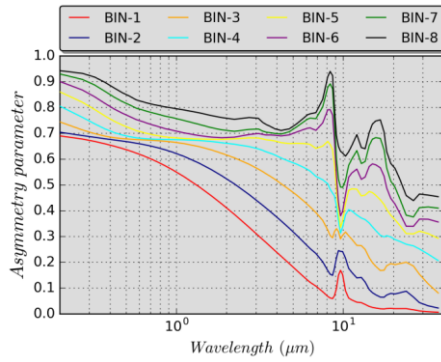
3136
 3137
 3138
 3139
 3140
 3141
 3142
 3143
 3144
 3145
 3146
 3147



(i)



(ii)

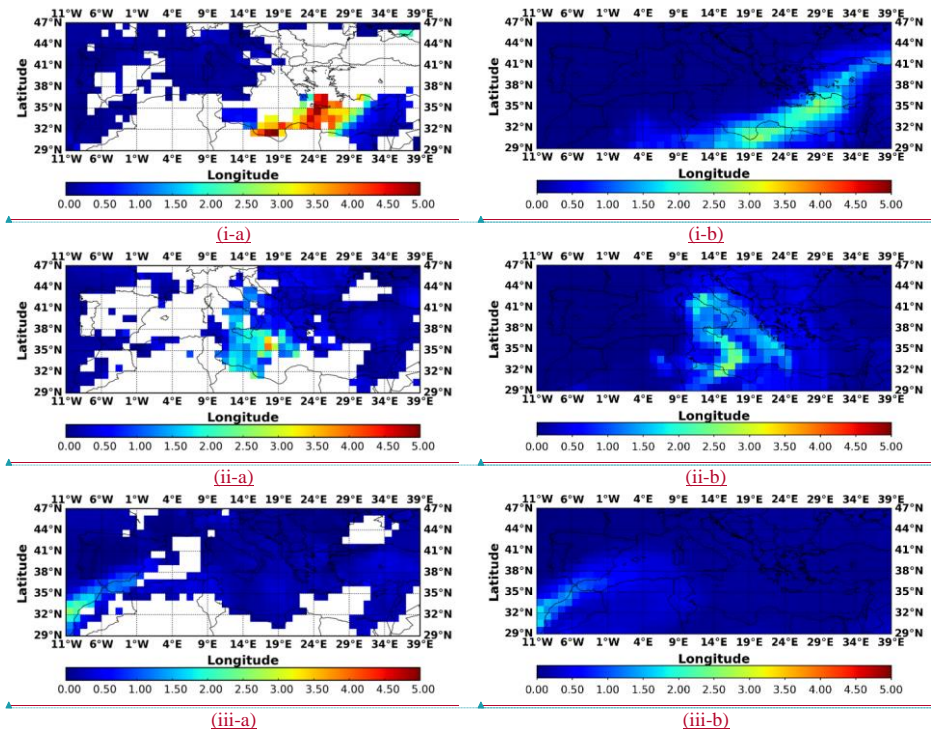


(iii)

3148 **Figure 2:** Spectral variation of the GOCART: (i) extinction coefficient (in m^2/g), (ii) single scattering albedo and (iii)
 3149 asymmetry parameter, for each one of the 8 dust bins which are considered in the dust module.

3150

3151



Formatted: Font: (Default) Times New Roman, 10 pt, No underline, Font color: Auto

Formatted: Font: (Default) Times New Roman, 10 pt, No underline, Font color: Auto

Formatted: Font: (Default) Times New Roman, 10 pt, No underline, Font color: Auto

Formatted: Font: (Default) Times New Roman, 10 pt, No underline, Font color: Auto

Formatted: Font: (Default) Times New Roman, 10 pt, No underline, Font color: Auto

Formatted: Font: (Default) Times New Roman, 10 pt, No underline, Font color: Auto

3152 **Figure 3:** Geographical distributions of the aerosol optical depth (AOD) at 550 nm: (a) retrieved by the MODIS-Terra sensor
 3153 and (b) simulated by the NMMB-MONARCH model at 12:00 UTC for the Mediterranean desert dust outbreaks that took
 3154 place on: (i) 2nd March 2005, (ii) 19th May 2008 and (iii) 2nd August 2012.

3155
 3156
 3157

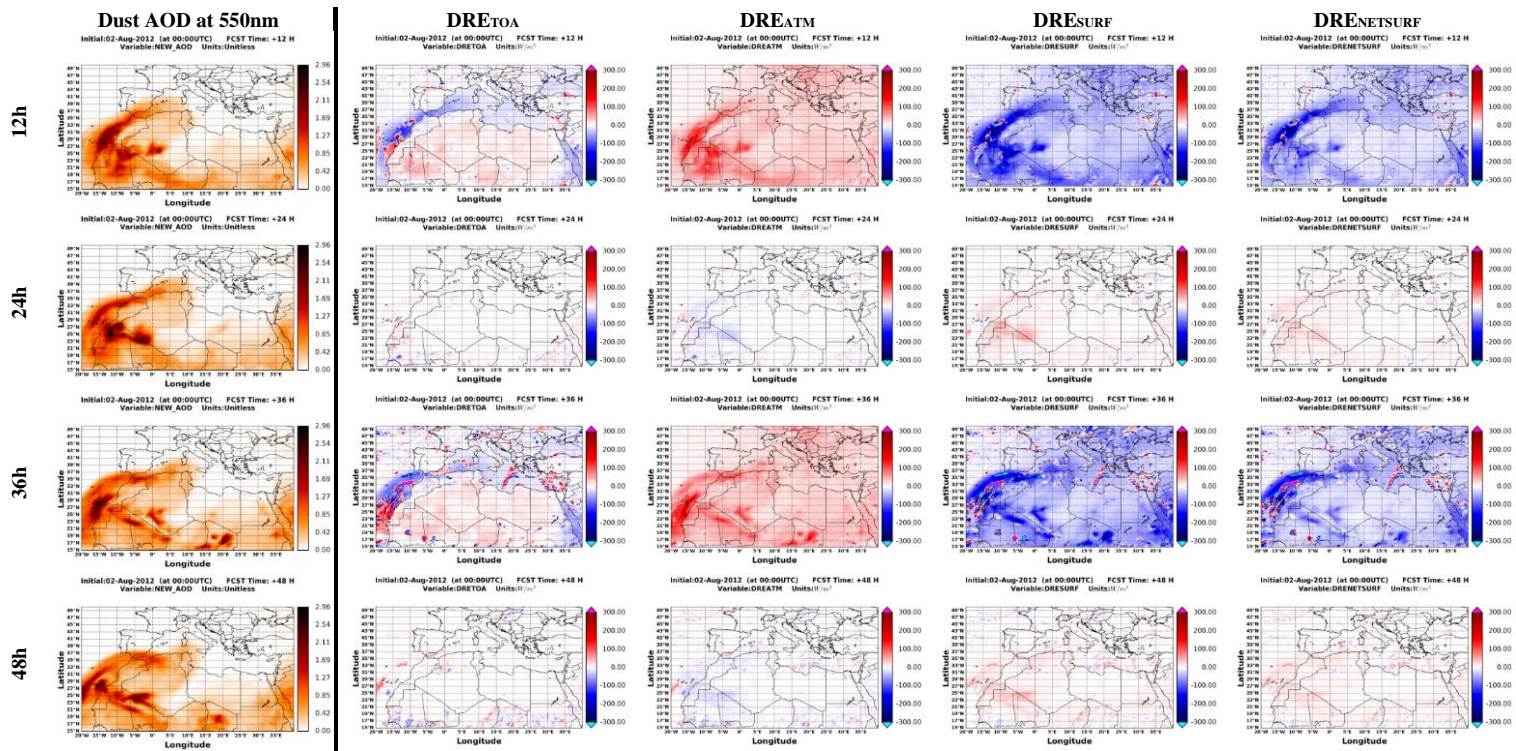


Figure 4: Spatial patterns of the simulated dust AOD_{550nm} and the instantaneous DRE_{TOA}, DRE_{ATM}, DRE_{SURF} and DRE_{NETSURF} values, expressed in Wm⁻², at 12, 24, 36 and 48 hours after the initialization of NMMB-MONARCH model at 00 UTC on 2nd August 2012.

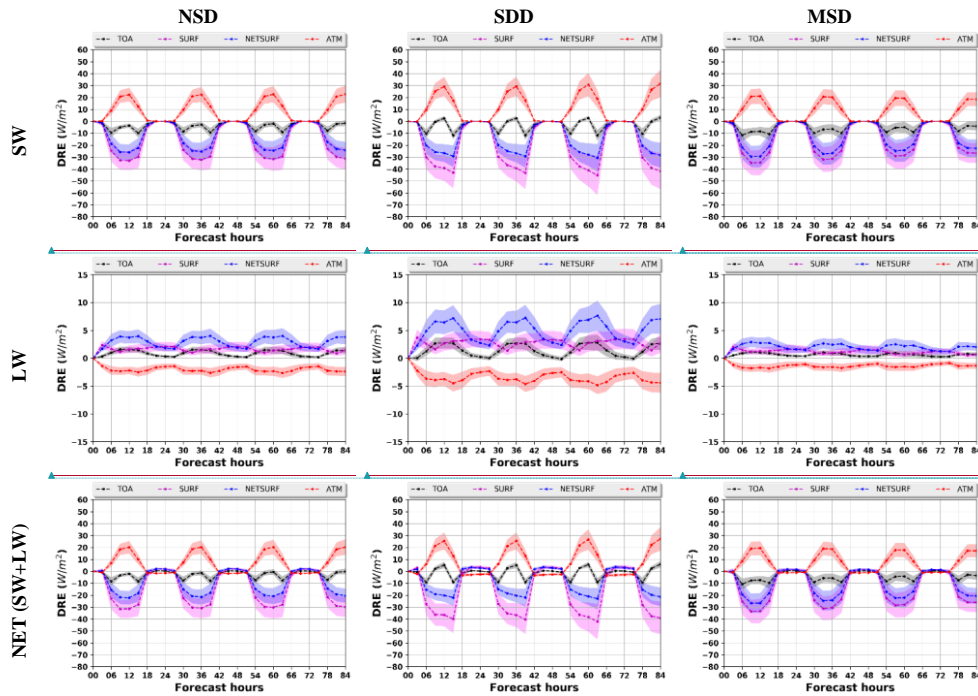


Figure 5: Regional all-sky SW (upper row), LW (middle row) and NET (SW+LW) (bottom row) DREs at TOA (black), SURF (purple), NETSURF (blue) and ATM (red) averaged over the NSD (left column), SDD (central column) and MSD (right column) domains. The calculated DREs correspond to the mean values calculated from the 20 simulated Mediterranean desert dust outbreaks and the shaded areas represent the associated standard deviation.

Formatted: Font: (Default) Times New Roman, 10 pt, No underline, Font color: Auto

Formatted: Font: (Default) Times New Roman, 10 pt, No underline, Font color: Auto

Formatted: Font: (Default) Times New Roman, 10 pt, No underline, Font color: Auto

Formatted: Font: (Default) Times New Roman, 10 pt, No underline, Font color: Auto

Formatted: Font: (Default) Times New Roman, 10 pt, No underline, Font color: Auto

Formatted: Font: (Default) Times New Roman, 10 pt, No underline, Font color: Auto

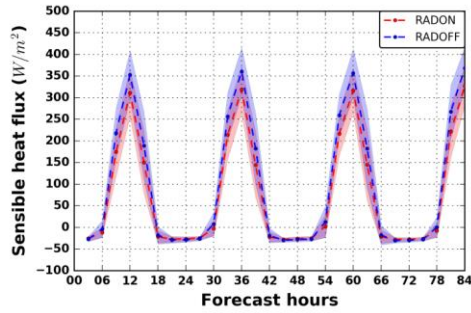
Formatted: Font: (Default) Times New Roman, 10 pt, No underline, Font color: Auto

Formatted: Font: (Default) Times New Roman, 10 pt, No underline, Font color: Auto

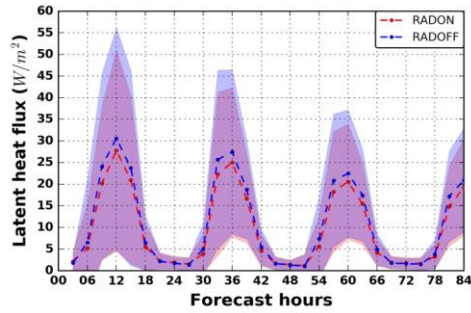
Formatted: Font: (Default) Times New Roman, 10 pt, No underline, Font color: Auto

Deleted: clear

Deleted: by



(i)



(ii)

Figure 6: Regional averaged values, over land areas of the simulation domain affected by dust loads and under clear-sky conditions, of the: (i) sensible and (ii) latent heat fluxes, expressed in Wm^{-2} , based on the RADON (red) and the RADOFF (blue) configuration of the NMMB-MONARCH model. The dashed lines correspond to the mean values calculated by the 20 simulated Mediterranean desert dust outbreaks and the shaded areas represent the associated standard deviation.

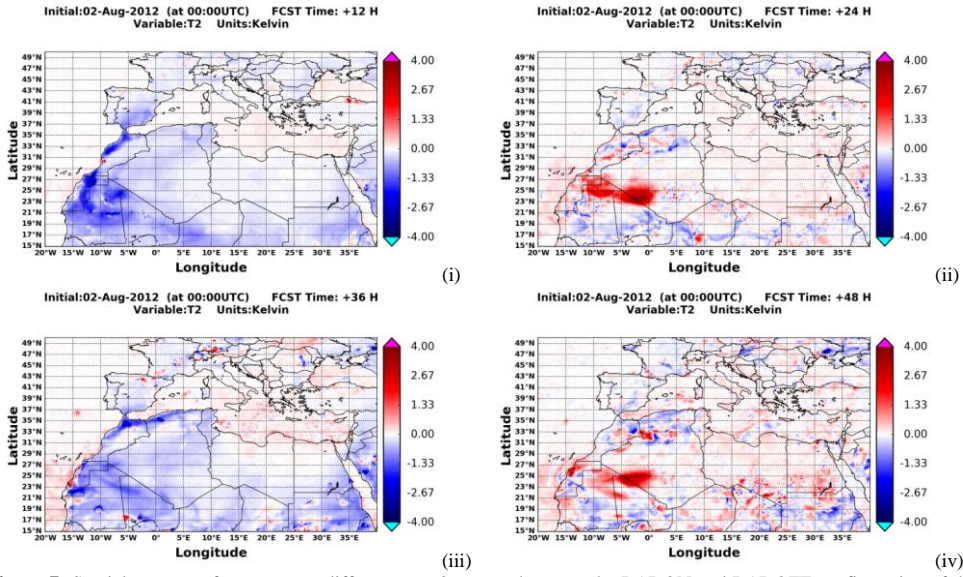


Figure 7: Spatial patterns of temperature differences at 2 meters, between the RADON and RADOFF configuration of the NMMB-MONARCH model, for the: (i) 12, (ii) 24, (iii) 36 and (iv) 48 hours forecast of the 00 UTC cycle on 2nd August 2012.

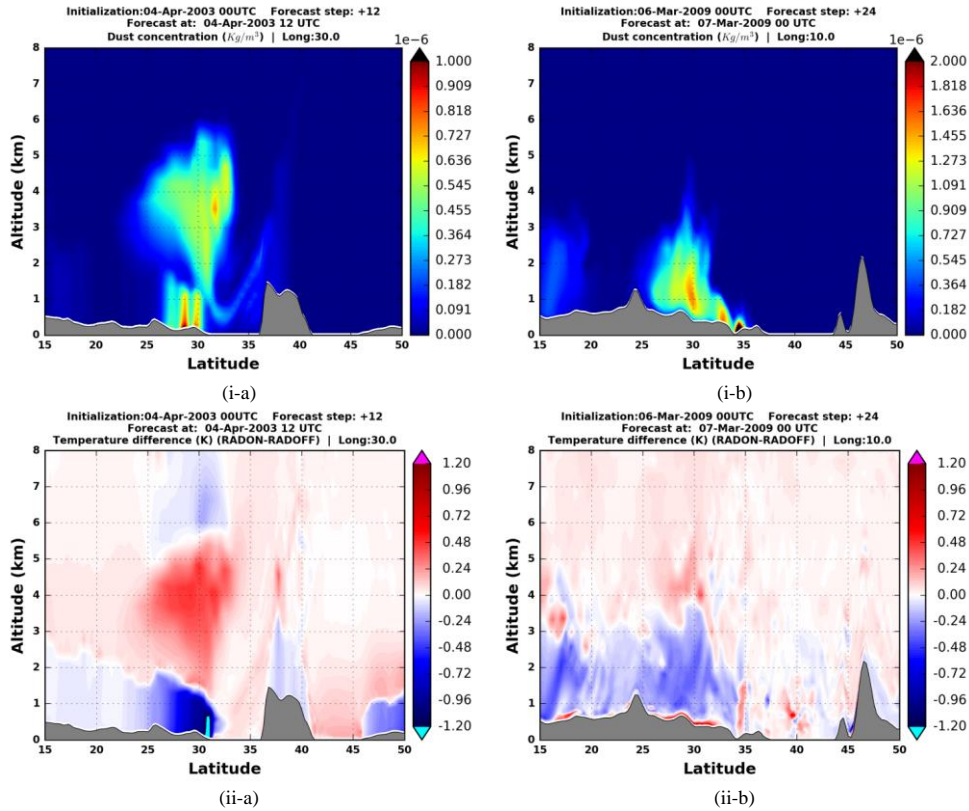
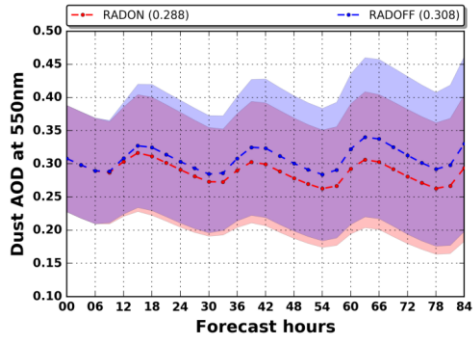
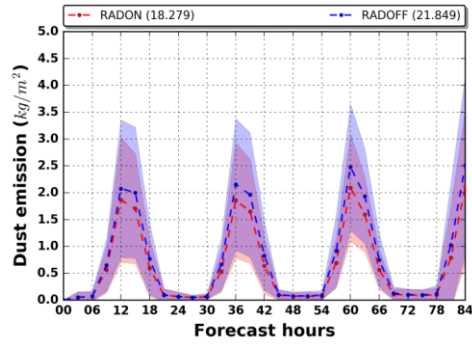


Figure 8: Altitude-latitude cross-sections (up to 8 km m.s.l.) simulated by the NMMB-MONARCH model of the: (i) dust concentration (in kg m^{-3}) and (ii) RADON-RADOFF temperature anomalies (in K) on: (a) 4 April 2003 at 12 UTC along the meridional 30° E and (b) 7 March 2009 00 UTC along the meridional 10° E.



(i)



(ii)

Figure 9: (i) Regional dust AOD at 550nm averaged over the simulation domain (NSD) and (ii) Regional dust emission (in kg m^{-2}) aggregated over the simulation domain (NSD). Blue and red curves correspond to the mean values, calculated from the 20 desert dust outbreaks, for the RADOFF and RADON simulations, respectively, and the shaded areas represent the associated standard deviation.

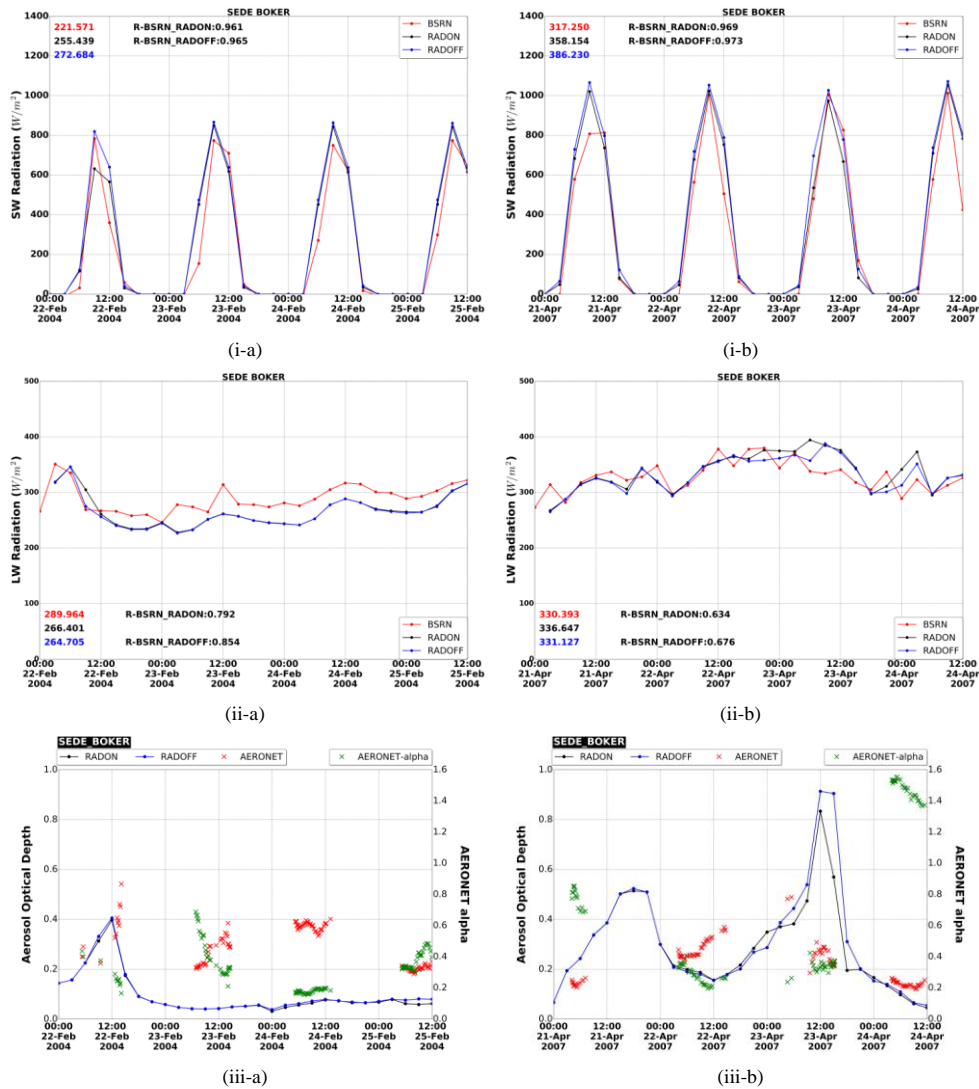
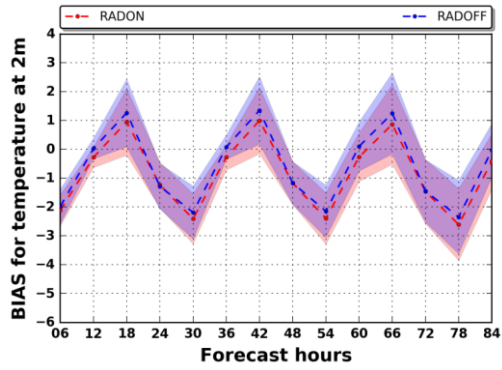
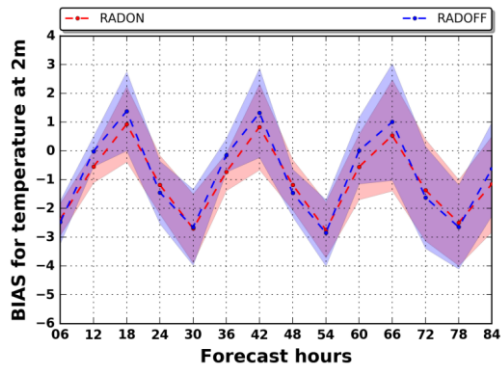


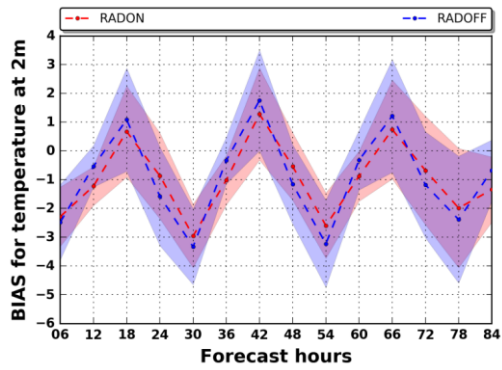
Figure 10: Timeseries of the downwelling: (i) SW and (ii) LW radiation measured at Sede Boker (red line) and simulated based on the RADON (black line) and RADOFF (blue line) configuration of the NMMB-MONARCH model during the periods: (a) 22 Feb. 2004 00UTC – 25 Feb. 2004 12UTC and (b) 21 Apr. 2007 00UTC – 24 Apr. 2007 12UTC. The mean ground and modelled values along with the computed correlation coefficients (R) between RADON-BSRN and RADOFF-BSRN, both calculated over the simulation periods, are also provided. (iii) Timeseries of the simulated dust AOD at 550 nm for the RADON (black line) and RADOFF (blue line) configuration of the NMMB-MONARCH model. Moreover, the AERONET total AOD at 500 nm and AERONET alpha values are provided.



(i)



(ii)



(iii)

Figure 11: Regional biases of temperature at 2 meters between NMMB-MONARCH and FNL, at $1^\circ \times 1^\circ$ degrees spatial resolution, calculated over land grid points of the simulation domain (NSD) in which dust AOD at 550 nm is higher/equal than: (i) 0.1, (ii) 0.5 and (iii) 1.0.

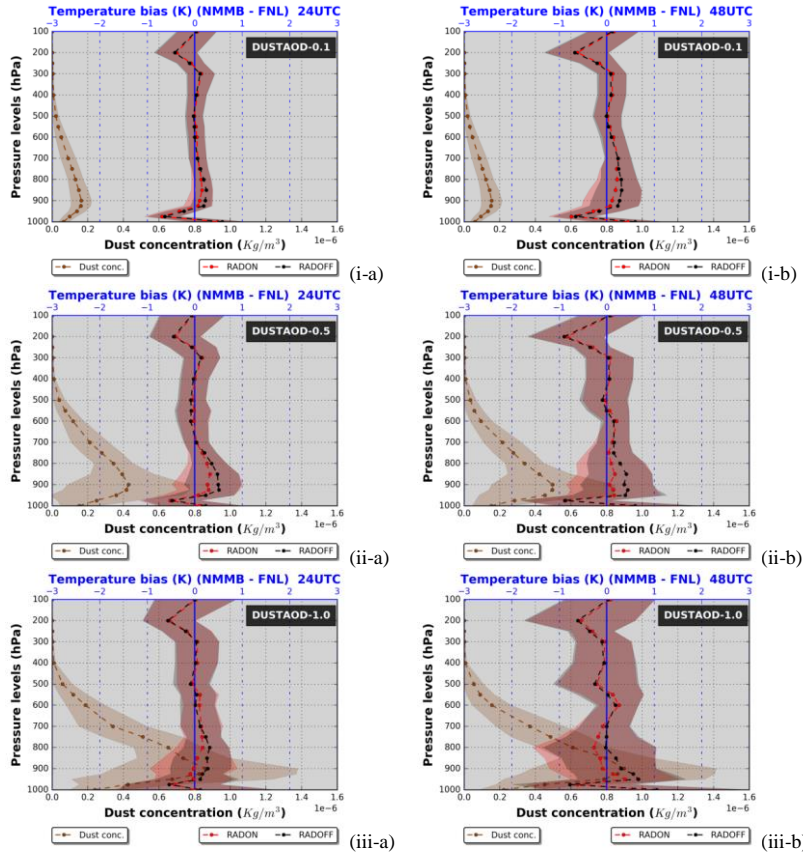


Figure 12: Vertical profiles of the regional temperature RADON-FNL (red curve) and RADOFF-FNL (black curve) biases calculated over grid points ($1^\circ \times 1^\circ$ degrees spatial resolution) where the dust AOD at 550 nm is higher/equal than: (i) 0.1, (ii) 0.5 and (iii) 1.0. In addition, the vertical profiles of the simulated dust concentration (in $\times 10^{-6} \text{kg m}^{-3}$) are provided (brown curve). Each profile corresponds to the mean value calculated from the 20 desert dust outbreaks which are considered while the shaded areas correspond to the associated standard deviations. The obtained results are valid: (a) 24 and (b) 48 hours after the initialization of the forecast period.